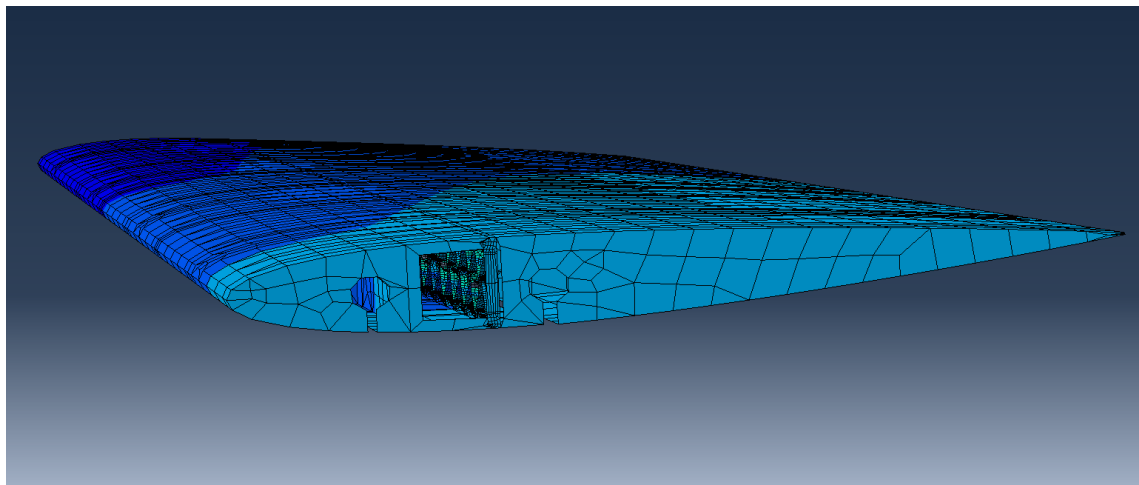


Master's thesis no. 17-063

Bending-twist Shape Adaptation By Compliant Chiral Spar Design

Alejandro Valverde López

Advisor: Falk Runkel

IDMF - Laboratory of Composite Materials and Adaptive Structures
Prof. Dr. Paolo Ermanni
ETH Zrich

27.09.2017

ETH Zrich
IDMF - Laboratory of Composite Materials and Adaptive Structures
LEE O 203
Leonhardstrasse 21
8082 Zrich

Telefon: +41 (0)44 633 63 02

www.structures.ethz.ch

Abstract

This thesis presents a novel purely passive mechanism of twist morphing for application on aerospace structures, such as wings. During certain flight conditions such as gust encountering, the aircraft may experience critical loads that threaten the structural integrity. To counteract this situation, a time-bounded modification of the lift distribution to achieve a reduction in the aerodynamic load is needed. The proposed method aims to control the bending-twist coupling of a wing-box that implements a variable-stiffness adaptive spar. This component is comprised of a lattice of chiral elements that undergo elastic instabilities on its ligaments under certain load, originating a sudden reduction of the shear modulus in the adaptive spar. The modification of the effective shear modulus in this element provokes the wing-box shear center shifting, a consequent modification of the torsional stiffness and, ultimately, a buckling-induced sectional twist in the wing-box. The mechanism therefore consists on a highly nonlinear variation of the wing twist passively triggered by the onset of buckling on the chiral structure. An analytical model of the wing-box is developed to provide information related to the changes in mechanical properties through modifications in shear modulus on the variable-stiffness spar. A fully parametrized computational model of the whole wing-box assembly is built to provide insight of the buckling phenomena and the nonlinear twist response of the structure. An extensive analysis of the influence of each of the main parameters in the buckling appearance and evolution, and in final twist response is also presented. Numeric results show that the snap-buckling instabilities indeed provide an effective method of changing the torsional stiffness of a wing-box and therefore affecting the twist and the lift distribution over the wing. Also, results show that parameters such as the wing-box thickness or the ligament eccentricity provide tailorability capabilities over the mechanism activation and the response evolution. In a further step, the wing-box model is embedded into a more complex model of a wing where realistic aerodynamic loads are applied on the wing skin. The effect wing box torsional adaptation is therefore shown to reduce the bending moment at the root.

Zusammenfassung

Acknowledgments

First of all, I would like to thanks Dr. Simon Prince from Cranfield University for offering himself to remotely supervise this thesis.

Secondly, I would like to thank to Prof. Dr. Paolo Ermanni for the opportunity offered to conduct my master thesis at the Laboratory of Composite Materials and Adaptive Structures at ETH Zürich.

Furthermore, I would like to thank my advisor at ETH Zürich, Falk Runkel, for his kindness and continuous help and support. His inestimable aid put my work into the right path so I could feel proud of it.

Special thanks to Theofanis Tsiantas who provided an enormous help throughout the whole project. His suggestions and support helped me to gain fundamental understanding of the structures mechanics.

Finally, I would like to give my eternal gratitude to my family, for their full and unconditional support throughout all this years of my education.

	Valverde, Alejandro	
Student:	ETH-Nr:	Departement: MAVT
	Hochschule (if external student): Cranfield University	
Thesis:	Title: Bending-Twist Shape Adaptation by Compliant Chiral Spar Design	
	Kind of Thesis: MA	Semester: FS2017
Supervisor:	Prof. Dr. P. Ermanni	
Advisor:	Runkel, Falk; Keidel, Dominic; Urban Fasel	

Start of the work:	01/04/2017
Intermediate presentation (Zwischenpräsentation):	tbd
Final presentation (Endpräsentation):	31/08/2017
Deadline delivery final report:	30/09/2017

Introduction

Shape adaptation of aerodynamic surfaces offers great potential for performance improvement across a wide range of flight conditions. In general, morphing structures encounter the challenge of combining the capability of carrying external loads (requiring a particular stiffness) with the need to macroscopically change its shape (requiring high compliance). For achieving purely passive shape adaptation by means of a desired bending-twist coupling, the proposed thesis studies the utilisation of a structurally tailored wing box featuring a unique mechanical response. The wing box is comprised by two flanges and two spars, one of which is designed by chiral periodic elements with curved ligaments, adding an additional geometrical parameter to the chiral design [1]. This significantly augments the tailorability of the mechanical behaviour of the chiral spar under deformation, which – in turn – affects the torsional stiffness and shear centre location of the wing box and, consequently, its torsional response [2,3]. Under shear and bending deformation – resulting from the aerodynamic pressure acting on the wing structure – the microstructural deformation behaviour of the chiral spar design is utilised to affect the global bending-twisting coupling of the wing structure. The attainable change in stiffness of the chiral spar, offered by virtue of the curved ligament design, is therefore exploited to increase the structural efficiency of the wing, e.g. by enabling load alleviation by means of root bending moment reduction.

Objectives

For achieving a buckling-induced twisting of wing structures, we consider a wing profile with a wing box comprised by two spars, one of which is designed with the novel chiral structure introduced at our institute. The initially very large shear modulus of chiral structures – owing

to their microstructural deformation behaviour – significantly contributes to the torsional stiffness of the wing box. At a particular external load, the shear flow in the web exceeds the buckling limit, resulting in a drastic reduction of the effective shear modulus of this structural element. As a result, the torsional stiffness and the shear centre is affected, leading to a purely passively induced local twist of the affected wing sections, conceptually shown in Figure 1. For the wing structure, this buckling-induced change in twist results in a spanwise varied effective angle of attack which we aim to exploit for load alleviation purposes.

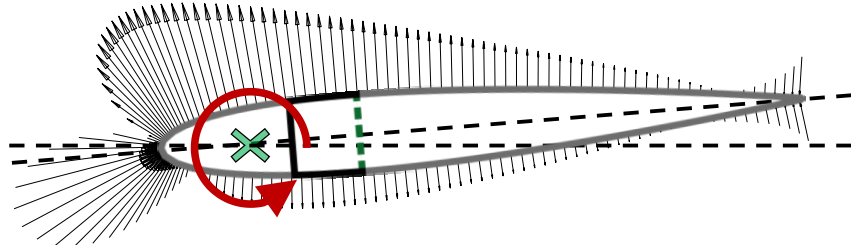


Figure 1- Wing with variable shear stiffness spar. Twisting results due to change in mechanical properties of rear spar under aerodynamic loads

In the first part of the thesis, parametric studies for the existing finite element simulation for a wing box structure with embedded chiral buckling elements are conducted. By means of numerical simulations, we assess the impact of geometrical parameters of the internal structure for the shape adaptation capability of the proposed concept.

These studies aim to find a wing box design that can be utilised for conducting simple preliminary tests, showing that a buckling-induced change in twist of the box structure can be obtained. For this purpose, chiral lattices must be manufactured to be applied for the spar design (Figures 2 and 3). The remaining structural elements of the wing box are manufactured with isotropic material to simplify manufacturing and the analytical calculation of the twisting of the beam. For a realistic wing design, the wing box is implemented in a NACA0012 wing profile, and aero-elastic analyses are conducted, utilising techniques already developed at our institute. The proposed concept is studied for achieving shape adaptation of wing structures under realistic aerodynamic loads, with the aim to reduce the loads on the wing and to improve its aero-elastic behaviour. The results of this study are compared to the state of the art for achieving passive twisting of wing structures and benefits/drawback of the novel design idea are evaluated.

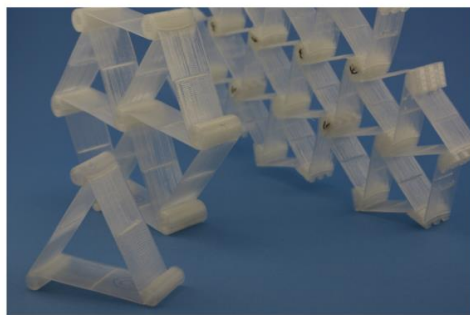


Figure 2 – Chiral elements with curved ligaments, processed by additive manufacturing

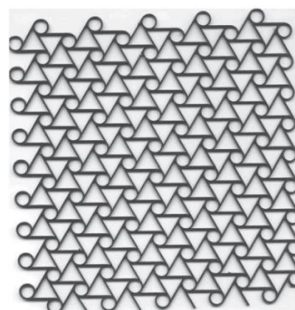
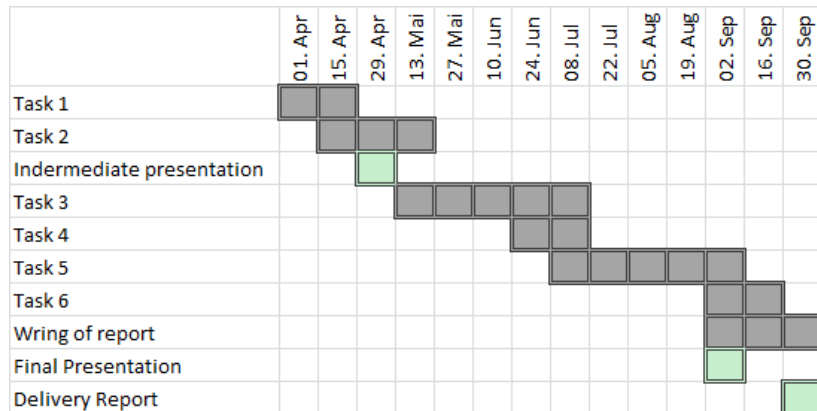


Figure 3 – Periodic chiral structure (taken from Bornengo, 2005)

Work breakdown

1. Task 1: Familiarisation with software (Abaqus CAE, XFOIL) and manufacturing techniques (3D printing process) of chiral structures.

2. **Task 2:** Finite elements analysis for assessing impact of geometrical parameters of chiral structure on the shape adaptation capability of simple wing box structure
3. **Task 3:** Manufacturing of wing box demonstrator with chiral elements shear web
4. **Task 4:** Testing of demonstrator for simple load cases
5. **Task 5:** Finite elements study of wing structures with chiral shear webs: aero-elastic analyses
6. **Task 6:** Comparison of results with existing concepts: benefits/drawbacks



Bibliography

- [1] Bornengo, Scarpa, and Remillat, Evaluation of hexagonal chiral structure for morphing airfoil concept, 2005
- [2] Urs Steiner, Airfoil camber morphing through tailored structural instability
- [3] Gilles Ramstein, Experimental validation of chiral structures with controlled local instability

Please consider

- ❖ Directives and useful information about Student Projects at the Laboratory of Composite Materials and Adaptive Structures are available online at:
http://www.structures.ethz.ch/content/dam/ethz/special-interest/mavt/design-materials-fabrication/composite-materials-dam/Education/Informationen/CMAS_Richtlinien_Studienarbeiten_EN.pdf
- ❖ Don't forget to register for the thesis under "My Studies" www.myStudies.ethz.ch at the begin of the semester
- ❖ This document has to be included in the final report

Zurich, 22/01/2017

Supervisor:

Advisor:

Student:

Prof. P. Ermanni

Declaration of originality

The signed declaration of originality is a component of every semester paper, Bachelor's thesis, Master's thesis and any other degree paper undertaken during the course of studies, including the respective electronic versions.

Lecturers may also require a declaration of originality for other written papers compiled for their courses.

I hereby confirm that I am the sole author of the written work here enclosed and that I have compiled it in my own words. Parts excepted are corrections of form and content by the supervisor.

Title of work (in block letters):

Bending-twist Shape Adaptation by Compliant Chiral Spar Design

Authored by (in block letters):

For papers written by groups the names of all authors are required.

Name(s):

Valverde López

First name(s):

Alejandro

With my signature I confirm that

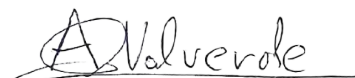
- I have committed none of the forms of plagiarism described in the '[Citation etiquette](#)' information sheet.
- I have documented all methods, data and processes truthfully.
- I have not manipulated any data.
- I have mentioned all persons who were significant facilitators of the work.

I am aware that the work may be screened electronically for plagiarism.

Place, date

Zürich, 08.09.2017

Signature(s)



For papers written by groups the names of all authors are required. Their signatures collectively guarantee the entire content of the written paper.

Contents

Abstract	i
Zusammenfassung	iii
Acknowledgments	v
List of figures	xxi
List of tables	xxiii
List of symbols	xxviii
1 Introduction	1
2 State-of-the-art	5
2.1 Morphing aircraft	5
2.2 Compliant chiral structure	11
2.3 Rationale for the thesis	16
3 Wing-box model	19
3.1 Concept	19
3.2 Analytical model	21
3.3 Computational model	24
3.3.1 Sub-parts and parametrization of the model	25
3.3.2 Computational model mesh characteristics	33

3.3.3	Load definition	34
3.3.4	Boundary condition	35
3.3.5	Lattice nodes rigid body modeling	36
3.3.6	Connection between the wing-box skin and the chiral lattice	40
3.3.7	Post-processing operations	44
3.3.8	Parametric study method	44
4	Model analysis	47
4.1	Analytical model analysis	47
4.1.1	Bending and twisting coupling results and discussion	49
4.1.2	Parametric study results and discussion	50
4.2	Computational model analysis	59
4.2.1	Rigid body modeling	59
4.2.2	Load introduction method	61
4.2.3	Connection between the wing-box skin and the chiral lattice	64
4.2.4	Mesh	66
4.2.5	Nonlinear problem and automatic stabilization	67
4.2.6	Ribs inclusion and control over the local deformation	71
5	Simulations results	75
5.1	General response characterization	75
5.2	Parametric study on the computational model	80
5.2.1	Wing-box thickness	80
5.2.2	Number of unit cells in the chiral lattice	85
5.2.3	Chiral lattice parameters	90
6	Aeroelastic study	105

6.1	Wing model	105
6.2	Aerodynamic model	106
7	Conclusion and Outlook	107
	Bibliography	109
A	Python code generated	113

List of Figures

1.1	Aircraft encountering a vertical gust	2
2.1	Wright Brothers 1899 kite	6
2.2	Shape morphing wing classification	6
2.3	The X-53 performing a 360° roll to prove AAW technology	7
2.4	Inner structure of the experimental wing build to test the concept of adaptive wing-box	9
2.5	Plate buckling on one of the webs of the wing-box beam	10
2.6	Chiral structure of rotatable nodes and bendable ligaments	11
2.7	Experimental Poisson's ratio v as a function of axial compressive strain on a chiral honeycomb	12
2.8	Chiral cell elements showing different ligaments curvatures	13
2.9	Compression load test on a basic triangular chiral structure	14
2.10	Investigated configurations for the truss-core of chiral topology	14
2.11	Manufactured prototype of a truss-core airfoil with chiral topology	15
2.12	Chiral sail concept	15
3.1	Working principle for the adaptive beam	20
3.2	Set of chiral ligaments undergoing elastic instabilities at the root of the wing-box	21
3.3	Schematic view of the beam closed section	22
3.4	General assembly configuration for the computational model	24

3.5	Default normals and thickness direction for continuum shell elements in Abaqus	24
3.6	Overview of the lattice of chiral elements part	25
3.7	Division of the lattice structure in cell units	26
3.8	Internal parameters of the chiral structure in the lattice	27
3.9	Overview of the wing-box in C-profile part	29
3.10	Internal parameters of the wing-box in C-profile part	29
3.11	Internal parameters of the two different ribs parts	31
3.12	Internal parameters of the two different ribs parts	33
3.13	Load introduction points located on the upper flange of the tip rib and the two inner ribs .	34
3.14	Boundary condition for the model	35
3.15	Picture of the manufactured chiral lattice nodes	36
3.16	Kinematic coupling constraint	37
3.17	Overview of the elements that are involved in the coupling condition at the lattice nodes .	37
3.18	Overview of the tyre part	38
3.19	Internal parameters of the tyre part	39
3.20	Overview of the connection between tyre and lattice node	39
3.21	Detail of the connection between the lattice nodes and the skin	40
3.22	Blocked translation and free rotation connection between the lattice nodes and the skin .	41
3.23	Free translation and rotation connection between the lattice nodes and the skin	41
3.24	Simple rigid connection between the wing-box skin and the chiral node	42
3.25	Coupling condition between the lattice node and the wing-box skin through tyre	43
3.26	Location of the mesh nodes from which valued of the rotational displacement u is extracted	44
3.27	Flow chart showing the execution of the parametric study python code	45
4.1	Influence of the stiffness ratio on the wing-box tip twist and bend	49
4.2	Influence of the cross-sectional aspect ratio B/H on the torsional stiffness GI_t	50

4.3	Influence of the cross-sectional aspect ratio B/H on the dimensionless shear centre position y_{SC}/B	51
4.4	Influence of the cross-sectional aspect ratio B/H on the flexural stiffness EI_y	51
4.5	Influence of the wall thickness ratio t_2/t_1 on the torsional stiffness GI_t	52
4.6	Influence of the wall thickness ratio t_2/t_1 on the dimensionless shear centre position y_{SC}/B	52
4.7	Influence of the wall thickness ratio t_2/t_1 on the flexural stiffness EI_y	53
4.8	Influence of the cross-sectional aspect ratio B/H on the flexural compliance	55
4.9	Influence of the cross-sectional aspect ratio B/H on the torsional compliance	55
4.10	Influence of the thickness ratio t_2/t_1 on the flexural compliance	56
4.11	Influence of the thickness ratio t_2/t_1 on the torsional compliance	56
4.12	Influence of the slenderness ratio L/B on the flexural compliance	57
4.13	Influence of the slenderness ratio L/B on the torsional compliance	58
4.14	Displacement-force curve obtained using different approaches to model the rigid lattice node	60
4.15	Displacement-force curve showing the model response using different load introduction methods	61
4.16	Deformed state of the model for a distributed load introduction method	62
4.17	Displacement-force curve showing the model response for different load introduction points z/W_{box}	63
4.18	Displacement-force curve showing the model response for different approaches to model the connection between the chiral node and the wing-box skin	64
4.19	Color contour representation of the total angular displacement of the mesh elements on the deformed structure for different approaches to model the connection between the chiral node and the wing-box skin	65
4.20	Distorted mesh elements in the model	66
4.21	Displacement-force curve for various values of constant artificial damping factor	68
4.22	External work and static dissipation for a damping factor equal to 2×10^{-5}	69
4.23	External work and static dissipation for a damping factor equal to 2×10^{-8}	69

4.24	External work and static dissipation for a damping factor equal to 2×10^{-9}	70
4.25	Vertical displacement v at the tip rib	71
4.26	Model response without the use of inner ribs nor automatic stabilization	72
4.27	Model response without the use of inner ribs and with automatic stabilization	73
4.28	Model response incorporating inner ribs and without automatic stabilization	73
5.1	Baseline model response when the fraction of load applied equals to 47% of the prescribed load (700 N)	76
5.2	External work and static dissipation for a simulation of the baseline configuration	77
5.3	Displacement-force curve for the baseline configuration	77
5.4	Baseline model response when the fraction of load applied equals to 73% of the prescribed load (700 N)	78
5.5	Baseline model response when the fraction of load applied equals to 96% of the prescribed load (700 N)	79
5.6	Displacement-force curve for various values of the wing-box thickness	81
5.7	Detail of the displacement-force curve for various values of the wing-box thickness	82
5.8	Color contour representation of the total angular displacement of the mesh elements on the deformed structure for $t_{\text{box}} = 1.2 \text{ mm}$	82
5.9	Color contour representation of the total angular displacement of the mesh elements on the deformed structure for $t_{\text{box}} = 0.8 \text{ mm}$	83
5.10	Color contour representation of the total angular displacement of the mesh elements on the deformed structure for $t_{\text{box}} = 0.6 \text{ mm}$	84
5.11	Force that induces the structure to collapse as a function of the wing-box thickness	84
5.12	Displacement-force curve for various values of the number of unit cells in the transversal direction	86
5.13	Displacement-force curve for various values of the number of unit cells in the spanwise direction	87
5.14	Colour contour showing the total rotational displacement when the fraction of load applied equals to 81% of the prescribed load (700 N) and $N = 10$	88

5.15	Force that induces the structure to collapse as a function of the wing-box length	89
5.16	Displacement-force curve for various values of the dimensionless chiral ligament eccentricity	91
5.17	Colour contour showing the total rotational displacement when the fraction of load applied equals to 100% of the prescribed load (700 N) and $\varepsilon_{\text{chi}} = 0.1$	91
5.18	Colour contour showing the total rotational displacement when the fraction of load applied equals to 96% of the prescribed load (700 N) and $\varepsilon_{\text{chi}} = 0.0$	92
5.19	Colour contour showing the total rotational displacement when the fraction of load applied equals to 71% of the prescribed load (700 N) and $\varepsilon_{\text{chi}} = 0.001$	93
5.20	Displacement-force curve for various values of the dimensionless chiral node depth	95
5.21	Colour contour showing the total rotational displacement when the fraction of load applied equals to 86% of the prescribed load (700 N) and $B_{\text{chi}} = 30$ mm	95
5.22	Colour contour showing the total rotational displacement when the fraction of load applied equals to 62% of the prescribed load (700 N) and $B_{\text{chi}} = 10$ mm	96
5.23	Force that induces the structure to collapse as a function of the chiral node depth	96
5.24	Displacement-force curve for various values of the chiral node radius	98
5.25	Colour contour showing the total rotational displacement when the fraction of load applied equals to 100% of the prescribed load (700 N) and $r_{\text{chi}} = 17.5$ mm	98
5.26	Force that induces the structure to collapse as a function of the chiral node depth	99
5.27	Displacement-force curve for various values of the chiral ligament half length	100
5.28	Force that induces the structure to collapse as a function of the chiral ligament half length	101
5.29	Displacement-force curve for various values of the chiral structure thickness	103
5.30	Force that induces the structure to collapse as a function of the chiral structure thickness	103
6.1	Overview of the wing FEM model embedded with the compliant wing-box design	105

List of Tables

3.1	Parameters used for the lattice model	28
3.2	Parameters used for the wing-box in C-profile model	30
3.3	Parameters used for the ribs model	32
4.1	Nominal value of the parameters used for the analytical model	48
5.1	Results from the parametric study on the wing-box thickness	81
5.2	Results from the parametric study on the number of unit cells in the transversal direction	85
5.3	Results from the parametric study on the number of unit cells in the spanwise direction	87
5.4	Results from the parametric study on the dimensionless chiral ligament eccentricity	90
5.5	Results from the parametric study on chiral node depth	94
5.6	Results from the parametric study on chiral node radius	97
5.7	Results from the parametric study on chiral ligament half length	100
5.8	Results from the parametric study on chiral structure thickness	102

List of symbols

ε_{chi}	Dimensionless ligament eccentricity	
\hat{x}	Dimensionless coordinate in the spanwise direction (x/L)	
\hat{y}	Dimensionless coordinate in the transversal direction of the computational model ($y_{\text{comp}}/H_{\text{box}}$)	
\hat{z}	Dimensionless coordinate in the chordwise direction of the computational model ($z_{\text{comp}}/W_{\text{box}}$)	
A	Cross sectional area for the analytical model	[mm ²]
A_{rib}	Rib frame width	[mm]
B	Width of the cross section for the analytical model	[mm]
B_{chi}	Chiral node depth	[mm]
c	Artificial damping factor	
$d_{\text{chi-rib}}$	Gap between lattice and inner ribs	[mm]
E, E_1, E_2	Young's modulus in the analytical model	[N/mm ²]
$E_{\text{box}}, E_{\text{rib}}$	Young's modulus for the rib and the wing-box of the computational model	[N/mm ²]
E_{chi}	Young's modulus for the chiral structure of the computational model	[N/mm ²]
e_{chi}	Ligament eccentricity of the chiral structure	[mm]
G, G_1, G_2	Shear modulus in the analytical model	[N/mm ²]
$G_{\text{box}}, G_{\text{rib}}$	Shear modulus for the rib and the wing-box of the computational model	[N/mm ²]
G_{chi}	Shear modulus for the chiral structure of the computational model	[N/mm ²]
H	Height of the cross section for the analytical model	[mm]
$H_{\text{box}}, H_{\text{rib}}$	Height for the wing-box and the ribs of the computational model	[mm]

I_t	Torsional constant	[mm ⁴]
I_y	Second moment of area about y	[mm ⁴]
L	Length of the beam for the analytical model	[mm]
L_{box}	Length of the wing-box in the spanwise direction	[mm]
L_{chi}	Chiral ligament half length	[mm]
M	Number of unit cells in transversal direction	
N	Number of unit cells in spanwise direction	
q_0	Constant shear flow	[N/mm]
q_C	Close section shear flow	[N/mm]
$q_{ }$	Open section shear flow	[N/mm]
Q_z	Force in direction of z	[N]
r	Radial position in the local cylindrical reference system	[mm]
R_{chi}	Ligament eccentricity radius	[mm]
r_{chi}	Chiral node radius	[mm]
S_c	Course mesh size	
S_f	Fine mesh size	
S_{E_y}	First moment of area about y	[mm ³]
t, t_1, t_2	Wall thickness in the analytical model	[mm]
$t_{\text{box}}, t_{\text{rib}}$	Wall thickness for the rib and the wing-box structure of the computational model	[mm]
t_{chi}	Wall thickness for the chiral structure of the computational model	[mm]
u	Displacement along the x direction	[mm]
V	Free-stream air velocity	[m/s]
v	Displacement along the y direction	[mm]
w, w_0	Displacements in direction of z	[mm]
W_{box}	Width of the wing-box	[mm]
$W_{\text{rib,close}}$	Width of the open rib	[mm]
$W_{\text{rib,open}}$	Width of the closed rib	[mm]

x	Coordinate in the spanwise direction	[mm]
y_{ana}, z_{comp}	Coordinate in the chordwise direction for the analytical and computations reference systems	[mm]
z	Perpendicular position in the local cylindrical reference system	[mm]
z_{ana}, y_{comp}	Coordinate in the transversal direction for the analytical and computations reference systems	[mm]
μ	Air dynamic viscosity	[N s/m ²]
ν	Poisson's ratio	
ν_{box}, ν_{rib}	Poisson's ratio for the rib and the wing-box of the computational model	
ν_{chi}	Poisson's ratio for the chiral structure of the computational model	
ϕ	Twist angle, rotational displacement in the $Y - Z$ plane	[rad]
Φ_y	Flexural stiffness	[N mm ²]
ϕ_{tip}	Twist angle at the wing-box tip for the nonlinear simulation	[deg]
ψ	Rotational displacement in the $X - Z$ plane	[rad]
ρ	Air density	[kg/m ³]
θ	Rotational displacement in the $X - Y$ plane	[rad]
$\tilde{\phi}_{tip}$	Twist angle at the wing-box tip for the linear simulation	[deg]
ϑ	Specific twist angle	[deg/mm]

Abbreviations

AAW	Active Aeroelastic Wing
ABS	Acrylonitrile butadiene styrene
AFW	Active Flexible Wing
CAE	Complete Abaqus Environment
CFRP	Carbon Fibre Reinforced Plastic
CMAS	Composite Materials and Adaptive Structures Lab
ETH	Eidgenössische Technische Hochschule

FEM	Finite element method
NASA	National Aeronautics and Space Agency
SMA	Shape Memory Alloy
VSS	Variable Stiffness Spar

Chapter 1

Introduction

Aircraft morphing is a very broad term that can be understood as the modification of the geometry of the aerodynamic surfaces to enhance the performance through the adaptation to the current flight condition. The interest in morphing of aerodynamic surfaces has accompanied aerospace history since the beginning. In 1903, the Wright Brothers successfully completed the first heavier-than-air flight when they designed and built a powered aircraft that achieved a controlled and sustained flight. Their design incorporated a mechanism that provided lateral control by manually changing the twist of the wing. Since then, the necessity of enhanced performance and higher airspeed brought the requirement of stiffer wing structures that would provide increased load carrying capabilities and improved protection against aeroelastic instabilities, among other benefits. As a result, research focused on improving the design of structures that did not exploit the elastic capabilities of the materials used.

On conventional transonic airliners, the need to modify the airflow around the airfoil at different flight conditions is achieved through discrete hinged mechanics such as flaps and ailerons. These mechanisms fulfill its mission in a limited range around the design point while, outside this range, they have a negative influence in the aerodynamics. The necessary discontinuities that these elements produce on the surface advance the boundary layer transition point from laminar to turbulent regime and therefore increase the wing aerodynamic parasite drag.

It is able to modify the airflow without discontinuities on the surface, which would come along with notable reductions in drag and consequently in fuel consumption. Furthermore, these benefits could be applied to diverse flight conditions or flight path alteration requirements. For example, the modification of the wing swept angle is a common practice to obtain an aircraft able to efficiently fly at a wide range of Mach numbers. Another application of wing morphing is the counteracting of the excessive aerodynamic load originated after gust encountering. This is a flight condition under which aircraft experience critical loads that mark the design point for the airframe due to its structural integrity threat. In such an event, an aircraft is flying in turbulent air and a component of the air velocity, normal to the flight path, changes the effective angle of incidence of the aerodynamic surfaces increasing its aerodynamic load. In Figure 1.1, the case of an aircraft encountering a vertical gust is shown. Several mechanisms, which

usually add structural mass, have been developed to withstand this rare but critical scenarios. Such solutions require a rapid modification of the lift distribution that mitigate the increment in aerodynamic load. In some modern transonic aircraft, after a gust encountering, the ailerons of both wings are deflected in such a way that they reduce the local airfoil chamber, reducing as well the lift generated at the wing tip.

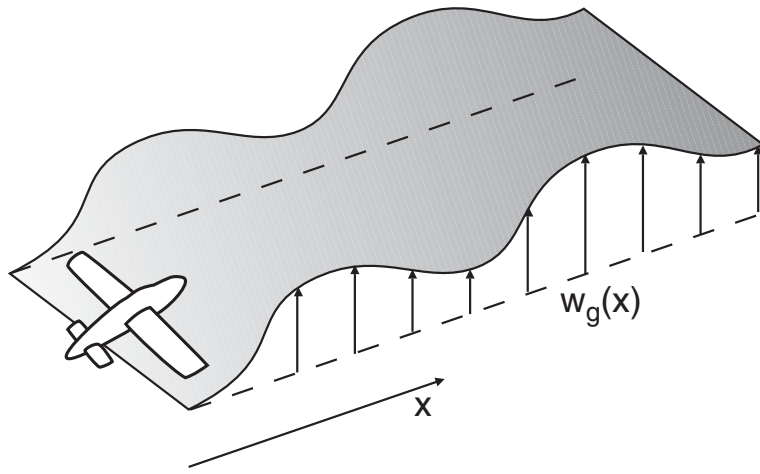


Figure 1.1: Aircraft encountering a vertical gust. [1]

For the particular objective of load alleviation, a wing morphing design needs to show compliance with a time bounded response. Having achieved this requirement, the advantages of using such an approach include weight reduction and/or the no alteration of the aerodynamic surfaces continuity with hinges, which provide reduced operation costs and aerodynamic performance enhancement, respectively.

The present work is a proposal of a novel wing morphing technology. Through wing twist modifications, it is possible to reduce the angle of attack, limit the aerodynamic load on the wings and, consequently, reduce the bending moment at the wing root. The presented concept consists on a mechanism able to modify the torsional stiffness of the wing-box through the inclusion of a variable-stiffness spar. The modification of the effective shear modulus in this element provokes the wing-box shear center shifting and the consequent modification in wing-box torsional stiffness.

The activation of the adaptive spar is an event fully passive and its based on the appearance of elastic controlled instabilities in the structure of the spar. This element is constituted of a lattice of chiral structures, which consists on a network of interconnected nodes and ligaments. Under certain load, some of the ligaments in the lattice start to buckle eventually causing the collapse of the structure due to the sudden reduction of the shear stiffness in the spar. This event induces a sudden variation in the wing-box twist as its torsional stiffness is altered.

The objectives for the work presented in this thesis include the evaluation of the buckling mechanism as a valid trigger for the variable-stiffness spar adaptation and consequent variation of the wing-box twist. In other words, to show how local buckling can affect the global morphing response of the wing.

Chapter 1. Introduction

Furthermore, the possibility of tailoring the buckling phenomena characteristics by varying parameters in the compliant spar is intended to be evaluated. Finally, the wing twist adaptation and the wing root bending moment reduction are evaluated for a more complex model of a wing that incorporates a realistic pressure distribution originated from the fluid-airfoil interaction.



This thesis is organized as follows: succeeding this introduction, the state-of-the-art of the technologies related to the one proposed in this work are presented. Then, the wing-box model, developed to investigate the proposed morphing mechanism, is described in the third chapter, following a characterization of its mechanical properties in the subsequent chapter. The fifth chapter shows the results obtained from the simulations performed on the computational model of the wing-box. After, a chapter dedicated to the aeroelastic analysis of the wing is introduced. The conclusion and outlook complete this thesis.

Chapter 2

State-of-the-art

This chapter presents a review of the current technologies in aircraft morphing in general and in wing twist morphing in particular. Also, a focus on the state-of-the-art of the chiral structures applications is presented.

2.1 Morphing aircraft

Aircraft morphing is a technology that has been part of the history of aviation since the Wright Brothers completed the first controlled and sustained flight of a heavier-than-air powered aircraft in 1903. Their concept of aircraft did not provide importance to built-in stability but absolute control of the aircraft by the pilot. For this reason, they deliberatively designed the aircraft with anhedral wing that make it dynamically unstable to perturbations in sideslip but more maneuverable in the lateral direction. In order to achieve roll control, they decided to incorporate a mechanism that allowed the change the wings twist by pulling from cables, as it can be seen in Figure 2.1. This was the first ever use of morphing of an aerodynamic surface for aircraft control.

New interest has raised in the recent years in aircraft morphing, mainly due to the appearance of new smart materials that allow more efficient mechanical design and that do not necessarily incur in weight increments [3]. Another reason that is pushing forward new aircraft morphing technologies is that missions today are in need of higher aircraft versatility to decrease operational costs in the commercial aviation field. For example, Airbus has recently patented a design of a downwardly foldable wing tip device applicable for a large passenger aircraft [4].

A general classification of different wing morphing concepts can be seen in Figure 2.2: planform modification through variation of sweep angle, span or chord; out-of-plane alteration involving twist, dihedral angle and spanwise bending, and airfoil adjustment achieved by modifications of the airfoil chamber and/or thickness. Under this classification, the morphing technology that is the focus of the work presented in this thesis is located under the out-of-plane branch and twist modification.

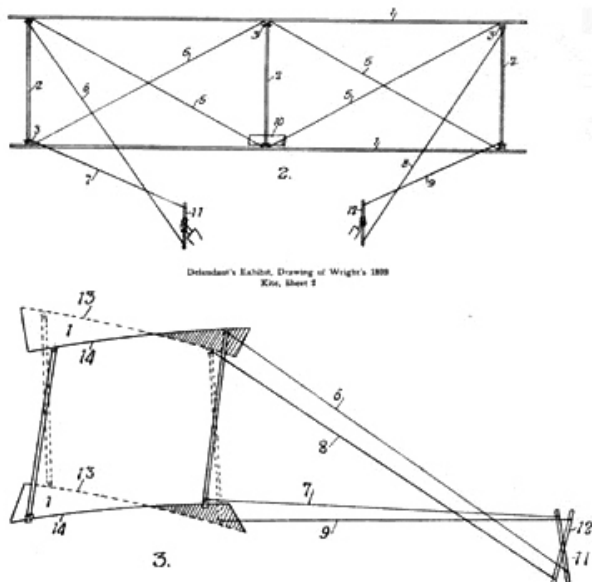


Figure 2.1: Wright Brothers 1899 kite: front and side views, with control sticks. Wing-warping is shown in lower view. [2]

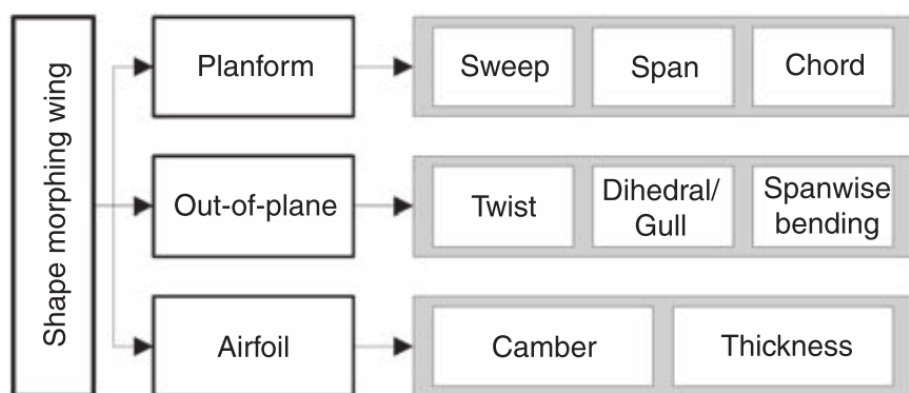


Figure 2.2: Shape morphing wing classification. [5]

In the field of wing morphing through active aeroelastic concepts, the pioneer program of the Active Flexible Wing (AFW) was developed by Rockwell International in the 1980s [6]. Under this program, a design of an aircraft where the wing aeroelastic twist was used to produce the required roll moments for control was presented. This enabled the aircraft to operate at dynamic pressures beyond those where conventional ailerons suffer from the appearance of reversal aeroelastic instabilities. Later, NASA continued with the AFW concept within their Active Aeroelastic Wing (AAW) project which used a modified F-18 fighter named X-53 to perform flight test and assess the viability of the proposed concept. A picture showing this aircraft can be seen in Figure 2.3. The X-53 had its wings modified to reduce the torsional stiffness and had additional actuators added to operate the outboard leading-edge flaps separately from the inboard leading-edge surfaces [7]. Rolling moment was obtained by aeroelastic twist of the wing using trailing-edge control surfaces and leading-edge flaps.



Figure 2.3: The X-53 performing a 360° roll to prove AAW technology. [7]

Following those initial attempts, many additional research literature can be found for other approaches to achieve wing morphing. Many of those, consisted in modifying the wing properties by active means, i.e.: incorporating actuators that introduce energy into the system. Among the vast available literature in this field, it is worth mentioning the advances made in [8] to develop a variable stiffness spar (VSS) concept to control the torsional stiffness as a function of the Mach number and the altitude. Also, in the investigation presented in [9], the adaptive torsional stiffness for a vertical tail was achieved by means of a variable attachment point position. The work presented in [10] showed how roll control of a small aircraft could be achieved by actively twisting its flexible wing. The technology of the shape memory alloys (SMA) has been also exploited in the field of active wing twist morphing, as seen in [11] and [12].

However, wing twist morphing designs may also benefit from geometrically flexible structures if the aeroelastic energy from the airstream can be used to activate the shape changing mechanics. Such an

approach may lead to passive morphings strategies that are always preferred since no additional energy is necessary to be introduced into the system and the usual weight penalties of morphing may be avoided if no additional actuators are needed.

In [13], a passively triggered system to reduce the lift increment that follows a gust encounter using multi-stable elements that are embedded into the airfoil is presented. Other examples of wing twist morphing by passive means are those presented in [14], [15] and [16]. In particular, the technology proposed in these works exploits the capabilities of the chiral structures that feature a negative Poisson's ratio for in-plane strains. A network of these chiral structure is embedded in the rib of the airfoil constituting the deformable part. These chiral structures will be extensively discussed in the next section of the present state-of-the-art review.

Also in the field of passive approaches to achieve wing twist morphing, W. Raither proposed in [17] a novel concept of adaptive aeroelastic tailoring by means of wing-box torsional stiffness modification. In order to achieve this, the shear stiffness of one of the webs that conform the wing-box beam is modified. This induces the section shear centre shifting, which provides an additional torsional deformation for a constant load. This concept is later explained in Section 3.1, as the same working principle is used for the technology presented in this work.

Implementation of the principle proposed by W. Raither in [17], requires a material with controllable in-plane shear modulus. A possible solution is proposed in [18] and consisted in the use of electro-bonded laminates that vary its bending stiffness by means of electrostatic forces applied different at points of the structure. Another approach is presented in [19], and exploits the variable elastic modulus of a polymer web due to temperature changes. This characteristic is provided by the temperature dependence of the elastic modulus of polymers in proximity of their glass transition. Therefore, the proposed concept consists on a semi-passive approach since some energy needs to be spent for the activation of the adaptive interfaces. In [20] the demonstrator shown in Figure 2.4 was built to show the viability of this last technology.

Finally, in [21] the variation of in-plane shear modulus is proposed that can be achieved by inducing elastic instabilities in one of the webs of the wing-box. The component is manufactured with a particular material anisotropy utilizing unidirectional CFRP. The appearance of plate buckling at the root on the specially designed web, as shown in Figure 2.5, induces the shear centre location shifting and the torsional stiffness adaptation, thus leading to a purely passive bending-twist coupling. In [22], the mechanical response was investigated using FE simulations and experimental testing on a manufactured demonstrator of the concept.



Figure 2.4: Inner structure of the experimental wing build to test the concept of adaptive wing-box. [20]

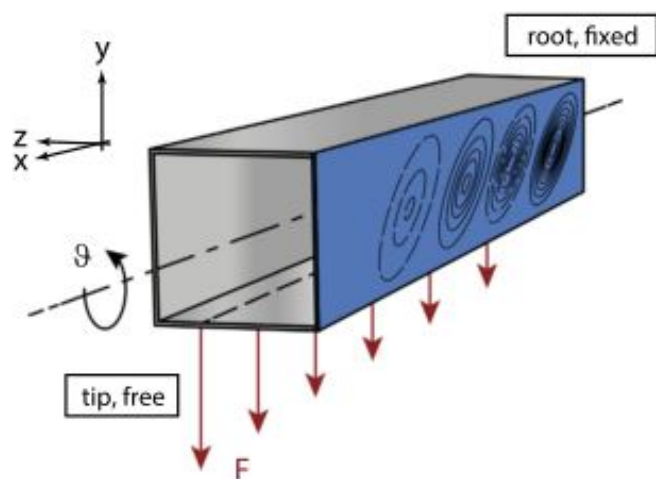


Figure 2.5: Plate buckling on one of the webs of the wing-box beam. The drawing shows a qualitative view of the buckling field. [21]

2.2 Compliant chiral structure

As mentioned in the introduction to this thesis, the proposed technology exploits structures that have recently been used in various research works due to its capabilities as materials with negative Poisson's ratio. Such structures expand laterally when stretched and contract laterally when compressed. In [23], R. Lakes proposed that negative Poisson's ratios can result from a hexagonal microstructure of rotatable nodes and bendable ligaments such as the one shown in Figure 2.6. Such structures are known as non-centrosymmetric, hemitropic, or chiral; they are distinguishable from their mirror image; that is, they cannot be superposed onto them and they are not isotropic.

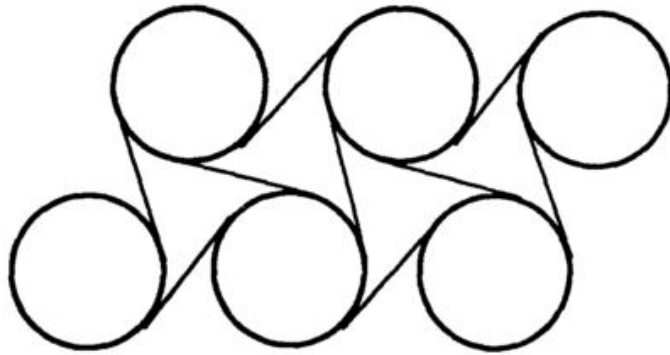


Figure 2.6: Chiral (noncentrosymmetric) hexagonal microstructure of rotatable nodes and bendable ligaments. Poisson's ratio is negative. [23]

In [24], experimental results showed that a honeycomb chiral structure exhibited a Poisson's ratio of -1 for deformations in-plane. Indeed, this behavior was maintained over a significant range of strain, as shown in Figure 2.7, verifying that its Poisson's ratio is independent upon the strain, in agreement with theory.

In [25] the properties of a chiral honeycomb are investigated, a manufacturing process using composite materials is proposed and the increase in the performance of using such materials is shown. Also, the experiments carried out allowed to characterize the possible failure modes of these structures and the nonlinear response when large displacements occur.

Until that moment, most of the work was concentrated in studying the in-plane behavior of the chiral structures. Then, in [26] the flatwise compression behavior of the chiral structures is investigated through FE modeling and simply analytical relations. This is the first consideration of buckling in a chiral structure in some way, in this case it was the out-of-plane buckling behavior based on the similar works presented in [27] and [28] for honeycomb structures. This research was extended by experimental studies in [29] and an anelastic characterization of the buckling phenomena is presented in [30]. The buckling response of chiral honeycombs under a general macroscopic in-plane stress state was more recently investigated from a theoretical point of view in [31].

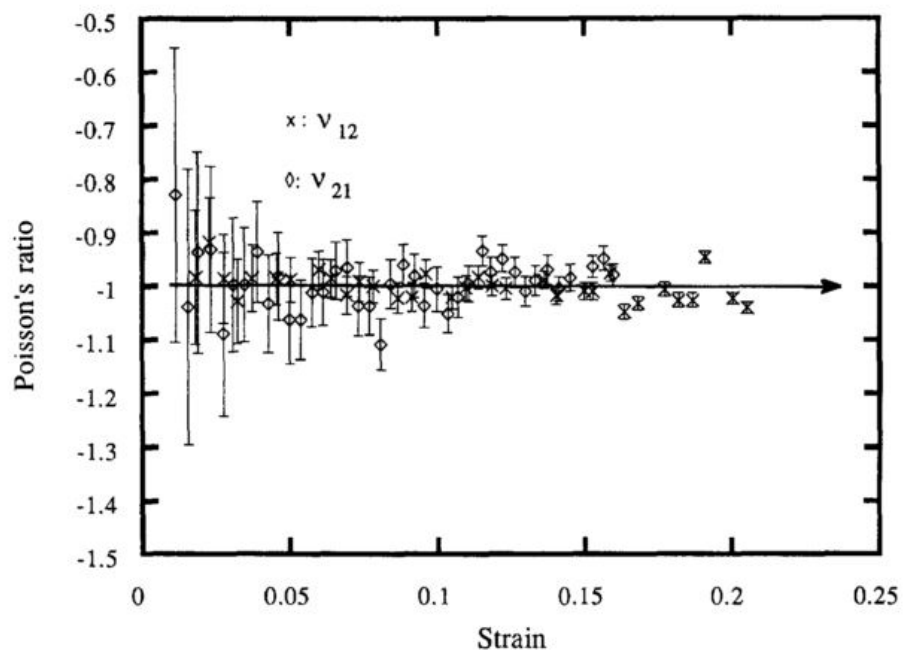


Figure 2.7: Experimental Poisson's ratio v as a function of axial compressive strain on a chiral honeycomb. The error bars represent inaccuracies due to the measurement resolution. [24]

Within the research undertaken at the Laboratory for Composite Materials and Adaptive Structures (CMAS) of the ETH Zürich in the field of variable stiffness structures, a novel chiral topology has recently been proposed. The chiral unit cell is modified by introducing transverse curvature into the ligaments, as shown in Figure 2.8(b). Such design increases the bending stiffness of the ligament and thus of the entire periodic structure. Each ligament posses double eccentricity which changes orientation at the centerline of it, in compliance with an equivalent connection with the cylinders located at the extremes. In [32], preliminary investigations of such structures were experimentally conducted on a conceptual level for a basic triangular chiral structure, as shown in Figure 2.9.

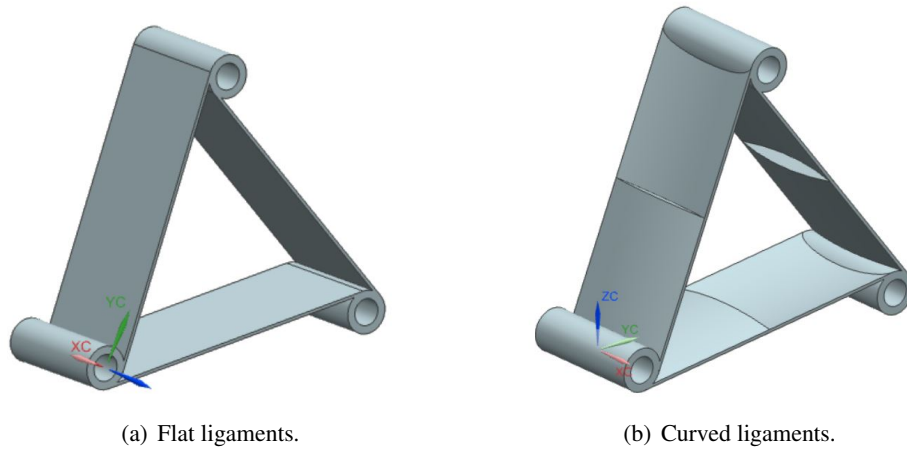


Figure 2.8: Chiral cell elements showing different ligaments curvatures. [32]

This new design of the ligaments is expected to provide additional tailorability over the buckling phenomena occurring on the lattice ligaments. This configuration is the one chosen for the chiral structure that is used in the concept presented in this work.

Different approaches have been followed to exploit the particular characteristics of chiral structures under in-plane strain on aerodynamic elements such as airfoils. In [14], a truss-core configuration with chiral topology, identical to the one shown in Figure 2.10(a), was utilized to design an airfoil for automotive competitions. The concept exploits the elastic deformation of the chiral lattice to alter the airfoil mean chamber line and thus modify the pressure distribution as required for the current desired performance of the car. In [15], a similar configuration was investigated by weakly coupled structural and CFD models, and the local and global deformations were characterized by considerations of the macroscopic chiral configuration. A prototype of the proposed design, shown in Figure 2.11, was manufactured and tested in [16]. Results showed a remarkable tailoring of the chamber morphing performance by means of a limited number of parameters which define the core geometry. The dynamic properties of such chiral truss-core assemblies were investigated in [33].

Recently, A. Airolidi developed the “chiral sail” concept in [34] which exploits the chiral topology of a chiral network embedded into the airfoil rib. The pressure difference between the upper and lower parts of the airfoil promotes the chamber variation as shown in Figure 2.12 and amplifies the lift when the



Figure 2.9: Compression load test on a basic triangular chiral structure. [32]

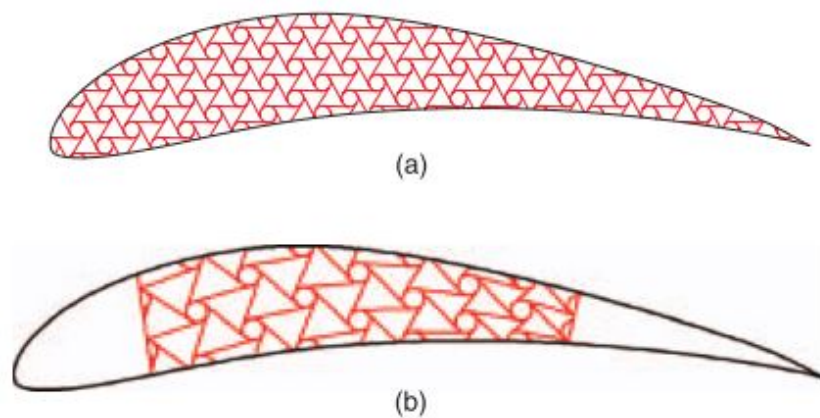


Figure 2.10: Investigated configurations for the truss-core of chiral topology. [15]

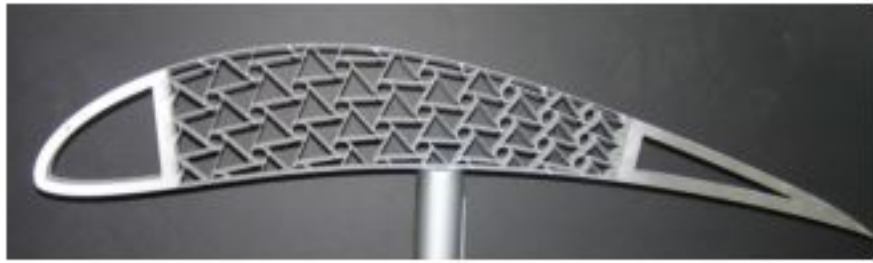


Figure 2.11: Manufactured prototype of a truss-core airfoil with chiral topology. They were manufactured in aluminum, using water-jet cutting techniques. [16]

angle of attack increases. This concept was implemented and validated by testing a demonstrator in [35]. The experimental side of this work showed the difficulties of manufacturing such complex structures.

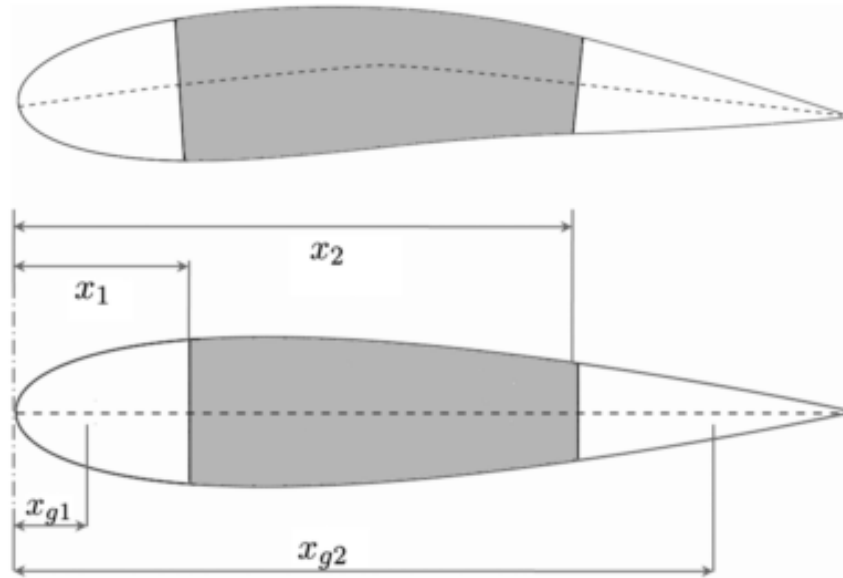


Figure 2.12: Chiral sail concept. The rib of the airfoil is constituted of a network of chiral unit cells. [34]

2.3 Rationale for the thesis

This thesis is part of the current research that it is been carried out at CMAS in seek of wing twist morphing achieved through variable stiffness wing-box structures that acquire this property undergoing elastic instabilities.

As shown in the topic review presented in [36] and [37], the use of buckling-induced technologies is a promising technique to achieve the desired behavior in recent developments of smart structures. Traditionally, elastic instabilities were avoided in the structural designs due to the significant loss of load-carrying capacity and the large deformations occurring as a consequence of such an event. However, in the scope of the so called motion-related applications of buckling-induced technologies, the capability of small perturbations to generate sudden snapping behavior in elastic elements, enables the structure to dynamically change its configuration, being this beneficial for applications such the one considered in the present work. Also, the possibility of minimizing the actuation force required during shape recovery due to the elastic state of the structure becomes interesting.

In parallel, when it comes to the bending-twist shape adaptation by compliant structural designs, some of the solutions already introduced in this chapter are able to modify the wing-box torsional stiffness for a pre-defined shape variation or are optimized for a given actuation lay-out, whereas the adoption of a structural concept such as a chiral lattice offers a wide range of possibilities in terms of tailoring. In particular, the chiral structures that posses curved ligaments are the design option for the concept proposed in this work. This novel characteristic is expected to provide additional control over the buckling appearance and evolution. This design of chiral structure was already manufactured and tested in another project completed at CMAS [38].

Thereby, for the approach presented in this work, the working principle introduced by [17] is combined with the buckling capabilities of the chiral structures exposed in Section 2.2 to conform the proposed principle.

In the scope of this thesis, a full model of the whole wing-box with the compliant variable-stiffness spar is studied. It is the intention to look at the buckling characteristics of the lattice of chiral structures that conforms the spar and the response in twist of the whole assembly. It is expected to see buckling occurring at the same time on several ligaments located close to the root of the wing-box since this is the region that experiences higher shear strain when imposing a force at the tip in the transversal plane. Also, it is envisioned that the buckling phenomena activates a sudden change in the twist of the wing-box. The modification of internal parameters of the chiral structure is expected to show promising tailorability capabilities on the displacement-force curve. Finally, the possibilities of the torsional stiffness adaptation for a wing model under realistic aerodynamic loads is studied.

In order to achieve verification of the previous premises, two models of the wing-box are developed, one numerical and another one analytical. The evolution of the buckling phenomena in the structure is characterized and the effect of the different design parameters on the structure pre-buckling and post-buckling response is assessed. Furthermore, the numerical wing-box model is incorporated into a more complex model of a wing in which the torsional stiffness is dominated by the wing-box. A distribution of

pressure originated from the fluid-airfoil interaction is applied to the wing skin and the structure response in terms of twist adaptation and wing root bending moment is analysed. The aim is to provided a suitable computational environment to achieve in-deep understanding of the proposed working principle and assist the manufacture of a future demonstrator.

It is expected that the proposed technology is suitable for environments where a rapid shape adaptation is required. Such applications may include to increase the critical speed for load alleviation purposes.

Chapter 3

Wing-box model

A model of the whole wing-box including the variable-stiffness spar is developed to study the buckling characteristics of the chiral lattice, the response in twist of wing-box and the tailorability possibilities of that response. In the present chapter the model is presented, which in fact consists in two models one analytical and another one computational.

On first place, the working principle that lays under the proposed technology is presented. Next, the two different models developed to provide fully understanding of the structure response are presented. Firstly, a simple analytical model of a beam with a web featuring variable stiffness properties is presented. This is used to provide fast insight of the role of each of the design parameters on the final mechanical properties of the beam. Important relevance is given to the section's shear centre y_{SC} shifting. This variable determines the magnitude of the resulting torsional moment that acts on the beam as a result of a load applied on the beam's transversal plane, and that induces the beam twist.

Secondly, the computational model is introduced. The different constituting elements are explained together with the boundary conditions, loads and mesh that are used in the simulations.

Finally, the program used to carry out automatic parametric studies is presented, together with its methodology.

3.1 Concept

As it was already introduced in last chapter, the proposed technology to achieve twist morphing through a variable torsional stiffness wing-box is based on the working principle presented in [17] and exploits the buckling characteristics of a lattice of chiral ligaments as a way of varying the effective shear modulus G_{eff} of the adaptive spar of the wing-box.

The basic working principle can be understood considering a closed profile adaptive beam in which

the shear centre is shifted as a result of the variable-stiffness capability of one of the webs. An schematic view of the working principle is shown in Figure 3.1 where an adaptive beam is displayed. In Figure 3.1(a), the four webs that constitute the rectangular profile of the beam have the same shear stiffness $G_1t_1 = G_2t_2$. The double symmetry characteristic of such a configuration indicates that the shear centre is located at the point where the two symmetry axes intersect. For this case, under a load applied on the shear centre, the beam experiences bending deformation with zero twist. On the other hand, when considering the situation shown in Figure 3.1(b) where $G_1t_1 > G_2t_2$, the reduced shear stiffness of the adaptive web produces that shear centre moves along the y direction and towards positive values of y . In this case, if the load is maintained in the same application point as before, the beam experiences bending deformation and negative twist. Correspondingly, for the case shown in Figure 3.1(c) where $G_1t_1 < G_2t_2$, the shifting of the shear centre is towards negative values of y and the beam experiences a positive twisting under the prescribed load.

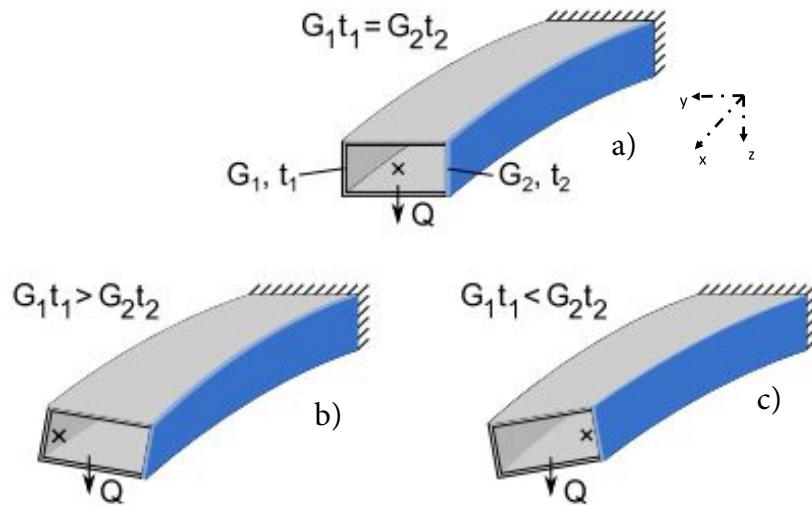


Figure 3.1: Working principle for the adaptive beam. [20]

The bending-twist coupling of the beam can therefore be controlled by the variable-stiffness web. The properties of the web can be modified by either adjusting the shear modulus G_2 or the thickness t_2 of the adaptive web.

In the technology presented in this work, the adaptive web is constituted of a lattice of chiral structures. On these elements, elastic buckling is intentionally induced and the resulting consequence is the reduction of the overall shear modulus G_2 effectively introducing an effective shear modulus $G_{2,\text{eff}} < G_1$. An example of the chiral structure undergoing buckling instabilities on some of the ligaments located at the wing-box root can be seen in Figure 3.2.

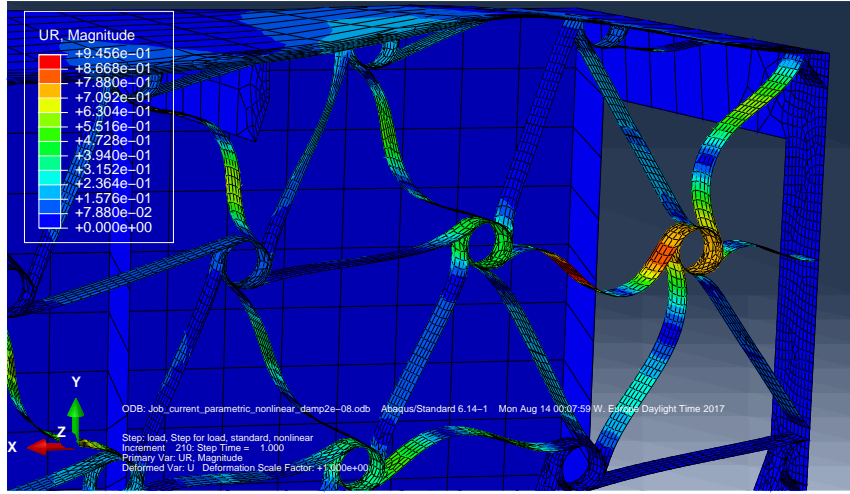


Figure 3.2: Set of chiral ligaments undergoing elastic instabilities at the root of the wing-box.

3.2 Analytical model

The analytical model of the wing-box is described in the present section. An schematic view of the section of the beam can be seen in Figure 3.3. The main dimensions for the section are given by the height H and the width B . Such a structure is characterized by having three elements with identical thickness t_1 , shear modulus G_1 and Young's modulus E_1 . For the element on the right, the adaptive web, the same parameters are t_2 , G_2 and E_2 , respectively.

As explained in Section 3.1, the shear stiffness $G_2 t_2$ of the adaptive web can be modified by varying either thickness t_2 or shear modulus G_2 . For the remaining, it is assumed that $t_1 = t_2 = t$ and therefore the thickness t_2 is not be considered as a modifiable parameter on the adaptive web.

Now, the bending-twisting coupling of the structure is investigated using well-known equations to describe the elastic behavior of thin-wall beam elements. Based on the analytical approach to the problem of a beam bending-twisting coupling followed in [17], it is known that warping can be neglected for a configuration like the one presented in this section.

The bending displacement of the structure is therefore given by Equation 3.1, which a solution of the Bernoulli-Euler equation for a beam:

$$w_b = \frac{QL^3}{6\Phi_y} \left(-\frac{x^3}{L^3} + \frac{3x^2}{L^2} \right), \quad (3.1)$$

where w_b is the displacement along the z direction and Φ_y is the flexural stiffness which is given by Equation 3.2:

$$\Phi_y = \int \int E(y,z) z^2 dy dz. \quad (3.2)$$

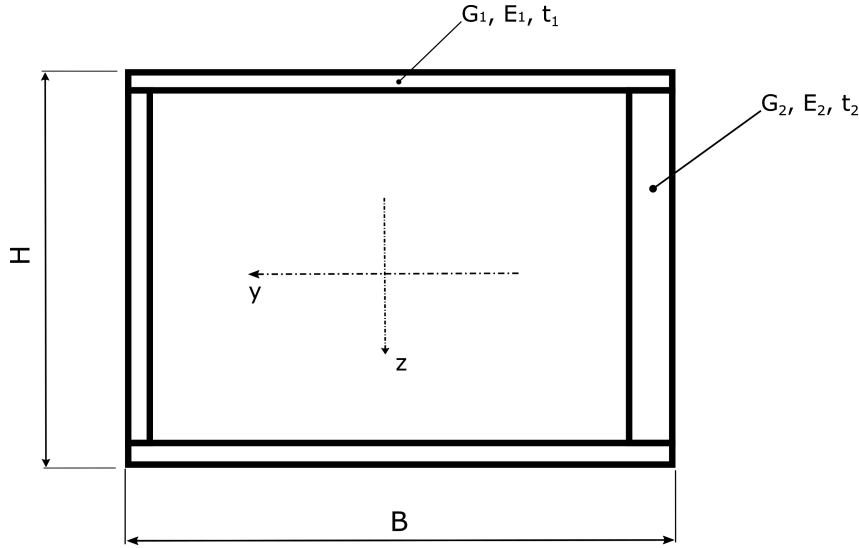


Figure 3.3: Schematic view of the beam closed section. The dimensions are given by the width B and the height H . For the upper, lower and left elements, the wall thickness, shear modulus and the Young's modulus are given by t_1 , G_1 and E_1 , respectively. For the right element, the same parameters are given by t_2 , G_2 and E_2 .

On the other hand, the twist of a beam with closed section can be obtained from the St. Venant expression for the specific twist ϑ , which is shown in Equation 3.3:

$$\vartheta = \frac{d\phi}{dx} = \frac{M_t}{4A_0^2} \oint \frac{ds}{Gt}, \quad (3.3)$$

where A_0 represent the area enclosed by the profile's wall midline, ϕ is the twist of the beam and M_t is the torsional moment applied. Additionally, the torsional stiffness GI_t for the closed section under study is given by the Equation 3.4:

$$GI_t = \frac{4A_0^2}{\oint \frac{ds}{G(s)t(s)}}. \quad (3.4)$$

In order to calculate the specific twist ϑ , it is necessary to evaluate the shear centre position y_{SC} for a given configuration. In order to achieve this, the calculation of the shear flow distribution in the section also needs to be done. To obtain the shear flow $q(s)$, the profile can be considered to be cut at one point, resulting on a opened section. The shear flow $q_{||}(s)$ for this open section case can be calculated using Equation 3.5. The corresponding shear flow for a closed section q_C can be obtained using the Equation 3.6:

$$q_{||}(s) = -\frac{Q_z}{\Phi_y} S_{E_y}(s), \quad (3.5)$$

$$q_C(s) = q_{||}(s) + q_0, \quad (3.6)$$

where Q_z is the force applied in the z direction and S_{E_y} is the so called static moment or first moment of area, which is calculated through the integral shown in Equation 3.7. Also, the variable q_0 represents the shear flow at the boundary that results from the torsion of the beam and can be calculated using the Equation 3.8:

$$S_{E_y}(s) = \int_0^s E(s)t(s)z(s)ds, \quad (3.7)$$

$$q_0 = \frac{Q_z}{\Phi_y} \frac{\oint_s \frac{S_{E_y}(s)}{G(s)t(s)} ds}{\oint_s \frac{1}{G(s)t(s)} ds}. \quad (3.8)$$

Now, the shear centre position in the beam transversal section is calculated for the case of open section. Given that the beam mechanical properties and geometrical dimensions are symmetric around y axis, the shear centre position in the z axis is $z_{SC} = 0$. On the other hand, the shear centre position in the y axis is given by the Equation 3.9:

$$y_{SC,open} = \frac{1}{Q_z} \oint_s q_C(s)r(s)ds, \quad (3.9)$$

where r represents the perpendicular distance to the coordinate origin.

Now, it is necessary that equilibrium exists between the torsional moment due to the shift of the shear centre (caused during the opening of the profile) and the moment due to the torsional shear flow of the closed profile. This condition can be mathematically expressed through Equation 3.10:

$$\begin{aligned} M_t &= Q_z(y_{SC,open} - y_{SC,closed}) \\ &= 2A_0q_0. \end{aligned} \quad (3.10)$$

The above equality enables on one hand the calculation of the closed section shear centre position $y_{SC,closed}$ using Equation 3.11:

$$y_{SC,closed} = y_{SC,open} - \frac{2q_0A_0}{Q_z}, \quad (3.11)$$

and the the calculation of the torsional moment M_t acting on the beam on the other hand using Equation 3.12:

$$M_t = Q_z(y_{load} - y_{SC,closed}), \quad (3.12)$$

that considers the coordinate y_{load} of the point where the load is applied.

Finally, once the torsional moment M_t acting on the beam is known, it is possible to calculate the beam twist $\phi(x)$ using Equation 3.3 and considering that $\phi(x) = \vartheta x$.

3.3 Computational model

The computational model of the wing box is built using Abaqus CAE commercial software. It consists on three main elements: the wing-box with C-profile, the lattice constituted of the chiral elements and a set of ribs. A general overview of the assembly of the different parts can be seen in Figure 3.4.

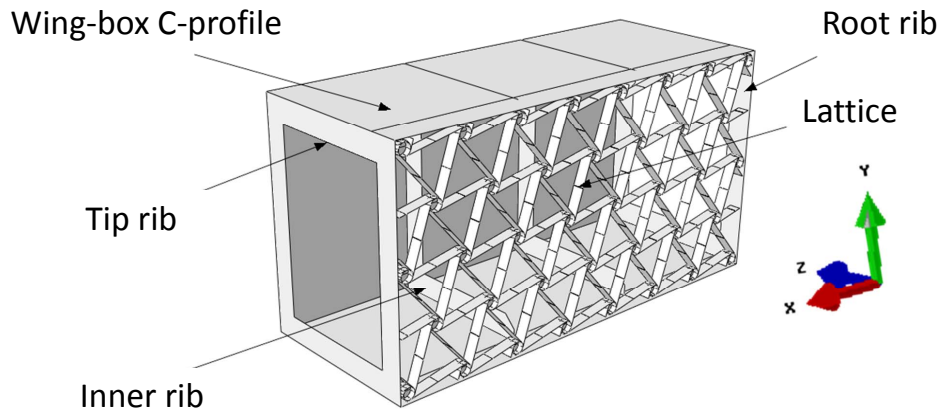


Figure 3.4: General assembly configuration for the computational model. The different parts for the general configuration include the wing-box profile, the lattice of chiral elements and a set of ribs that can be located at the tip, at the root or in between this borders.

The discretization of the structural element was done using continuum shell elements as the basic constituting part. An sketch of a continuum shell element as defined in Abaqus can be seen in Figure 3.5.

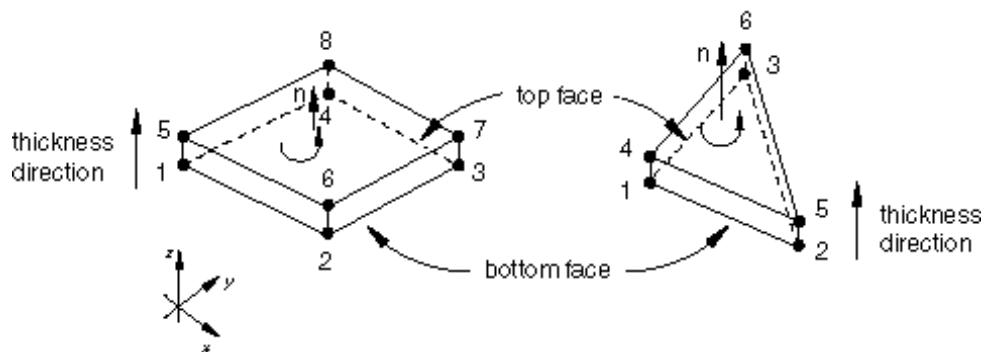


Figure 3.5: Default normals and thickness direction for continuum shell elements in Abaqus. [39]

3.3.1 Sub-parts and parametrization of the model

Lattice of chiral elements

The model of the lattice structure is constituted of a network of rigid nodes interconnected by ligaments. At each node, there are six ligaments attached in a uniform distribution that leaves an angular separation of 60° between consecutive attachment points. This network constitutes a lattice of chiral elements. An overview of this part can be seen in Figure 3.6. The lattice structure is divided in an integer number of unit cells in the longitudinal (spanwise) and transversal directions. These parameters are identified with the variables N and M for the longitudinal and transversal directions, respectively. In Figure 3.7, an sketch of the internal division for $N = 8$ and $M = 3$ is shown. It displays a set of horizontal rectangles that represent each of the transversal M divisions while the set of vertical rectangles correspond to each of the N longitudinal divisions.

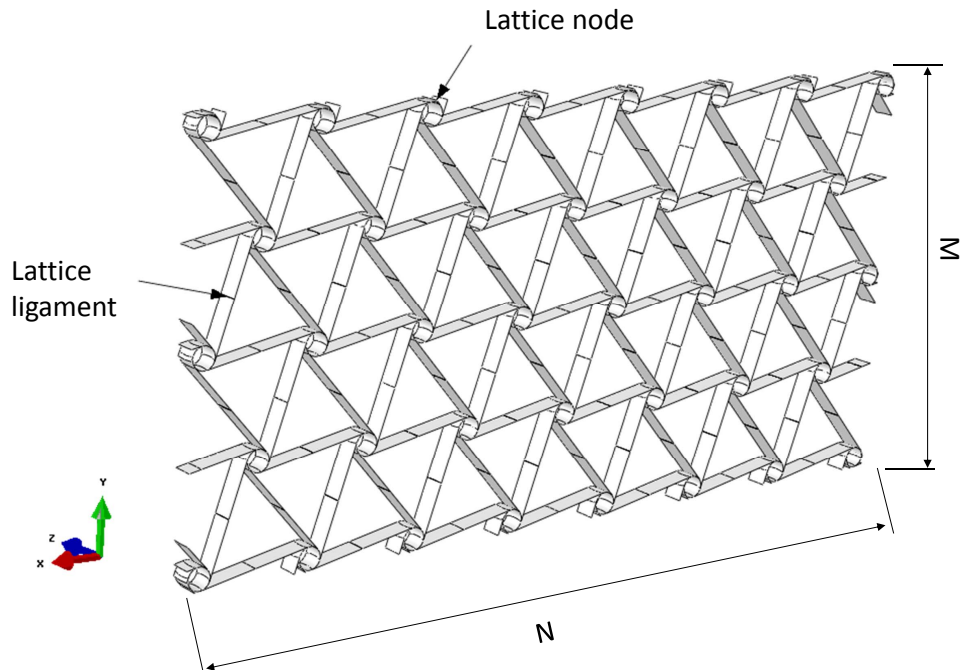


Figure 3.6: Overview of the lattice of chiral elements part. The parameters N and M represent the number of unit cells in the longitudinal (spanwise) and transversal directions, respectively.

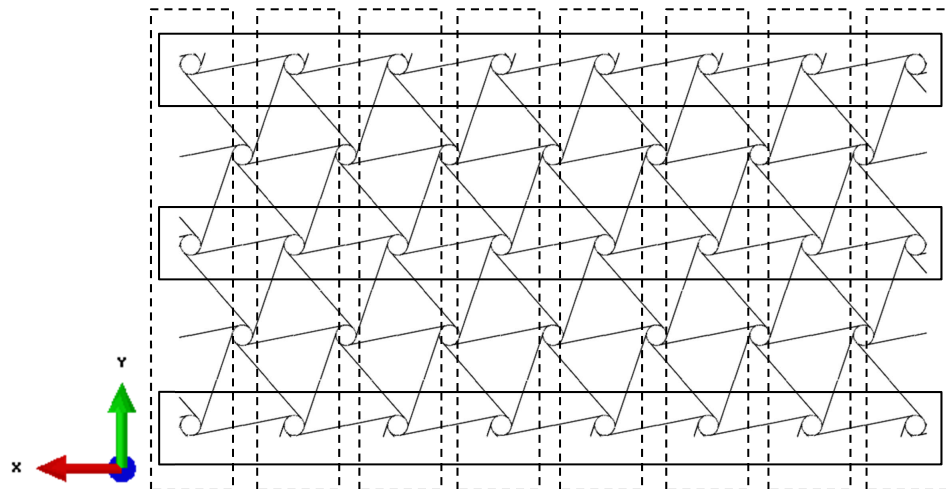


Figure 3.7: Division of the lattice structure in cell units. The sketch shows a lattice with $N = 8$ and $M = 3$. The set of horizontal rectangles represent each of the transversal M divisions while the set of vertical rectangles correspond to each of the N longitudinal divisions.

Furthermore, the internal geometry in the chiral structure is determined by a number of parameters: the thickness t_{chi} , the ligament eccentricity e_{chi} , the ligament half length L_{chi} , the lattice node depth B_{chi} and the lattice node radius r_{chi} . The geometrical meaning of these variables can be seen in the sketch shown in Figure 3.8. The thickness t_{chi} applies for both the ligaments and the lattice nodes geometries. The eccentricity e_{chi} is expressed as the dimensionless parameter ε_{chi} which is obtained from $\varepsilon_{\text{chi}} = e_{\text{chi}}/B_{\text{chi}}$.

In the sketch shown in Figure 3.8 an additional dimension variable appears, the ligament eccentricity radius R_{chi} which is dependent on the ligament eccentricity e_{chi} and the lattice node depth B_{chi} as shown in Equation 3.13.

A summary of all the parameters introduced to characterize the chiral lattice structure together with their units and nominal values is shown in Table 3.1.

$$R = \frac{e_{\text{chi}}^2 + \frac{B_{\text{chi}}^2}{4}}{2e_{\text{chi}}} \quad (3.13)$$

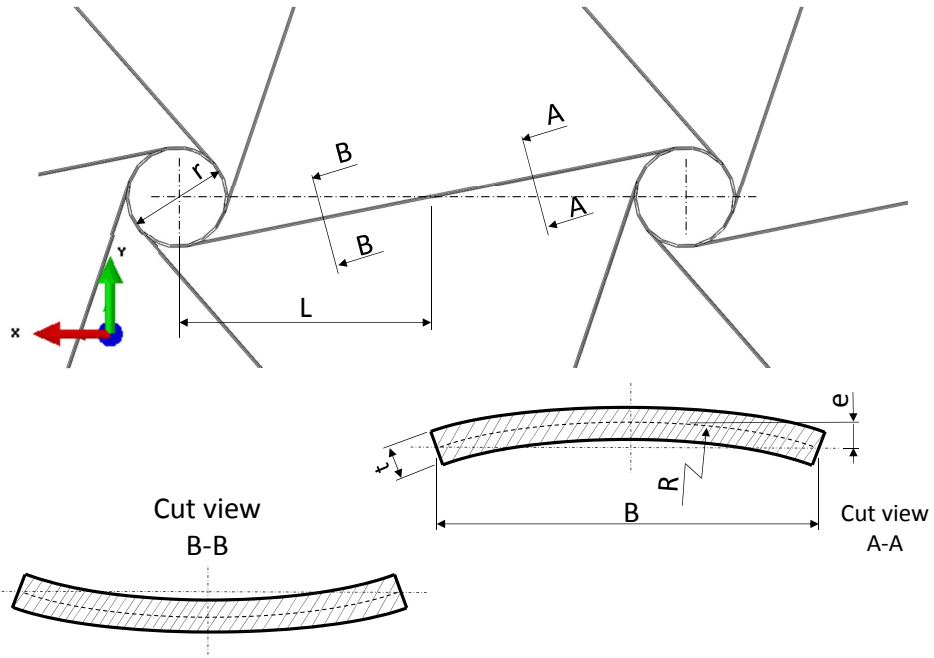


Figure 3.8: Internal parameters of the chiral structure in the lattice. The geometry is characterized by the the ligament eccentricity e_{chi} , the ligament half length L_{chi} , the lattice node depth B_{chi} , the lattice node radius r_{chi} and the thickness t_{chi} . The ligament eccentricity radius R_{chi} which is dependent on the ligament eccentricity e_{chi} and the lattice node depth B_{chi} , as shown in Equation 3.13

Parameter	Symbol	Units	Nominal value
Dimensions			
Number of unit cells in spanwise direction	N		8
Number of unit cells in transversal direction	M		3
Dimensionless ligament eccentricity (e/B)	ε_{chi}		0.01
Node radius	r_{chi}	mm	10
Node depth	B_{chi}	mm	20
Ligament eccentricity radius	R_{chi}	mm	250.1
Ligament half length	L_{chi}	mm	50
Thickness	t_{chi}	mm	0.5
Material (ABS)			
Young's modulus	E_{chi}	N/mm ²	3100
Poisson's ratio	ν_{chi}		0.3

Table 3.1: Parameters used for the lattice model. The mechanical properties of the material used correspond to ABS, which is a common thermoplastic polymer.

Wing-box in C-profile

The model of the wing-box consists on a beam with open C profile. The length L_{box} and height H_{box} of the part are determined from those of the lattice of chiral elements. Therefore, the tailorable parameters for this part are the width W_{box} , the thickness t_{box} and the mechanical properties E_{box} and ν_{box} of the material used.

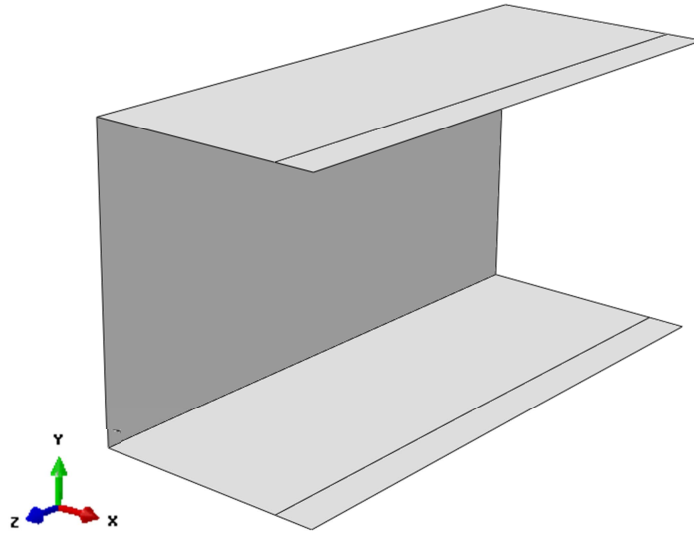


Figure 3.9: Overview of the wing-box in C-profile part

In the sketch shown in Figure 3.10 it is possible see the geometrical meaning of the parameters introduced in the previous paragraph. Additionally, the Table 3.2 shows its units and nominal values.

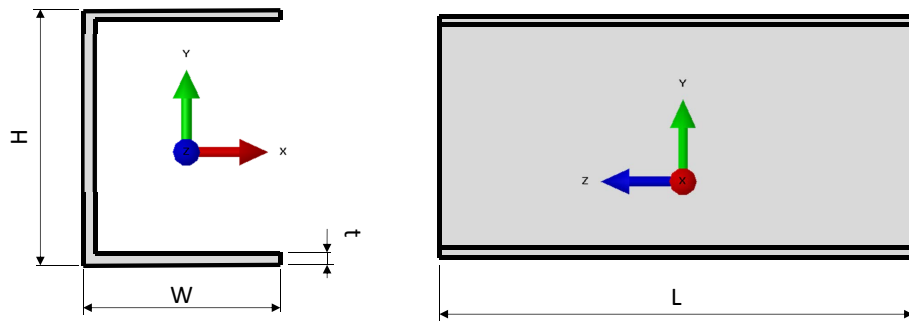


Figure 3.10: Internal parameters of the wing-box C-profile part. The geometry of the part is determined by the length L_{box} , height H_{box} , the width W_{box} and the thickness t_{box} .

Parameter	Symbol	Units	Nominal value
Dimensions			
Wing-box height	H_{box}	mm	383.27
Wing-box length	L_{box}	mm	743.86
Wing-box width	W_{box}	mm	300
Wing-box thickness	t_{box}	mm	0.8
Material (Aluminum)			
Young's modulus	E_{box}	N/mm ²	69000
Poisson's ratio	ν_{box}		0.3269

Table 3.2: Parameters used for the wing-box in C-profile model. The mechanical properties of the material used correspond to standard aluminum. The value of the wing-box height H_{box} and the wing-box length L_{box} are not independent but are calculated based on the transversal and longitudinal dimensions of the chiral lattice structure, respectively.

Ribs

In order to provide the wing-box with additional stiffness in the transversal direction, the addition of ribs is considered. For its design, two different approaches are studied. One considers an open profile design while the other considers a close profile design, as shown in Figure 3.11. These could be installed at the tip and/or root of the wing box; and also, in the interior of the wing-box. For those ribs located in this last position, the open section design is preferred to avoid interferences with the lattice of chiral structures. For the ribs located in an outer position, considerations regarding the optimal design choice will be presented in Subsection 4.2.6.

The ribs design is characterized by the widths $W_{\text{rib},\text{close}}$ and $W_{\text{rib},\text{open}}$, and the height H_{rib} . The height H_{rib} and the width of the closed section design $W_{\text{rib},\text{close}}$ are set to be equal to those of the wing-box: $H_{\text{rib}} = H_{\text{box}}$ and $W_{\text{rib}} = W_{\text{rib},\text{close}}$, respectively. The value of $W_{\text{rib},\text{open}}$ is calculated as follows:

$$W_{\text{rib},\text{open}} = B_{\text{chi}} + W_{\text{rib},\text{close}} + d_{\text{chi-rib}}$$

where $d_{\text{chi-rib}}$ represents the gap between the right edges of the inner rib and the lattice chiral structure. This gap ensures that there are not any interferences in between the rib and the lattice chiral structure. The value of this parameter was set to a fix value of $d_{\text{chi-rib}} = 20\text{mm}$. Additionally, the frame width A_{rib} and the thickness t_{rib} allow design modifications.

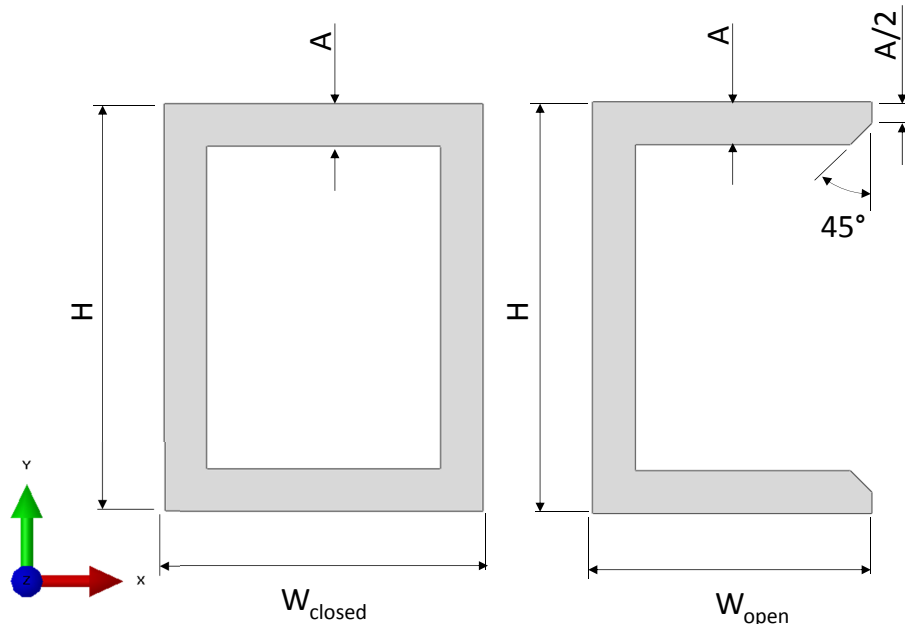


Figure 3.11: Internal parameters of the two different ribs parts. The angle edge for the open section configuration is set to a fix value of 45° to simplify the design and assuming this area of the rib is not critical for the rib duty.

The nominal values of all the parameters involved in the ribs design can be read in Table 3.3. The material choice aimed for a configuration stiffer than the wing-box to ensure no out-of-plane deformation of the rib. For this reason, the material chosen is steel.

Parameter	Symbol	Units	Nominal value
Dimensions			
Rib height	H_{rib}	mm	383.27
Closed rib width	$W_{\text{rib,close}}$	mm	300
Frame width	A_{rib}	mm	30
Rib thickness	t_{rib}	mm	2
Material (Steel)			
Young's modulus	E_{rib}	N/mm ²	200000
Poisson's ratio	ν_{rib}		0.25

Table 3.3: Parameters used for the ribs model. The material of choice is steel. The value of the rib width $W_{\text{rib,close}}$ and the height H_{rib} will be equal to the wing-box width W_{box} and to the chiral lattice structure height, respectively.

3.3.2 Computational model mesh characteristics

In the present section, the characteristics of the model spatial discretization are presented. The mesh is unstructured and it is auto-generated by Abaqus CAE for the whole assembly. The elements are a combination of quadratic and tetrahedral with 4 and 3 nodes, respectively. Different mesh elements size are assigned to different parts of the model depending of the geometrical complexity of the area.

In Figure 3.12, it is possible to distinguish the two regions that are assigned with different mesh element size: the lattice of chiral structures and the close region of the wing-box skin are assigned with a fine mesh size while the remaining model is assigned with a course mesh size, typically one order of magnitude greater. This introduces two new parameters that are used to modify the mesh size of the different regions:

- S_f : Fine mesh size, typically equal to 3 mm.
- S_c : Course mesh size, typically equal to 30 mm

The selection of this typical values for S_f and S_c are obtained after a number of trial-error attempts to achieve convergence in the nonlinear simulations. As part of the program built to execute the nonlinear simulations, the mesh size is automatically changed if convergence is now achieve. The methodology followed by this program is explained in detail in Subsection 3.3.8.

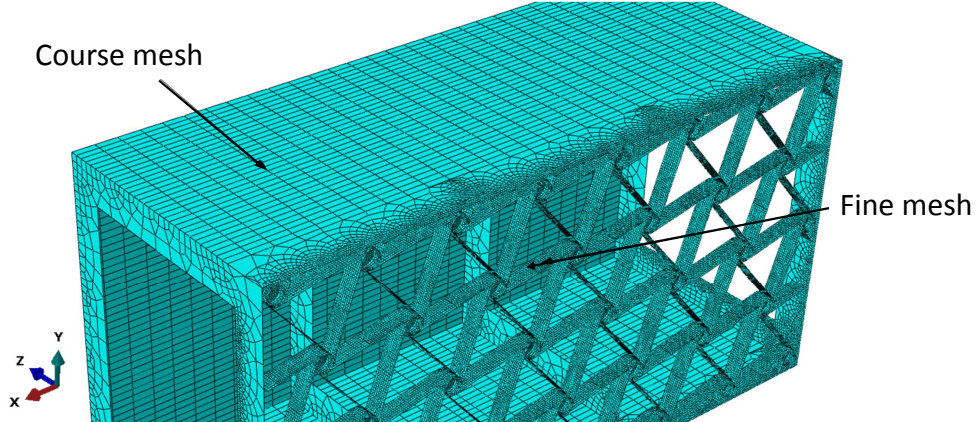


Figure 3.12: Internal parameters of the two different ribs parts. Different mesh element size are assigned to different parts of the model. The lattice structure is assigned with a fine mesh element size while the wing-box is assigned with a course mesh element size.

3.3.3 Load definition

The computational model allowed different possibilities in terms of the load introduction. Among all of them, it was decided to locate the load introduction points on the upper flange of the ribs. The reason for this is the replicate how the load will be introduced in a future manufactured demonstrator of the wing-box.

Therefore, the number of load introduction points had an upper bound equal to the number of ribs available. For the baseline configuration, this number equals to three, one close rib at the tip of the wing-box and two open ribs in the inner part of the wing-box. Another possibility is to vary the position in the chordwise direction of load introduction point or points. In Figure 3.13 it can be seen the location of the load introduction points when they are distributed among the three available ribs and their position in the chordwise direction is equal to $z/ = 0.8$.

In Subsection 4.2.2, the differences in the response of the structure depending on the number of load introduction points that their position in the chordwise direction are discussed.

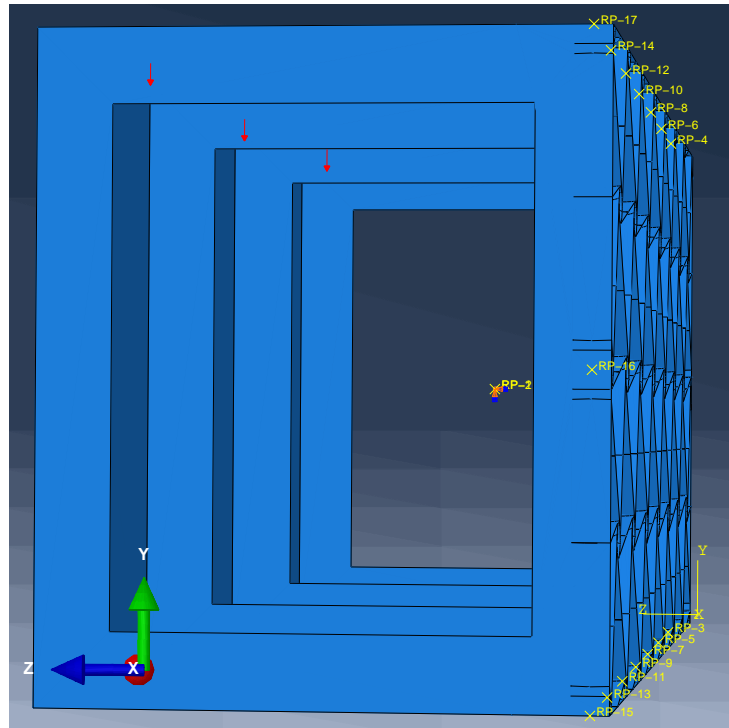


Figure 3.13: Load introduction points located on the upper flange of the tip rib and the two inner ribs.

3.3.4 Boundary condition

The boundary condition for the whole assembly is the one shown in Figure 3.14. It consisted in a kinematic coupling similar to the one introduced in Section 3.3.1 to model the rigid body behavior of the lattice nodes. In this case, the kinematic coupling is establish between a reference point located approximately at the centre of the root rib and the faces of this mentioned rib. The reference point acts as a master node while the mesh nodes located at the faces of the rib are the slave nodes. The reference point is next fixed in all its degrees of freedom using the corresponding boundary condition Abaqus module.

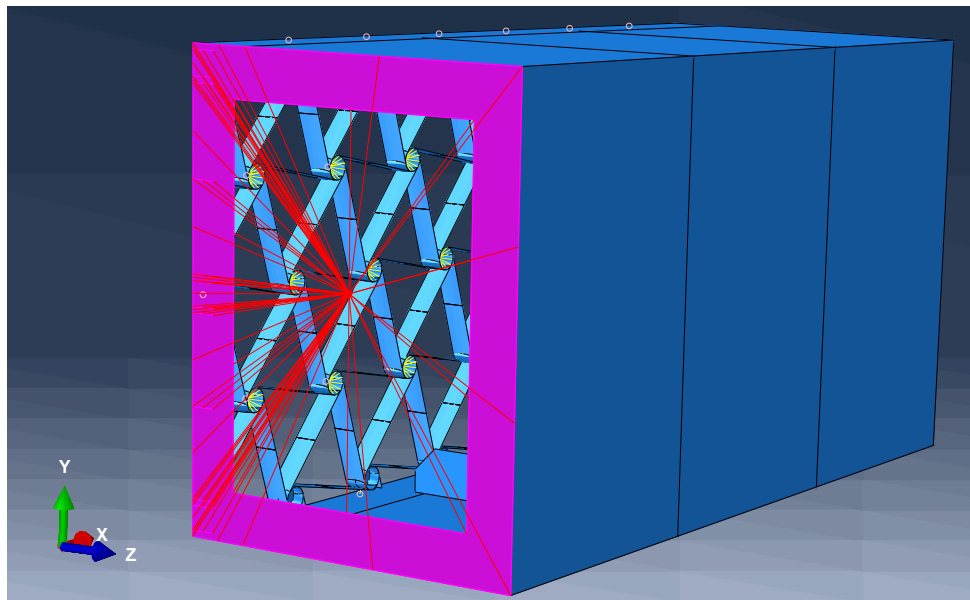


Figure 3.14: Boundary condition for the model. The condition is establish through a coupling interaction between a reference point and the faces of the rib at the root. The reference point is fixed in all its degrees of freedom using the corresponding boundary condition Abaqus module.

3.3.5 Lattice nodes rigid body modeling

The lattice nodes is one of the essential parts of the lattice of chiral elements. These are only constrained in the rotation around its own axis by the ligaments connected to them. For the modeling, they are assumed to behave like a rigid body. In Figure 3.15, a closer look to the chiral nodes can be seen, showing two different approaches to manufacture a node that would behave like a rigid body compared with the rest of the structure.

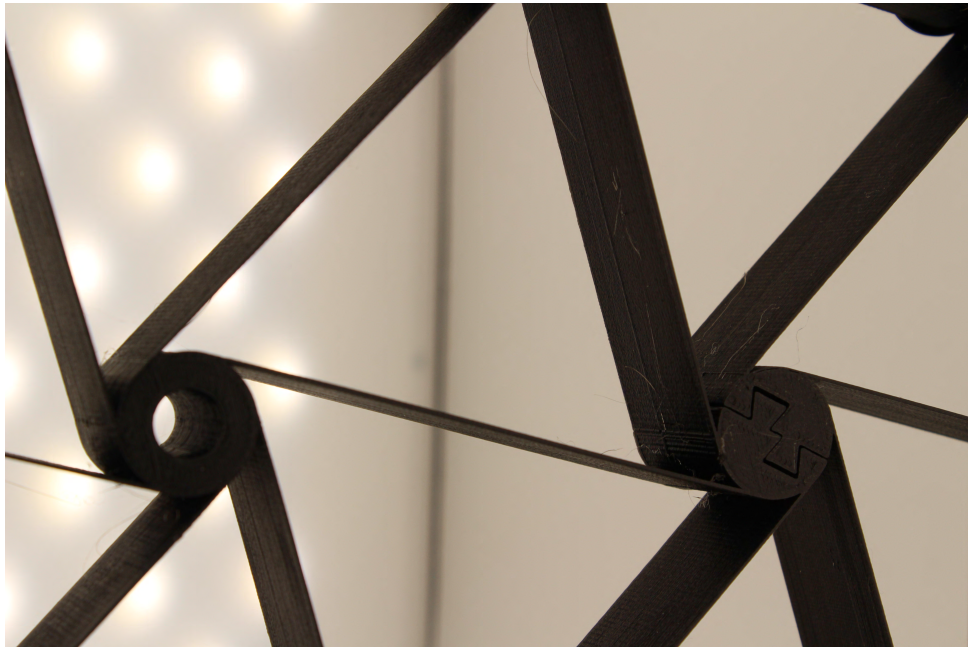


Figure 3.15: Picture of the manufactured chiral lattice nodes. The figure shows two different approaches followed to manufacture the nodes. The one on the right was the standard one showing a cylinder with a thickness bigger than the thickness of the chiral ligaments $t_{\text{node}} \gg t_{\text{ligaments}}$. On the left, an alternative approach is followed in order to allow the assembly of the chiral lattice that is not manufactured as a unique piece. The photography was taken from the demonstrator built by [38].

In the Abaqus model, different approaches were followed to model the chiral nodes together with its rigid body feature. The first one was to create a coupling condition using Abaqus corresponding module. In particular, a kinematic coupling is enabled. A kinematic coupling constrains the motion of one or more coupling nodes, also called slave node or nodes, to the rigid body motion of a reference node, also called master node. It is imposed by eliminating degrees of freedom at the coupling nodes. In Figure 3.16, an example of a kinematic coupling can be seen.

For the considered case, the coupling nodes are those mesh nodes located at the faces of the lattice nodes and the master node is the reference point located in the center of the lattice node. In order to achieve the rigid solid behavior, all the degrees of freedom translational and rotational are coupled. In Figure 3.17, an overview of this coupling condition can be viewed.

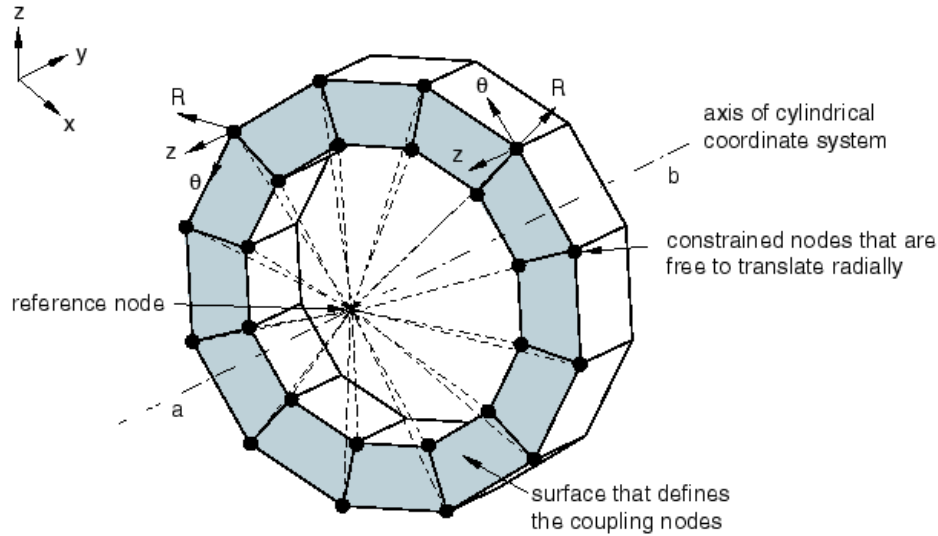


Figure 3.16: Kinematic coupling constraint. The sketch illustrates the use of a kinematic coupling constraint to prescribe a twisting motion to a model without constraining the radial motion. In this case, a local cylindrical reference system is used and the constrained nodes have two degrees of freedom coupled to those of the reference node, the angular position θ and the position along the z axis. The coupling nodes are therefore free to translate radially, varying R . [39]

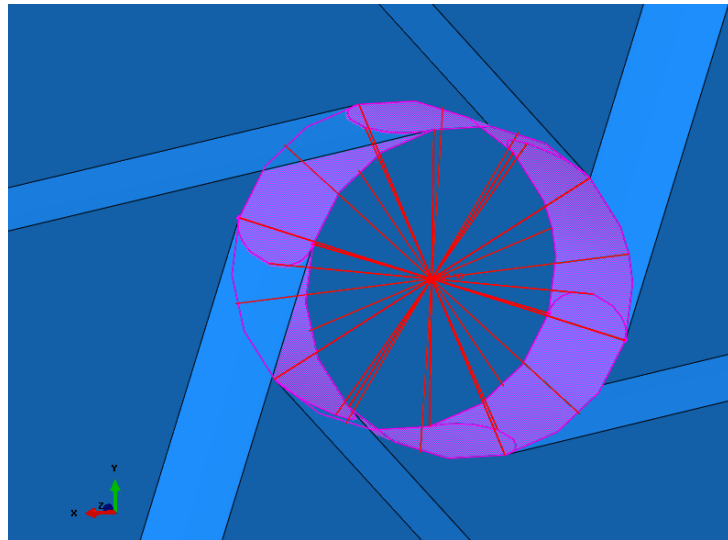


Figure 3.17: Overview of the elements that are involved in the coupling condition at the lattice nodes. The coupling condition was defined in between the mesh nodes located in the faces of the lattice node and a reference point located in the middle. All the degrees of freedom translational and rotational are linked.

Another approach consisted in embedding an additional part inside the lattice nodes to add rigidity to the element. The proposed design of such a part, which is referred as tyre from now on, can be seen in Figure 3.18. The internal dimensions of this element are shown in Figure 3.19. Its dimensions are dependent on parameters of the chiral lattice, that is, the thickness of the tyre is equal to that of the chiral lattice $r_{\text{tyre}} = r_{\text{chi}}$ and the same occurred for the height B_{tyre} and the radius r_{tyre} which were $r_{\text{tyre}} = r_{\text{chi}}$ and $B_{\text{tyre}} = B_{\text{chi}}$. The added rigidity was obtained as a result of considering a different material for the tyre such that the Young's modulus of the two parts verify the condition $E_{\text{tyre}} \gg E_{\text{chi}}$. Once, the connection is completed, the resulting merged part looked as shown in Figure 3.20.

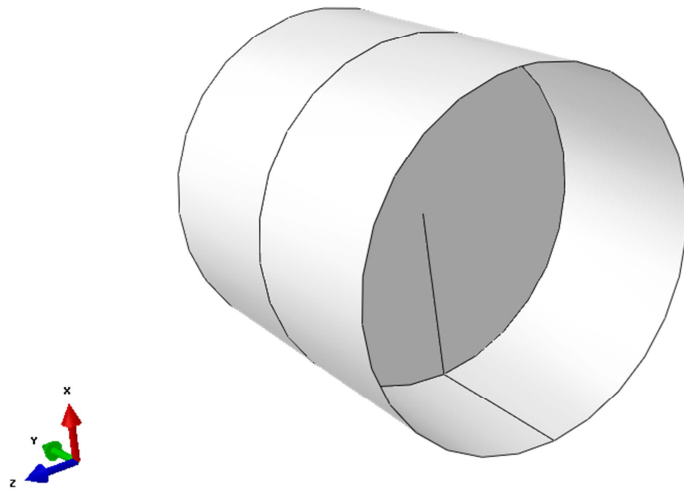


Figure 3.18: Overview of the tyre part.

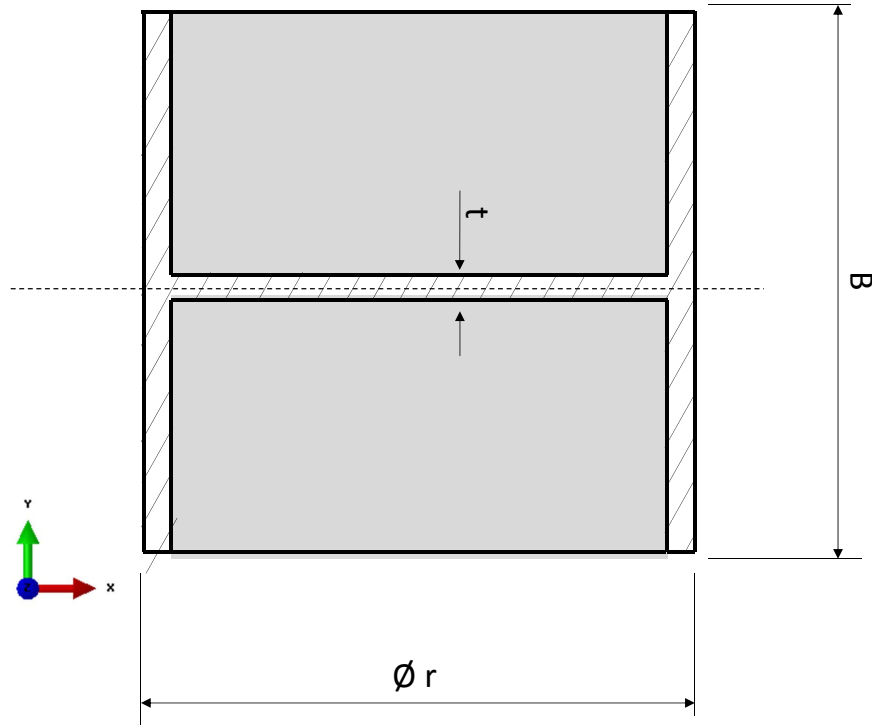


Figure 3.19: Internal parameters of the tyre part. The sketch shows a transversal cut to the part. The tyre is characterized by the radius r_{tyre} , the height B_{tyre} and the thickness t_{tyre} . All this parameters are set to be equal to the corresponding ones in the lattice nodes, therefore: $r_{\text{tyre}} = r_{\text{chi}}$, $B_{\text{tyre}} = B_{\text{chi}}$ and $t_{\text{tyre}} = t_{\text{chi}}$.

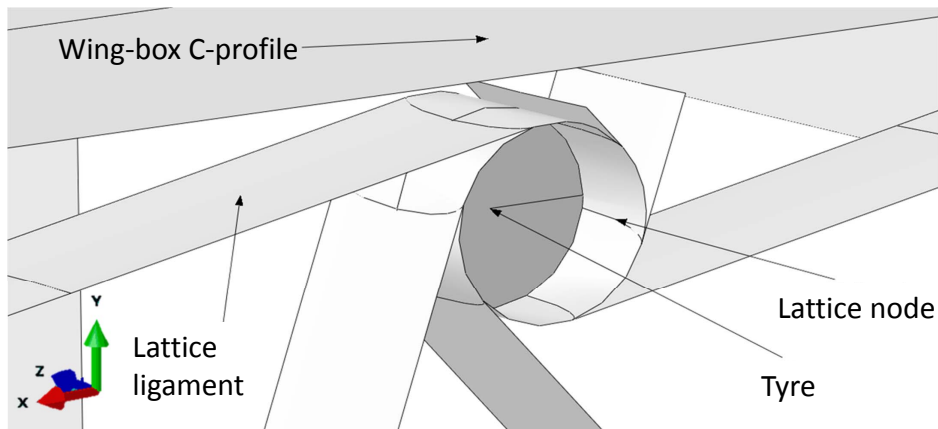


Figure 3.20: Overview of the connection between tyre and lattice node. The tyre will be embed inside the lattice node.

3.3.6 Connection between the wing-box skin and the chiral lattice

In the present subsection, the computational modeling of the connection between the lattice nodes and the wing-box skin is presented. This is an unavoidable transition from the lattice of chiral structures comprised of nodes and ligaments to the skin of the wing-box. Loads are transmitted to the lattice through this attachment points that is why its design results crucial. Three different configurations are studied:

Blocked translation and rotation The lattice nodes have all its degrees of freedom restricted. In this case, the lattice nodes are cut by half and are directly attach to the wing-box skin.

Blocked translation and free rotation The lattice nodes are free to rotate around its own axis. The translation displacement parallel to the skin is restricted. An sketch showing this type of connection can be viewed in Figure 3.22. This configuration was the one chosen for the demonstrator built in the Figure 3.21.

Free translation and rotation Now the lattice nodes are also allowed to translate parallel to the skin. This configuration is schematically represented in Figure 3.23.



Figure 3.21: Detail of the connection between the lattice nodes and the skin. The picture shows the type of connection chosen for the manufactured demonstrator of the lattice. The lattice nodes is allowed to rotate around its own axis but cannot translate parallel to the skin. This photography was taken from the demonstrator built by [38].

Depending on the type of connection considered, it is necessary to leave a space gap between the chiral node and the wing-box skin. For the most restrictive case, in which the connection between the lattice structure and the wing-box is rigid, the lattice node was cut by half and directly attached to the

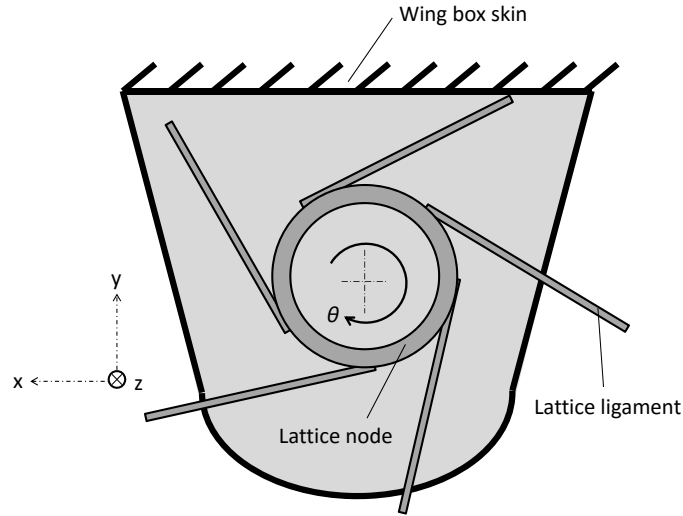


Figure 3.22: Blocked translation and free rotation connection between the lattice nodes and the skin. In this case, the only degree of freedom of the lattice node that it is not restricted is the rotation around its own axis, that is the rotational displacement θ around the direction z .

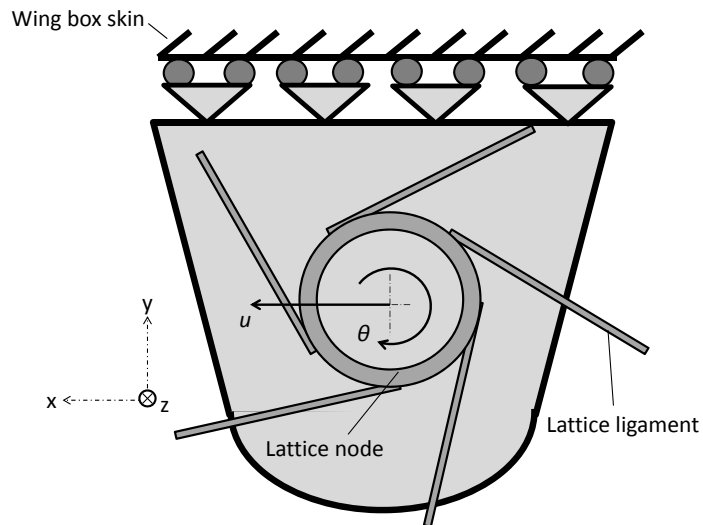


Figure 3.23: Free translation and rotation connection between the lattice nodes and the skin. For this case, the unrestricted degrees of freedom of the lattice nodes are the rotational displacement θ around its own axis, i.e.: the direction z ; and the displacement u parallel to the wing-box wall, i.e.: along the direction x .

wing-box skin, as shown in Figure 3.24. In this case, there is no gap between the two elements. However, when the allowance of the node rotation is implemented, it is necessary leave a gap between the elements. It becomes then necessary to use the interaction module provided by Abaqus CAE to model the different connections.

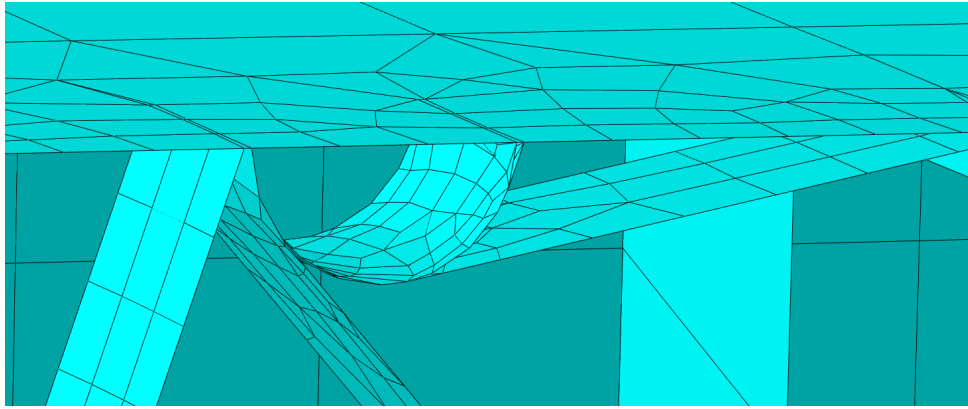


Figure 3.24: Simple rigid connection between the wing-box skin and the chiral node. In this case, none of the possible displacements of the chiral node are left unrestricted. Instead, a solid connection is established through the physical connection and the addition of a coupling condition between a reference point and the mesh nodes located on the lattice node face.

When modeling a type connection between the wing-box skin and the lattice node that allows the free rotation of this last element around its own axis, it is also necessary to preserve the rigid body behavior of the lattice node. For this reason, a tyre part as described in Subsection 3.3.1, is implemented to model both the rigid body characteristics of the lattice node and the allowance of relative displacement between this element and the wing-box skin above it. Therefore, the tyre part is embedded at the centre of each of the lattice nodes located at the border of the lattice structure, as it is shown in Figure 3.20. Then, a coupling constraint is established between a mesh node in the middle of the tyre that acts as slave node; and a mesh node located at the wing-box skin just above the tyre that acts as master node, as shown in Figure 3.25.

The free rotation of the chiral node is allowed by not constraining the rotational displacement θ around the z direction in the coupling constraint definition. Finally, the last type of connection allowed the displacement of the lattice node parallel to the wing-box skin. For this case, the translational displacement u along the x direction is be left uncoupled.

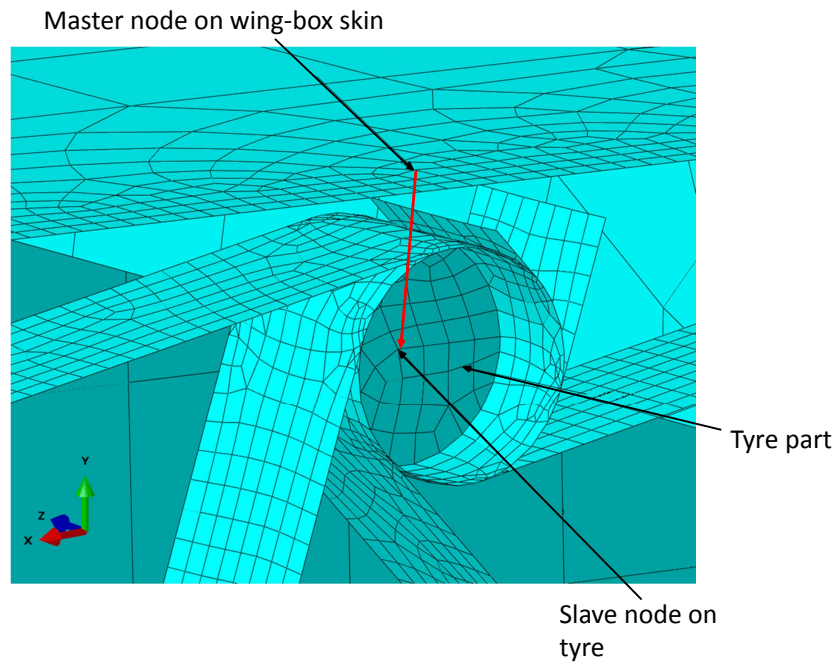


Figure 3.25: Coupling condition between the lattice node and the wing-box skin through tyre. The coupling condition is establish between a mesh node located in the wing-box skin that acts as a master node and a mesh node in the middle of the tyre that becomes the coupling or slave node.

3.3.7 Post-processing operations

The results obtained from the Abaqus simulations were analysed in two different ways. Firstly, qualitatively by means of the deformation plots that shown the corresponding Abaqus visualization module. And, secondly, extracting values of different magnitudes directly from the mesh nodes or elements located at certain positions of interest on the solution model.

As part of the execution of the parametric analysis program written using Python scripting, an additional module is used to perform the post-processing operations. The obtained values of the selected variables are written to an external files.

The calculation of the wing-box twist is done through the evaluation of the rotational displacement u around the x direction at a number of mesh elements located in different parts of the tip rib, as shown in Figure 3.26.

Due to deformations occurring at the tip rib, the value of u extracted from each of the mesh nodes is going to differ. A magnitude of this discrepancy between the mean value and the single values of u is shown through the evaluation of the deviation from the mean. The calculated mean value and the maximum deviation are included in the tables that contain results from the simulations.

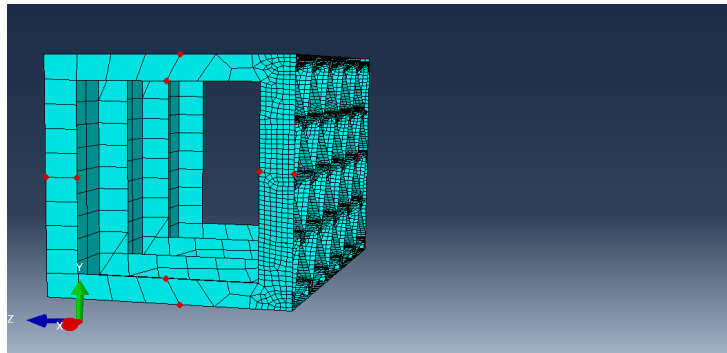


Figure 3.26: Location of the mesh nodes from which valued of the rotational displacement u is extracted. The final value for the twist is calculated from the mean value of u at the mesh nodes shown.

3.3.8 Parametric study method

The model described in the previous subsections is implemented in a Python program that is read by the FEM software, Abaqus CAE. The program is fully parametrized, enabling the possibility of executing simulations for different values of the parameters introduced previously. This procedure consists on a parametric study procedure that is initiated when executing the python file `mainAbaqusParametricStudy.py`. This piece of code reads the parameters that belong to the parametric study by executing the file `setUpParametricStudy`. As part of the parametric study process, a computational model is built in Abaqus, submitted for analysis using Abaqus Standard and post-processed by the complementary program `mainBuildAndExecuteWingBox.py`.

The convergence of the simulation is controlled within the program `mainAbaqusParametricStudy.py` and it is able to re-run a simulation with slight variations in the mesh size and/or in artificial dissipation definition if convergence was not achieved.

An schematic characterization of the program execution is shown the flow chart represented in Figure 3.27. The code written for this program can be found in Appendix A.

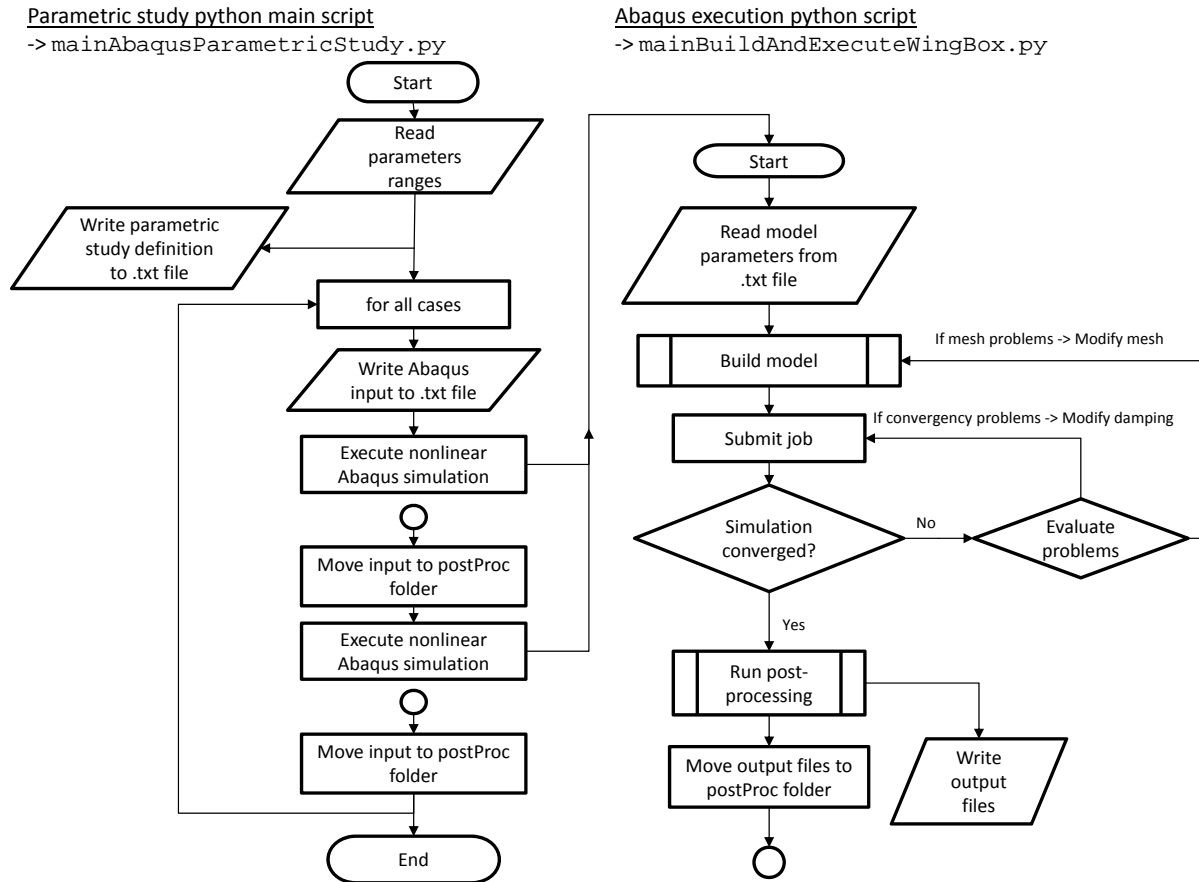


Figure 3.27: Flow chart showing the execution of the parametric study python code. The execution of the parametric study is controlled within the program `mainAbaqusParametricStudy.py`, responsible of the execution the program `mainBuildAndExecuteWingBox.py` that builds the model, submits the job for analysis and performs the post-processing operations on the solution model, for each of the cases considered in the parametric study definition.

Chapter 4

Model analysis

In the present chapter the general characterization of the model is presented. The first section includes an analysis of the analytical model. For this, a variation of the beam geometric parameters and the stiffness ratio E_1/E_2 is performed, and the consequent effect on the mechanical properties and the bending-twist coupling of the beam is evaluated. This analysis provides fast insight of how the different design parameters affect the final mechanical properties of the beam.

In the second section, the computational model is analysed in order to obtain the most suitable configuration that allows the validation of the proposed technology. In particular, discussions over the methods to model the rigid body behavior of the lattice nodes, the load introduction method, the mesh particularities, the ribs inclusion and the nonlinearities the response are presented.

4.1 Analytical model analysis

The analytical model of the wing-box was already presented in the Section 3.2. For the results that are presented in the subsections below, the model parameters take the nominal values presented in Table 4.1. These are taken from a similar analytical approach to the problem of a wing-box with a variable-stiffness web, presented in [17]. By doing this, verification of the results becomes possible.

Parameter	Symbol	Units	Nominal value
Dimensions			
Height of the cross section	H	mm	200
Wing-box length	L	mm	800
Width of the cross section	B	mm	80
Wing-box wall thickness	t_1, t_2	mm	1
Material (Aluminum)			
Young's modulus	E_1, E_2	N/mm ²	69000
Shear modulus	G_1, G_2	N/mm ²	26000

Table 4.1: Nominal value of the parameters used for the analytical model. The mechanical properties of the material used correspond to standard aluminum.

4.1.1 Bending and twisting coupling results and discussion

Here, the influence of the stiffness ratio E_1/E_2 on the coupling between the bending and the twist deformations of the beam is presented. This is graphically shown in Figure 4.1 for a number of simulations performed for a load Q_z equal to 2000 N. In the plot, the twist deformation at the tip is shown with the solid line and it is represented using the variable ϕ_{tip}/Q while the bend deformation is shown with the dashed line and it is also represented as w_{tip}/Q .

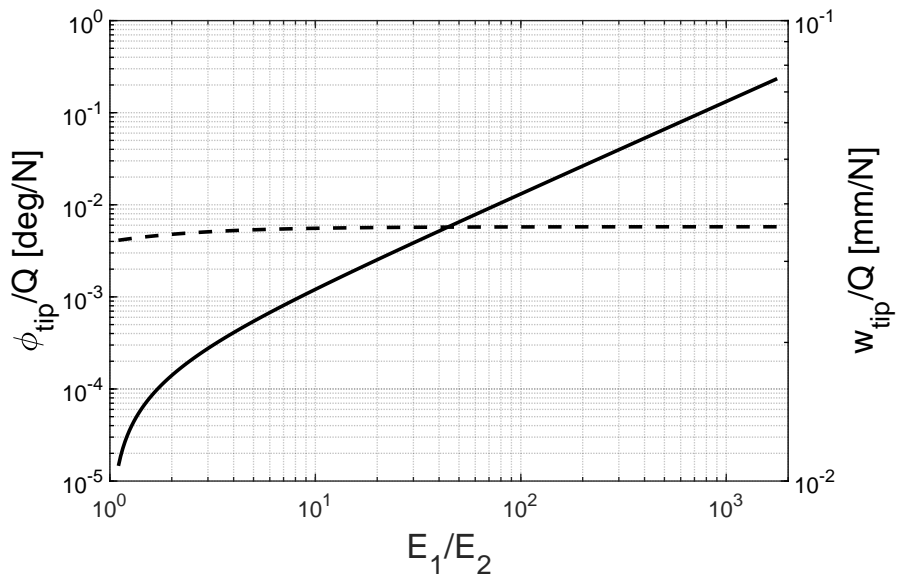


Figure 4.1: Influence of the stiffness ratio E_1/E_2 on the wing-box tip twist ϕ_{tip} and bend w_{tip} . The solid line is used to represent the twist ϕ_{tip} while the dashed line represents the bend w_{tip} . The two displacements correspond to values seen in the wing-box tip and are divided by the applied force magnitude Q_z .

In Figure 4.1, the stiffness ratio E_1/E_2 is modified over a wide range such that $E_1/E_2 \in [10^0, 10^3]$. It can be seen that the variable ϕ_{tip}/Q_z is consequently increased by various orders of magnitude from $\phi_{\text{tip}}/Q_z = 10^{-4}$ deg/N to $\phi_{\text{tip}}/Q_z = 10^{-1}$ deg/N, as a consequence of the stiffness ratio variation. However, the variation in bend represented with the variable w_{tip}/Q_z is negligible in comparison. It can be seen that the bending displacement quickly increases for values of $E_1/E_2 > 1$ and it gets to an asymptote for values $E_1/E_2 \gg 1$. These results therefore show how the twist displacement, which gives information regarding the torsional stiffness of the structure, is much more affected by variations of the stiffness ratio E_1/E_2 than the bending stiffness is. Consequently, it is not expected to see large increments in bend displacement in comparison with twist displacement when the variable-stiffness mechanism is activated. This results are in compliance with those presented in [17].

For the proposed mechanism, it is expected that the ratio E_1/E_2 , which is linked to the effective

shear modulus G_{eff} of the real wing-box, is reduced in various orders of magnitude once the buckling phenomena is triggered. After this event, the results above show that the reduction in bending stiffness of the wing-box will be negligible in comparison with the reduction in torsional stiffness.

4.1.2 Parametric study results and discussion

In the present subsection, the variation of the beam mechanical properties for different geometric parameter values is shown. The beam geometry is characterized through the cross-sectional aspect ratio B/H , the thickness ratio t_2/t_1 and the slenderness ratio L/B . The effect of these parameters on the sectional properties, twist and bending stiffness, and flexural and twisting compliance are shown. Additionally, the variance of the stiffness ratio E_1/E_2 is also included in the analysis.

The influence of the cross-sectional aspect ratio B/H on the torsional stiffness GI_t , the shear centre position y_{SC} and the flexural stiffness EI_y is shown in Figures 4.2, 4.3 and 4.4, respectively. On its side, the effect of thickness ratio t_2/t_1 on the same three beam parameters is shown in Figures 4.5, 4.6 and 4.7.

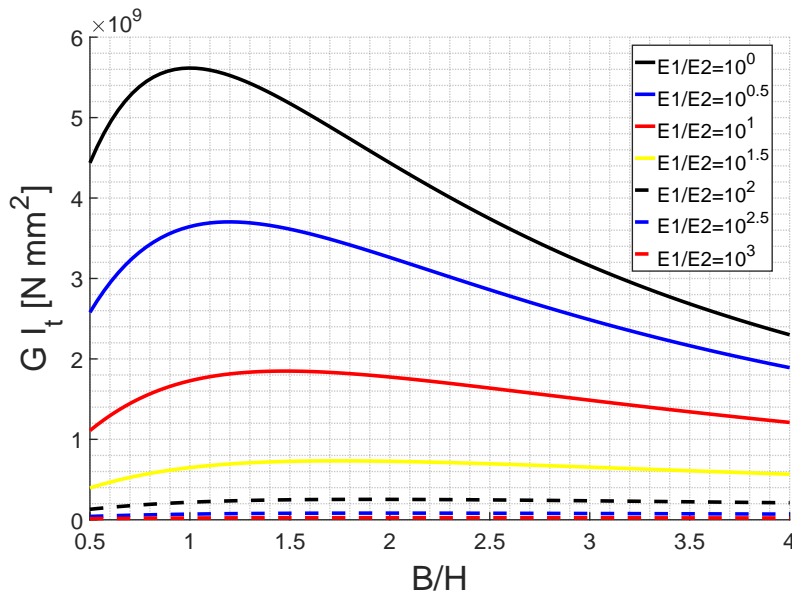


Figure 4.2: Influence of the cross-sectional aspect ratio B/H on the torsional stiffness GI_t , shown for various values of the stiffness ratio E_1/E_2 ranging from 10^0 to 10^3 .

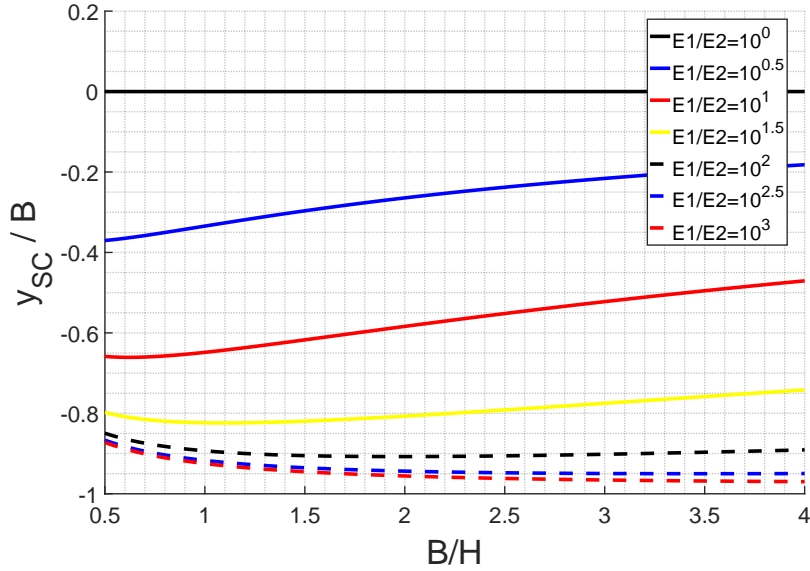


Figure 4.3: Influence of the cross-sectional aspect ratio B/H on the dimensionless shear centre position y_{SC}/B , shown for various values of the stiffness ratio E_1/E_2 ranging from 10^0 to 10^3 .

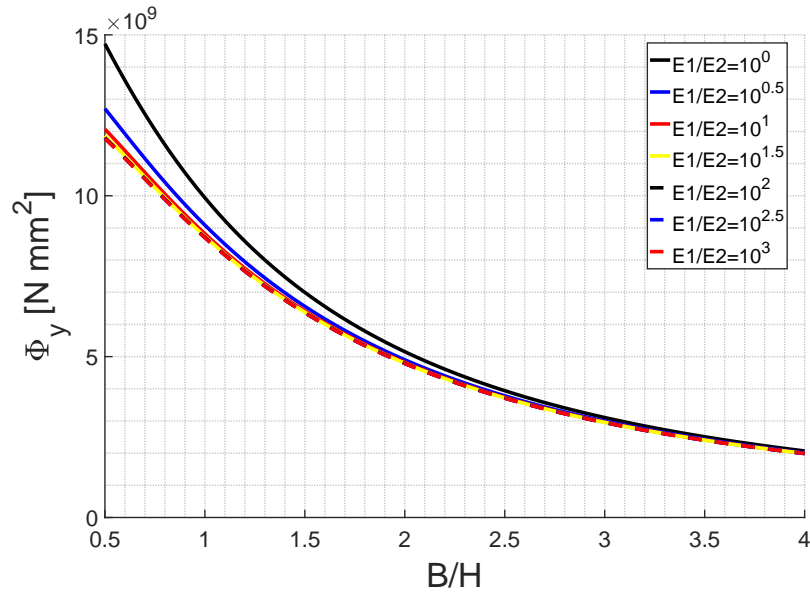


Figure 4.4: Influence of the cross-sectional aspect ratio B/H on the flexural stiffness $EI_y = \Phi_y$, shown for various values of the stiffness ratio E_1/E_2 ranging from 10^0 to 10^3 .

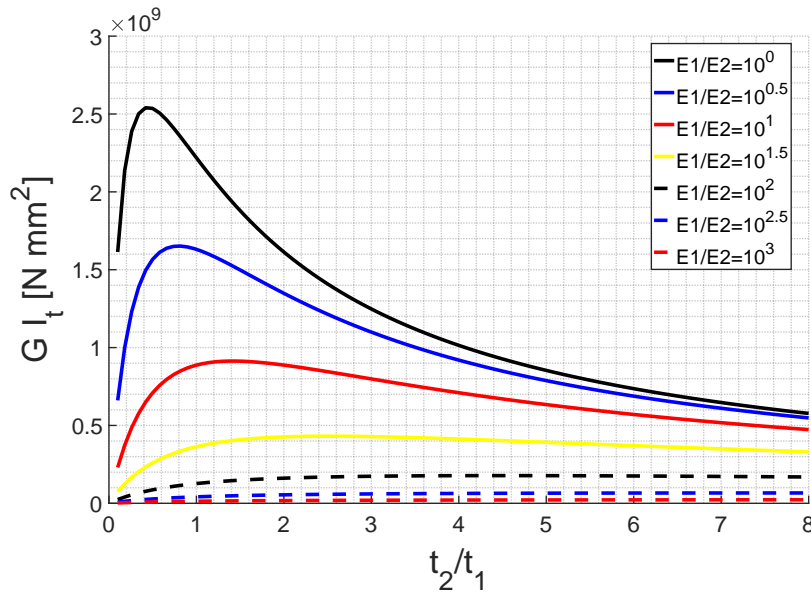


Figure 4.5: Influence of the wall thickness ratio t_2/t_1 on the torsional stiffness GI_t , shown for various values of the stiffness ratio E_1/E_2 ranging from 10^0 to 10^3 .

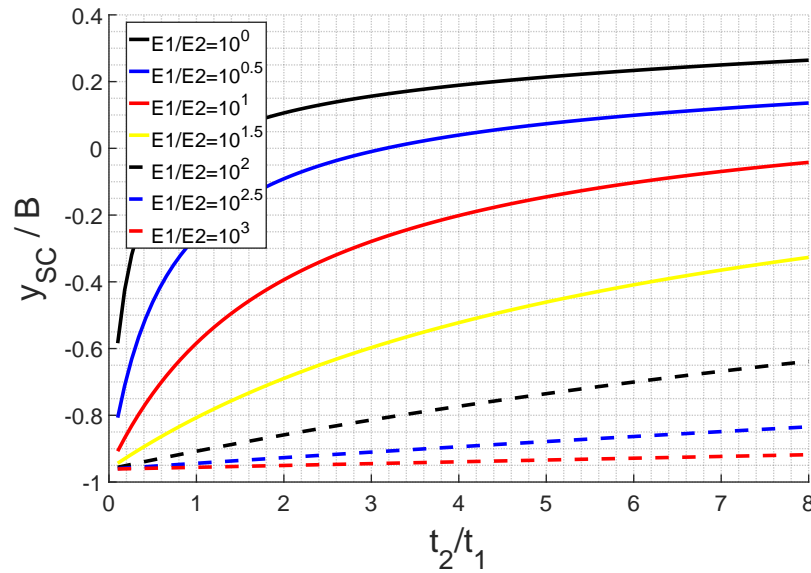


Figure 4.6: Influence of the wall thickness ratio t_2/t_1 on the dimensionless shear centre position y_{SC}/B , shown for various values of the stiffness ratio E_1/E_2 ranging from 10^0 to 10^3 .

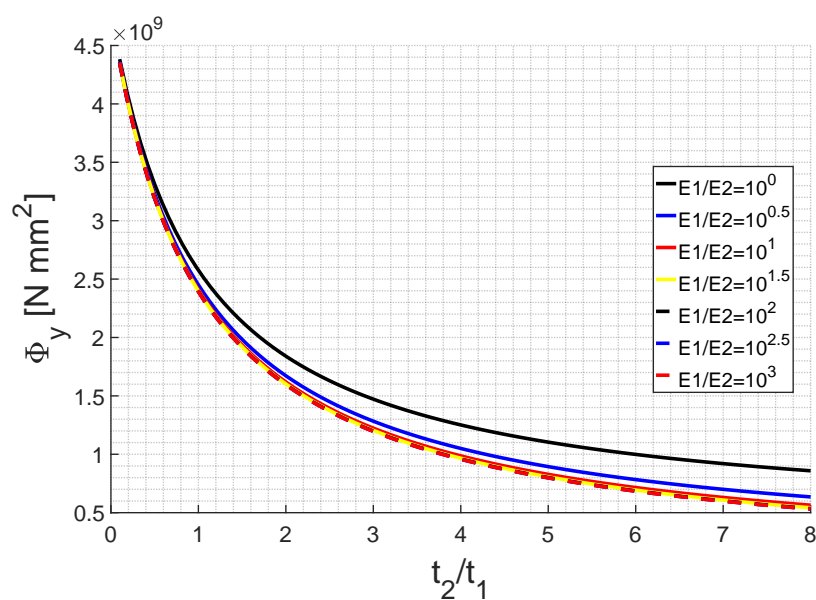


Figure 4.7: Influence of the wall thickness ratio t_2/t_1 on the flexural stiffness $EI_y = \Phi_y$, shown for various values of the stiffness ratio E_1/E_2 ranging from 10^0 to 10^3 .

In Figure 4.2, it can be seen that a maximum torsional stiffness appears for $B/H = 1$ when $E_1/E_2 = 1$. This can be explained because, as it is also shown in [17], the closer the torsional stiffness to the doubly symmetric case, the higher its torsional stiffness. However, when $E_1/E_2 > 10$, the maximum torsional stiffness is shown to appear for $B/H > 1$. A similar conclusion can be extract when analyzing the Figure 4.5, that shows the influence of the thickness ratio t_2/t_1 on the torsional stiffness GI_t .

In Figure 4.3 shows that for values $E_2 \ll E_1$, the shear centre position y_{SC} is approximately constant for B/H variations. In this context, the beam approximates its behavior as if it has an open profile section. However, as the value of E_1/E_2 decreases, the influence of the ratio B/H increases showing a bigger influence of the web where the Young's modulus E_2 applies. On the other hand, Figure 4.6 shows that the bigger the thickness ratio t_2/t_1 is, the closer that the shear centre y_{SC} will be to the vertical axis of symmetry. However, for $E_2 \ll E_1$ the influence of the thickness ratio t_2/t_1 is reduced.

In Figure 4.4 it can be seen that the flexural stiffness EI_y decreases when the cross-sectional aspect ratio B/H increases. This is explained because the second moment of area I_y is reduced when B/H increases as the coordinate y of the points in the section is reduced as well. Similarly, it can be seen in Figure 4.7 that when the thickness ratio t_2/t_1 increases, the value of EI_y decreases. In both cases, the flexural stiffness EI_y is little affected by variations of the stiffness ratio E_1/E_2 . This result matches what was already shown in Subsection 4.1.1.

Additionally, the effect of the cross-sectional aspect ratio B/H on the deflection and torsional compliances is shown in Figures 4.8 and 4.9, respectively. The corresponding plots when analyzing the effect of the thickness ratio t_2/t_1 on the deflection and torsional compliance are shown on Figures 4.10 and 4.11, respectively. The beam torsional compliance is expressed as a fraction of the twist at the tip divided by the vertical force applied, that is $|\phi_{tip}|/Q$, while the beam flexural compliance is expressed as fraction of the maximum vertical displacement at the tip divided by the vertical force applied, that is $w_{0,tip}/Q$.

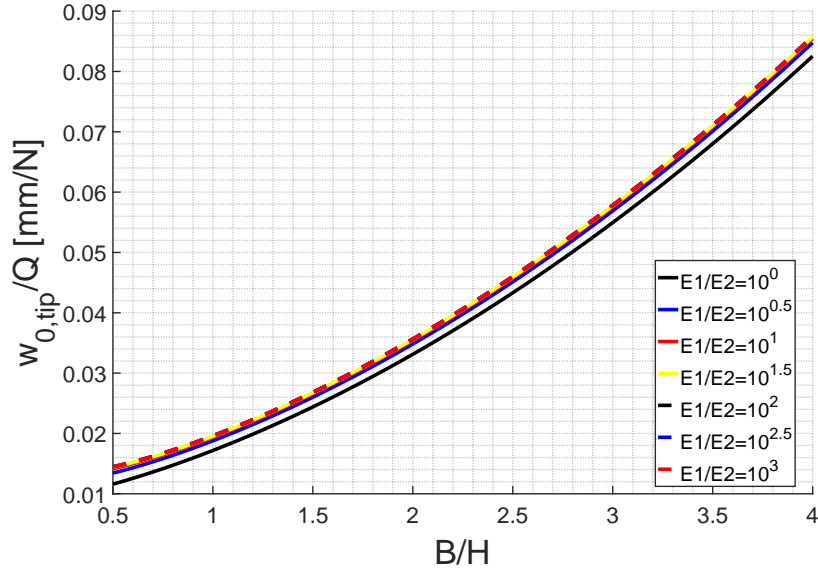


Figure 4.8: Influence of the cross-sectional aspect ratio B/H on the flexural compliance $w_{0,\text{tip}}/Q$, shown for various values of the stiffness ratio E_1/E_2 ranging from 10^0 to 10^3 .

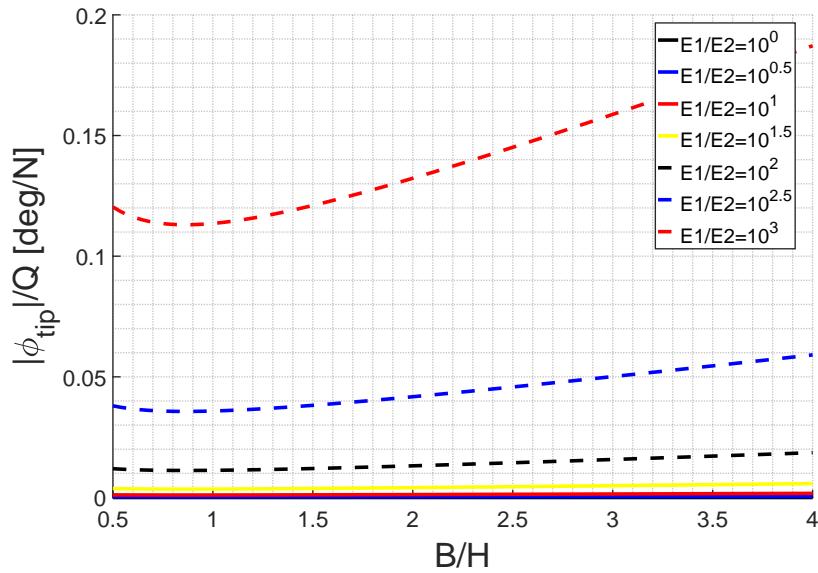


Figure 4.9: Influence of the cross-sectional aspect ratio B/H on the torsional compliance $|\phi_{\text{tip}}|/Q$, shown for various values of the stiffness ratio E_1/E_2 ranging from 10^0 to 10^3 .

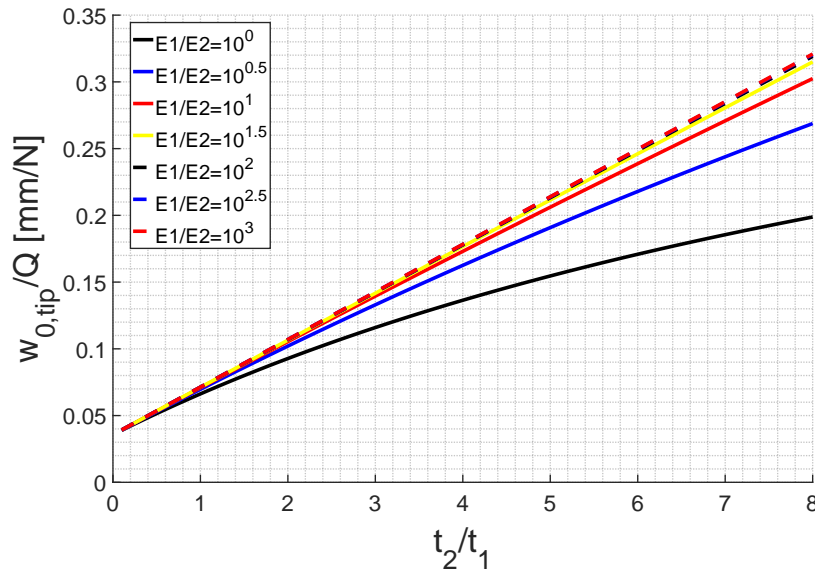


Figure 4.10: Influence of the thickness ratio t_2/t_1 on the flexural compliance $w_{0,\text{tip}}/Q$, shown for various values of the stiffness ratio E_1/E_2 ranging from 10^0 to 10^3 .

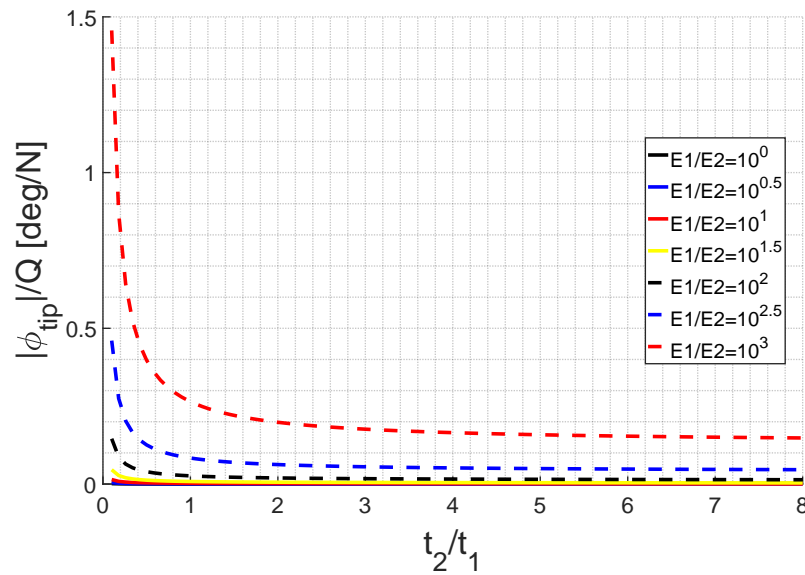


Figure 4.11: Influence of the thickness ratio t_2/t_1 on the torsional compliance $|\phi_{\text{tip}}|/Q$, shown for various values of the stiffness ratio E_1/E_2 ranging from 10^0 to 10^3 .

From the analysis of the torsional compliance $|\phi_{\text{tip}}|/Q$ as a function of the thickness ratio t_2/t_1 in Figure 4.10, it can be seen that increments in t_2/t_1 amplifies the effects of variations of the stiffness ratio E_1/E_2 on the flexural compliance $w_{0,\text{tip}}/Q$. On the other hand, Figure 4.8 shows that the flexural compliance $w_{0,\text{tip}}/Q$ increases when the cross-sectional aspect ratio B/H increases and the value of B/H does not alter the magnitude of the effect of variations of E_1/E_2 in the flexural compliance, effect that remains small.

From Figure 4.11, it can be understood that there is not variation in the torsional compliance for values of the thickness ratio $t_2/t_1 > 1$; but for $t_2/t_1 < 1$, the torsional compliance increases considerably. This result shows again something similar at what it was shown in Subsection 4.1.1, how the modification of shear stiffness in the second web has a considerable effect on the torsional stiffness. On the other hand, Figure 4.9 shows small effect of the variation of the cross-sectional aspect ratio B/H on the torsional compliance.

The effect of the slenderness ratio L/B on the deflection and torsional compliances is shown in Figures 4.12 and 4.13, respectively. These two figures show how the flexural and torsional compliance increase for increasing values of L/B . Also, Figure 4.12 shows again the small influence of the stiffness ratio E_1/E_2 in the flexural compliance while Figure 4.13 shows how the torsional compliance is considerably affected by variations of E_1/E_2 .

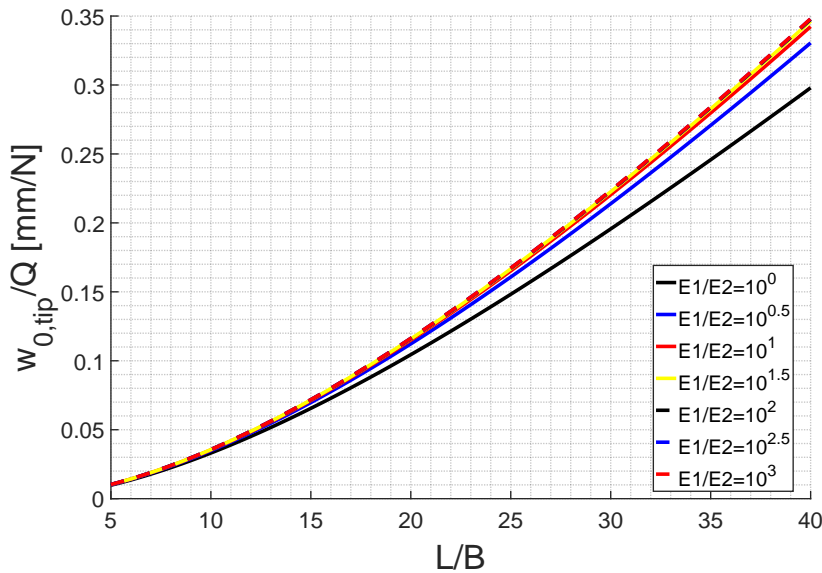


Figure 4.12: Influence of the slenderness ratio L/B on the flexural compliance $w_{0,\text{tip}}/Q$, shown for various values of the stiffness ratio E_1/E_2 ranging from 10^0 to 10^3 .

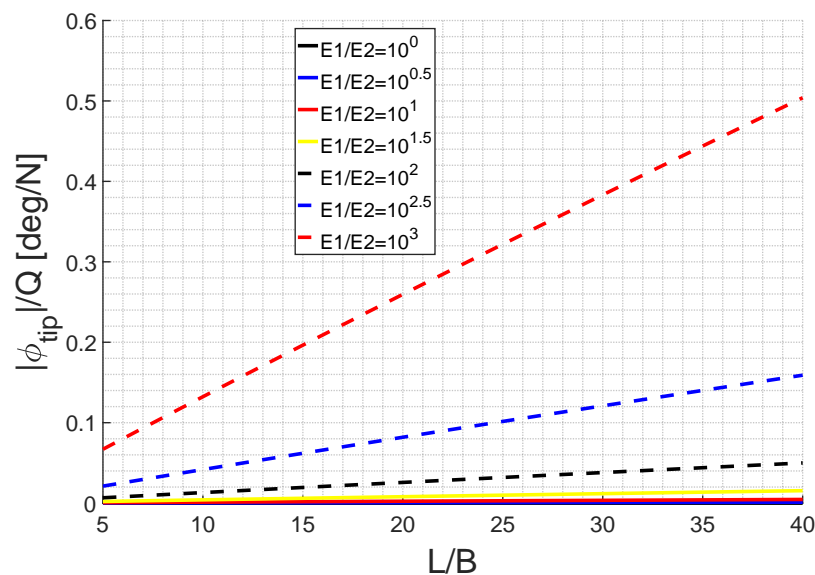


Figure 4.13: Influence of the slenderness ratio L/B on the torsional compliance $|\phi_{\text{tip}}|/Q$, shown for various values of the stiffness ratio E_1/E_2 ranging from 10^0 to 10^3 .

4.2 Computational model analysis

In the present section, results from the analysis performed on the computational model are presented. Different aspects of the model are evaluated and design decisions are justified. The analysis considers the modeling of the lattice nodes rigid behavior, the different load introduction strategies, the influence of the mesh in the simulation convergence, the addition of the ribs and the nonlinearities that appear in the problem.

For the proposed technology, it is expected to see the appearance of large deformations and elastic instabilities in the structure. This means that the structural stiffness of the model is altered as the load applied increases. For this reason, it becomes necessary to execute nonlinear simulations in which the load applied is increased by small step increments. Each of these steps constitutes a different frame that contains particular values of the problem magnitudes at the mesh nodes and elements.

Furthermore, linear simulations are also executed to provide information of the expected response of the structure considering its initial stiffness, before the onset of the elastic instabilities that alter the stiffness. The results obtained from the nonlinear simulations are compared to those obtained from the linear simulations. This comparison is done by means of the curve displacement-force that shows the achieved twist adaptation of the wing-box at each of the frames that build up the complete simulation window.

In addition to this general nonlinear/linear global response comparison, the performance of the structure is also analysed by means of the evaluation of the six possible displacements of the mesh nodes at different parts of the structure. The value of these magnitudes are shown in colour contours plots over the solution model.

4.2.1 Rigid body modeling

Two different approaches are followed to model the rigid body behavior of the lattice nodes, as it has been already explained in Subsection 3.3.5. The first modeling approach considers the creation of a coupling condition between a reference point positioned at the centre of the lattice node cylinder and mesh nodes located in the faces of the lattice node. The second approach consists on the introduction of an additional part that is placed in the middle of the cylinder to add stiffness to the element. In this section, the results obtained for each modeling approach are compared.

In Figure 4.14, the displacement-force curve for the nonlinear and linear responses in wing-box twist obtained for each modeling approach are compared. It can be seen that when the tyre approach is used, the collapse of the structure occurs at a smaller load than if the coupling implementation is used.

Also, the analysis of the mesh nodes displacements on the solution model shows that, when the tyre rigid body behavior is modeled using the tyre part, the rotation of the lattice nodes around its own axis is approximately 20% higher than when the modeling is done using the coupling constraint. This rotation should be free and be only constrained by the connection to the ligaments. Therefore, it is concluded

that the use of the tyre part is a more realistic approach to modeling the rigid body behavior of the lattice nodes.

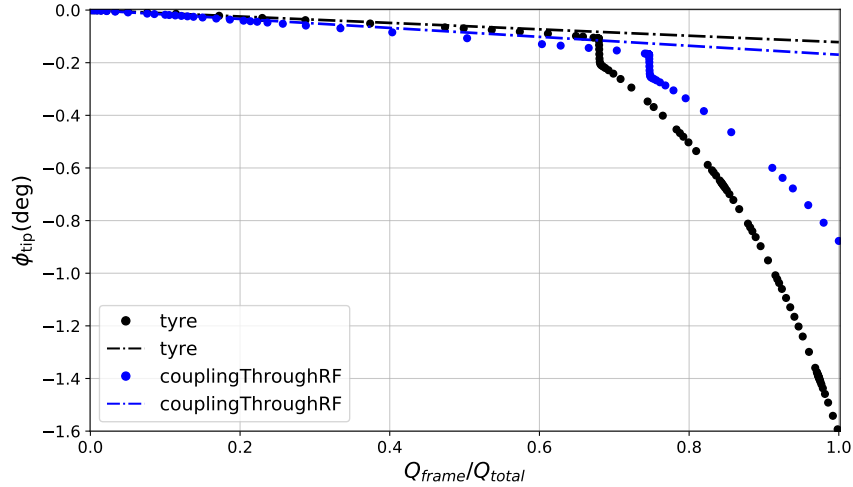


Figure 4.14: Displacement-force curve obtained using different approaches to model the rigid lattice node.

4.2.2 Load introduction method

As shown in Subsection 3.3.3, there are multiple ways in which the load can be introduced into the structure. It was decided to locate the load introduction points at the upper flange of the ribs in an attempt of replicate how the load will be introduced in a future manufactured demonstrator. In this subsection, the different results obtained when modifying the load introduction method are shown.

Firstly, the option of distributing the same total load over the total number of ribs, three in the baseline configuration, is compared with the option of concentrating all the load on the upper flange of the tip rib. In Figure 4.15, the curve displacement-force is shown for these two different cases. It can be seen how when the load is distributed over a number of points and it is not concentrated on a single point, a delay in the onset of the structure collapse occurs. This result is correlated with visual inspection of the displacement of the mesh nodes on the solution model in Abaqus. The corresponding colour contour of the rotational total displacement $\sqrt{\theta^2 + \phi^2 + \psi^2}$ for a distributed load is shown in Figure 4.16. Here it can be seen how buckling has started to occur on the ligaments located close to the ribs, where the load is being introduced. In a further stage, when load increases, buckling would start to occur at the root of the wing-box.

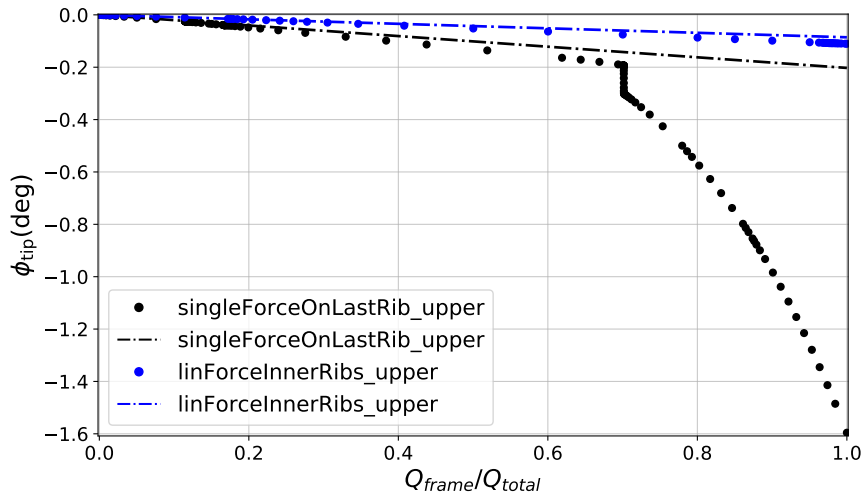


Figure 4.15: Displacement-force curve showing the model response using different load introduction methods. The label “singleForceOnLastRib_upper” corresponds to the case of using one single point for the load introduction. This point is located at the upper flange of the tip rib. The label “linForceInnerRibs_upper” corresponds to the case of introducing load on the upper flange of all the available ribs, which are three for the baseline configuration, two in the inner part of the wing-box and one at the tip. It can be see that the concentration of the load advances the onset of the structure collapse.

Secondly, in Figure 4.17 a comparison of the response for different load position points in the chordwise direction is shown. The plot shows the displacement-force curve for four values of the variable z/W_{box} . A smaller value of z/W_{box} represents a load introduction point located closer to the chiral lattice.

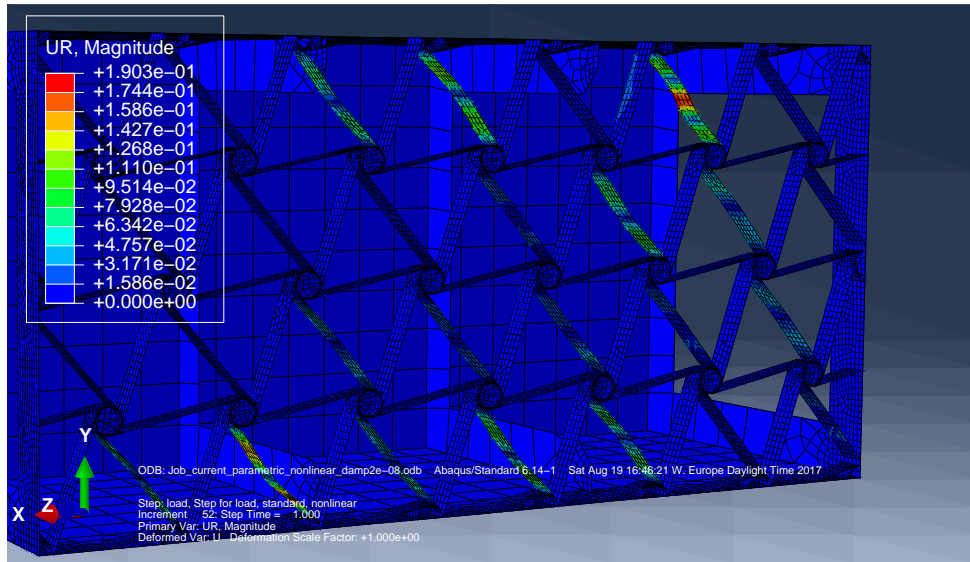


Figure 4.16: Deformed state of the model for a distributed load introduction method. It can be seen how since the buckling is starting to occur at the ligaments located close to the ribs, the onset of the elastic instabilities is delayed.

It can be seen that buckling is not triggered for values of z/W_{box} equal to 0.6 and 0.8. This is explained because the further the introduction point is from the chiral lattice, the less shear strain appears on the chiral lattice and the later that the onset of the elastic instabilities occurs.

Since the distribution of the load in more than one rib only delays the onset of the instabilities, it is decided to use a single load introduction point for the study performed on the baseline configuration, in an attempt to simplify the model. Also, it is decided to locate the load introduction point at $z/W_{\text{box}} = 0.5$ to keep the symmetry.

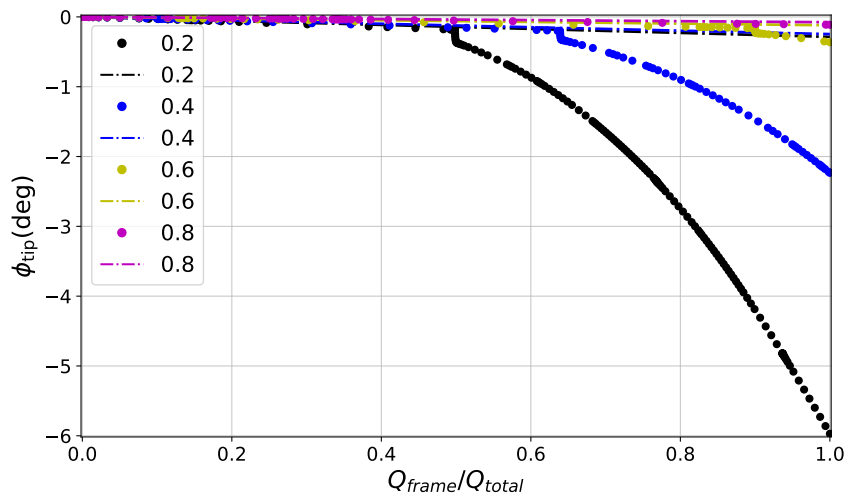


Figure 4.17: Displacement-force curve showing the model response for different load introduction points z/W_{box} . A smaller value of z/W_{box} represents a load introduction point located closer to the chiral lattice. The further the introduction point is from the chiral lattice, the less shear strain appears at the chiral lattice and the later that the onset of the elastic instabilities occurs.

4.2.3 Connection between the wing-box skin and the chiral lattice

As it has been already explained in Subsection 3.3.6, the modeling of the connection between the chiral lattice structure and the wing-box skin is one of the critical aspects of the design. In the basic connection type, the lattice node is cut by half and it is directly attached to the wing-box skin, restraining all the possible degrees of freedom. In a further step, the lattice node is allowed to rotate around its own axis. For this type of connection, the rotational displacement θ of the mesh node in the centre of the tyre embedded into the lattice node is left uncoupled when defining the coupling constraint with the mesh nodes on the wing-box skin. Additionally, it is also possible to allow the lattice node to translate parallel to the wing-box skin, leaving the degree of freedom u unrestrained.

In Figure 4.18, the displacement-force curves obtained for the three types of connection are shown. It can be seen how allowing the free rotational displacement θ of the nodes leads to an earlier onset of the instabilities that causes the structure collapse. Additionally, it can be seen that when the displacement u is left unrestrained, the mechanism activation occurs even before. To sum up, the allowance of additional degrees of freedom of the lattice nodes lead to the advance of the buckling-induced mechanism activation.

Finally, the total rotational displacement of the mesh elements is shown in a colour contour plot on the solution model in Figure 4.19, where it can be seen how a different buckling field appears for each of the modeling approaches.

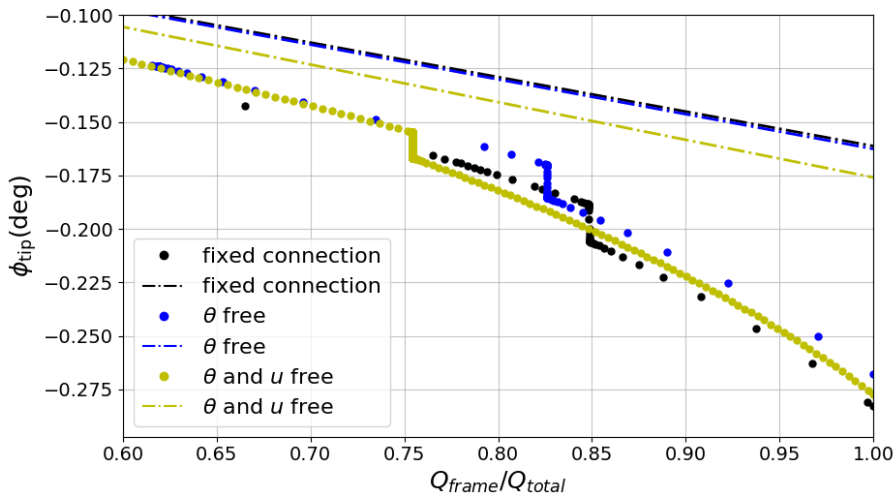


Figure 4.18: Displacement-force curve showing the model response for different approaches to model the connection between the chiral node and the wing-box skin. It can be seen that the allowance of additional degrees of freedom of the lattice nodes lead to the advance of the structure collapse and the onset of the instabilities.

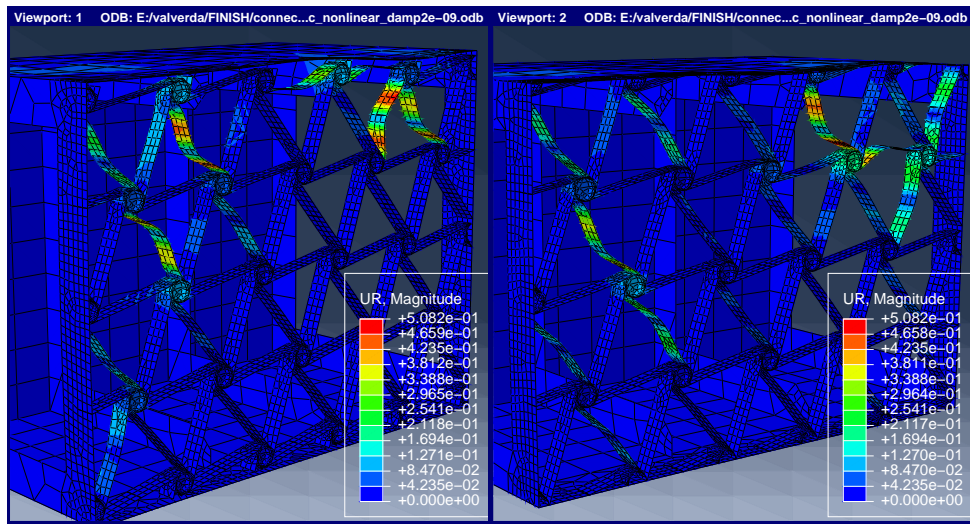


Figure 4.19: Color contour representation of the total angular displacement of the mesh elements on the deformed structure for different approaches to model the connection between the chiral node and the wing-box skin. The figure on the right shows the buckling field when the connection is such that the lattice nodes are restrained in all its degrees of freedom, and the one in the left shows the buckling field when the rotation of the lattice nodes is allowed. It can be seen how different connection approaches lead to different buckling fields.

4.2.4 Mesh

The model is build using cell shell elements as the fundamental constituting part. The thickness is assigned in the perpendicular direction, as it is shown in Figure 3.5.

This type of element is a 2D element that it was used to build 3D structures. This kind of procedure may incur in distortions in the mesh elements due to shell elements intersecting in the same line at different angles. For the designed model, this situation occurred at certain locations of the chiral lattice structure. It can be seen in Figure 4.20 that the distorted elements appear at two different locations. Firstly, at the plane where the two ligaments with different curvature join. At this point, the sharp angles that appear in between the geometrical lines induce the appearance of tetrahedral distorted mesh elements. The second typical location for appearance of distorted elements is along the curve where the lattice nodes and the curved ligaments join.

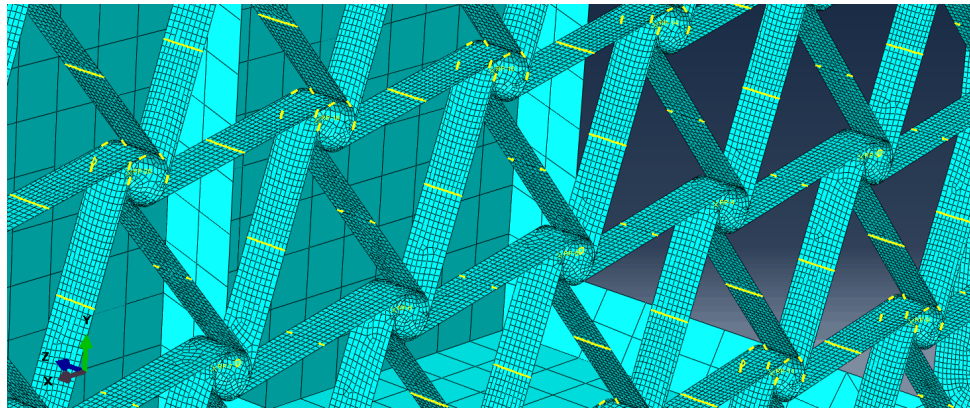


Figure 4.20: Distorted mesh elements in the model. The number of distorted elements was found to be crucial for the simulation convergence.

It was seen that the number of distorted elements had a significant effect in the simulation convergence evolution. For a high number of distorted elements, the simulation could not go further from the first step. No attempts to locally modify the mesh at the mentioned locations were made, instead, it was found that modifying the global mesh size gave enough control over the number of distorted elements to be able to overcome this limitation. The bigger the mesh size in the area, the less distorted elements appear after completing the meshing operations.

4.2.5 Nonlinear problem and automatic stabilization

For the case under study, nonlinear simulations are carried out as is expected to find large displacement and non-constant stiffness. In Abaqus, to execute nonlinear simulation involves the following considerations, as shown in [39]:

- a combination of incremental and iterative procedures;
- using the Newton method to solve the nonlinear equations;
- determining convergence;
- defining loads as a function of time; and
- choosing suitable time increments automatically.

Therefore, Abaqus breaks the step where the load is applied into increments. The software automatically chooses the size of each of the increments based on the convergence evolution of previous increments.

Also, nonlinear static problems may become unstable. One of the possible sources of such instabilities is buckling. A model where buckling appears locally may not be resolvable using general solution methods. For this kind of cases, it becomes necessary to either solve the problem dynamically or with the aid of artificial damping.

Since the above situation represents what it is expected to be found in the model response, a constant artificial damping factor is used throughout the whole step to account for the appearance of local instabilities.

Automatic stabilization with a constant damping factor implies that viscous forces of the form:

$$F_v = c\mathbf{M}\mathbf{v} \quad (4.1)$$

are added to the global equilibrium equations:

$$\mathbf{P} - \mathbf{I} - \mathbf{F}_v = 0, \quad (4.2)$$

where \mathbf{I} represents the internal forces, \mathbf{P} the external forces, \mathbf{M} is the artificial mass matrix calculated with unity density, c is the defined damping factor, $\mathbf{v} = \Delta\mathbf{u}/\Delta t$ is the vector of nodal velocities, and Δt is the increment of simulation time.

The final value of c that is going to be used during the simulations is chosen after performing a small parametric study of the different possibilities. As a result, the plot shown in Figure 4.21 is produced. This plot represents the evolution of the twist at the tip as the load is increased step by step during the nonlinear simulation. As it will be explained in Section 5.1, the use of automatic stabilization becomes necessary to capture the nonlinear mechanics that involve buckling on the chiral ligaments and the ultimate collapse

of the structure. Finally, special care needs to be taken in order to ensure that the inclusion of artificial damping factor is not leading to inaccurate results due to over-damping of the structure. This can be done by comparing the fraction of the static energy that it is dissipated compared with the external work that is introduced into the system. Such a comparison is presented in the discussion below.

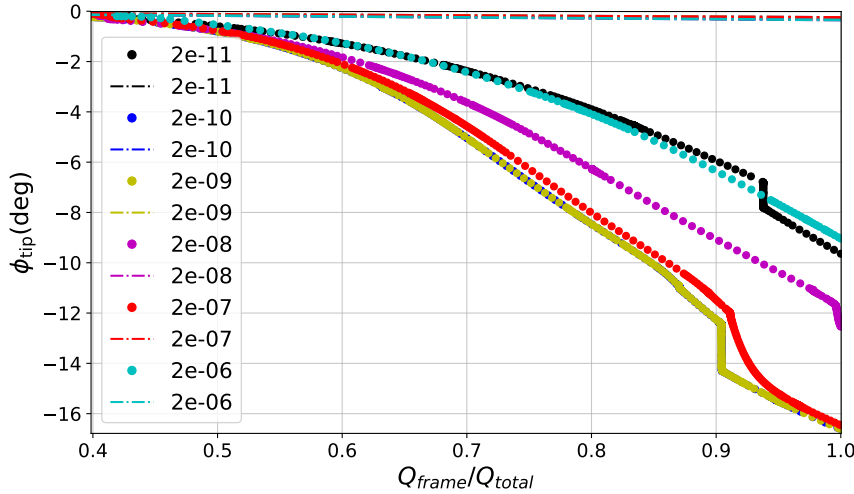


Figure 4.21: Displacement-force curve for various values of constant artificial damping factor.

As it can be seen in Figure 4.21, all the different values of the damping factors considered succeed to capture the wing-box tip twist adaptation. However, the responses differ considerably and no clear trend is shown. For low values of c , the structure fails to properly capture the onset of the buckling phenomena while, for high values of c , the structure over-damping leads to inaccurate results. To check if over-damping of the structure is occurring, a comparison between the static dissipated energy and the external work is shown for values of $c = 2 \times 10^{-5}$, $c = 2 \times 10^{-8}$ and $c = 2 \times 10^{-9}$ in Figures 4.22, 4.23 and 4.24, respectively. In these plots, the moment where the structure collapses due to the buckling phenomena occurring on the chiral ligaments can be seen as a sudden change in the slope of both energy curves. Here it can be seen that for the case of $c = 2 \times 10^{-5}$, the slope of the curve showing the energy dissipated through artificial stabilization is positive after the onset of buckling, which is a sign of over-damping in this region. On the other hand, for the case of $c = 2 \times 10^{-8}$, the slope remains zero. Finally, for the case of $c = 2 \times 10^{-9}$, the slope also remains zero and the final value for the energy dissipated is smaller than for $c = 2 \times 10^{-8}$. The displacement-force curve is coincident for the two cases of $c = 2 \times 10^{-8}$ and $c = 2 \times 10^{-9}$.

Finally, since the objective is to capture the dynamics that involve buckling on the chiral ligaments and the ultimate collapse of the structure, keeping the energy dissipated a small as possible fraction of the external work, it is decided to use constant damping factor $c = 2 \times 10^{-9}$ for the simulations performed ahead.

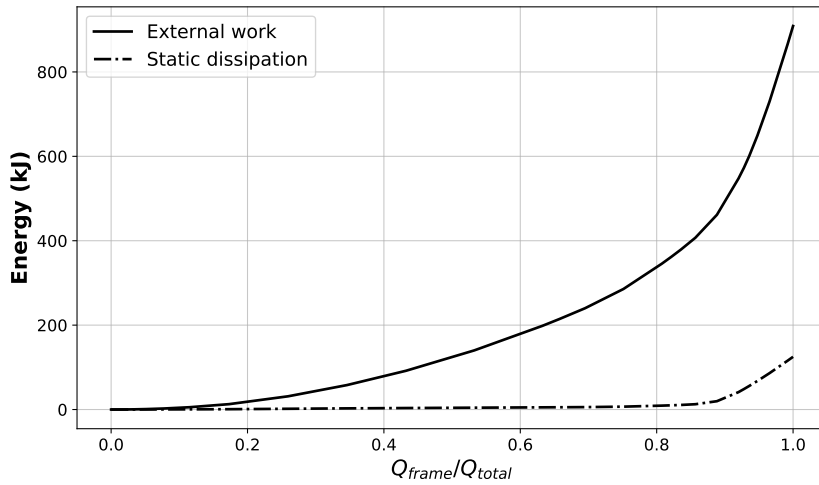


Figure 4.22: External work and static dissipation for a damping factor equal to 2×10^{-5} . The positive slope of the curve showing the energy used in the static dissipation is a sign of over-damping.

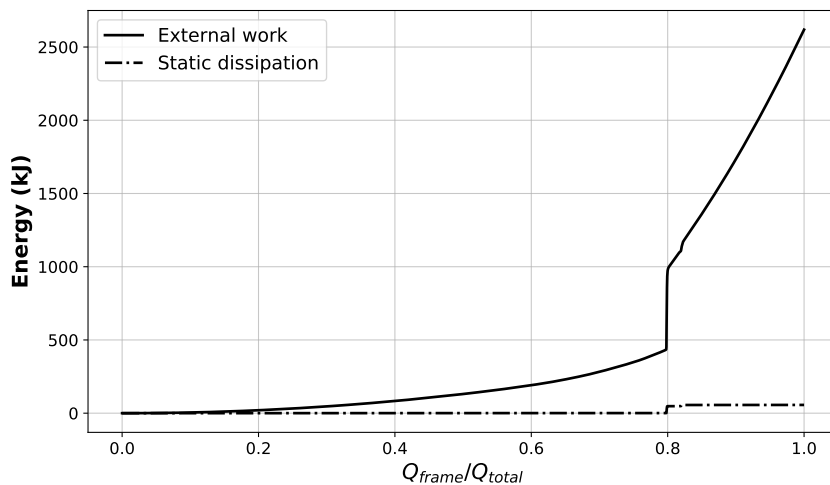


Figure 4.23: External work and static dissipation for a damping factor equal to 2×10^{-8} . After the structure collapse the static dissipation energy remains constant and small compared with the external work introduced into the system.

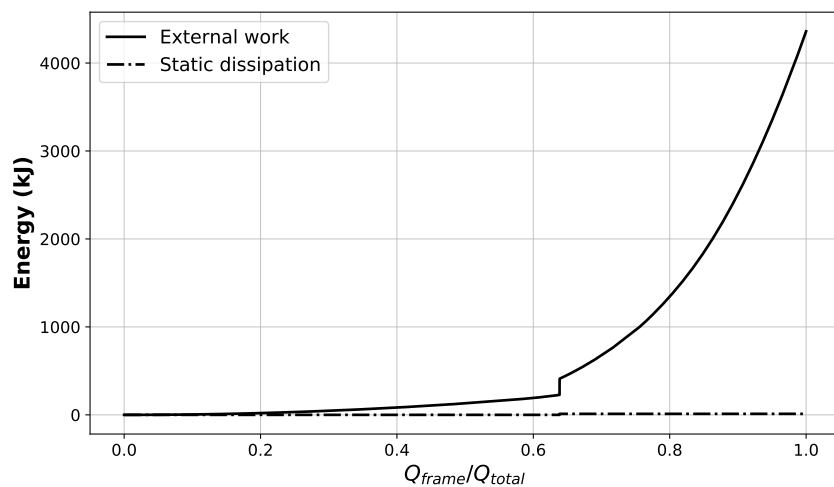


Figure 4.24: External work and static dissipation for a damping factor equal to 2×10^{-9} . After the structure collapse the static dissipation energy remains constant and negligible compared with the external work introduced into the system.

4.2.6 Ribs inclusion and control over the local deformation

As explained in Subsection 3.3.1, two different designs are developed for the rib, one consists in a open profile and the other one in a closed profile. A first set of simulations are executed for the option of one open section at the rib at the tip. In Figure 4.25, it can be seen an example of the response seen for this type of configuration after a prescribed load of 800 N has been applied. It can be seen that, under the prescribed load, the rib closes its profile and the upper flange shows a bigger displacement v compared with the lower flange.

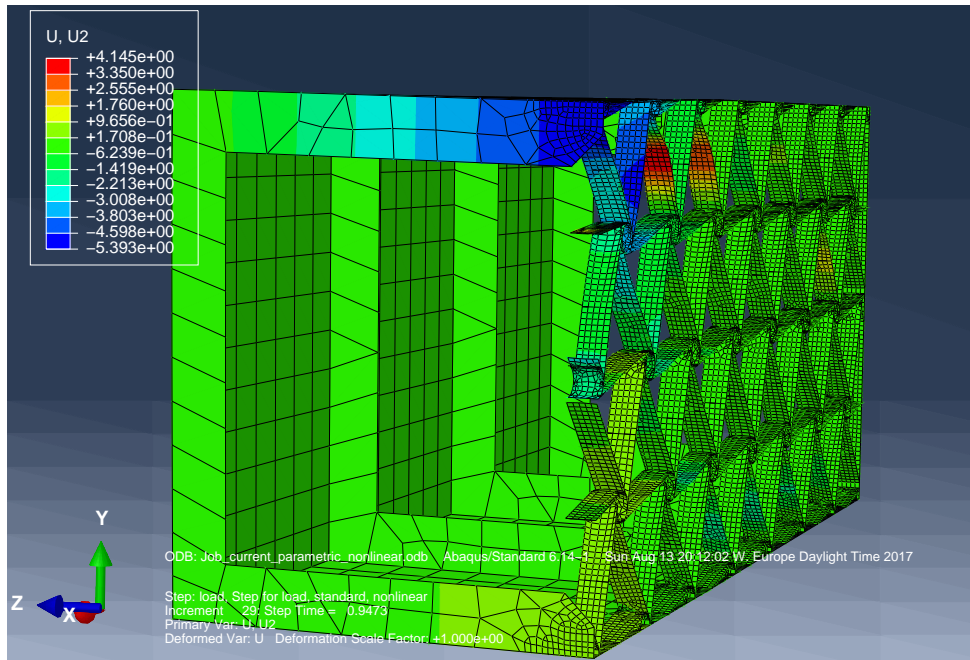


Figure 4.25: Vertical displacement v at the tip rib. The colour contour shows those mesh nodes located on the upper flange of the rib have a higher v , therefore showing how the rib is closing under the prescribed load (800 N)

In an attempt to avoid a deformation in the rib that causes the rib to close, it was decided to use ribs with a close profile. Simulation are initially executed without incorporating automatic stabilization. Then, the colour contour plot of the total rotational displacement over the solution model is shown in Figure 4.26, where it can be seen that the initial buckling occurs in ligaments located far from the root. The twist of the beam, measured as the rotational displacement u around the x direction, is approximately 0.3 deg. The prescribed load as -800 N and the simulation converged to the 95% of the prescribed load.

In order to investigate further stages of the simulation, the addition of automatic stabilization through artificial damping factor becomes necessary, as it was explained in Subsection 4.2.5. After doing so, the colour contour plot of the total rotational displacement over the solution model is shown in Figure 4.27. Apart from the buckling occurring at the chiral ligaments, this figure shows how big local deformations appear on the wing-box upper skin for this case. Also, it can be seen that the buckling phenomena has

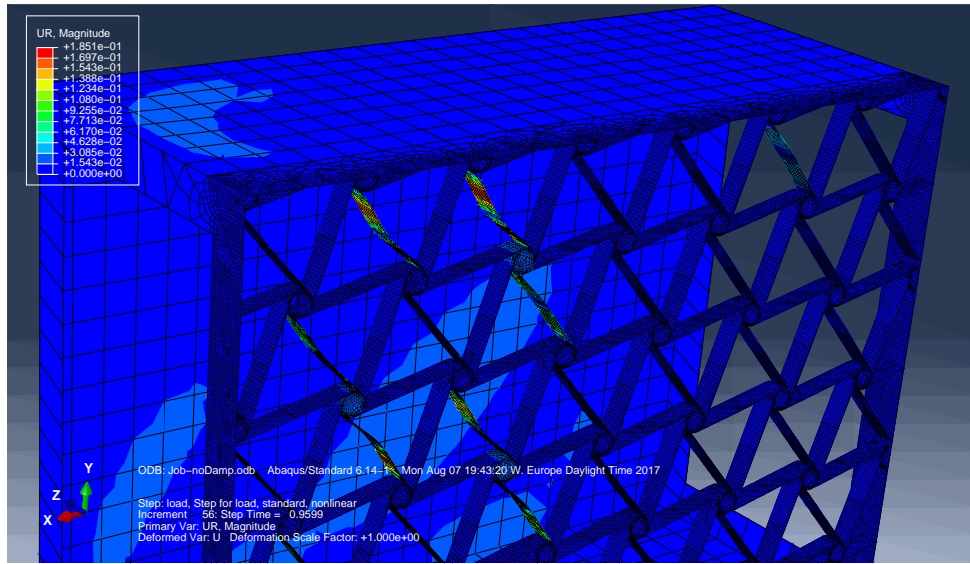


Figure 4.26: Model response without the use of inner ribs nor automatic stabilization. The simulation converged to the 95% of the prescribed load (800 N). Elastic deformations in the ligaments occur at the tip of the wing-box, close to the point where the load is introduced.

moved backwards to the ligaments close to the root.

In order to reduce the local deformations occurring at the wing-box skin, a pair of inner ribs as described in Subsection 3.3.1 are added to the model. This element adds stiffness to the structure in bending. Now, the colour contour with the total rotational displacement is shown in Figure 4.28. Here it can be seen that the ligaments that start to buckle are located at the same position that they were when the model did not incorporate inner ribs. However, now the magnitude of local deformation at the wing-box skin has decreased due to the stiffness added to the structure as a result of the inner ribs inclusion.

However, for this last case, the simulation was only able to converge up to 13% of the prescribed load. In order to progress further in the analysis, the use of automatic stabilization becomes necessary again. For this reason, in the final configuration, automatic stabilization through constant damping factor is used together with the inner ribs. A description of the response of the structure for this last case is presented in next chapter.

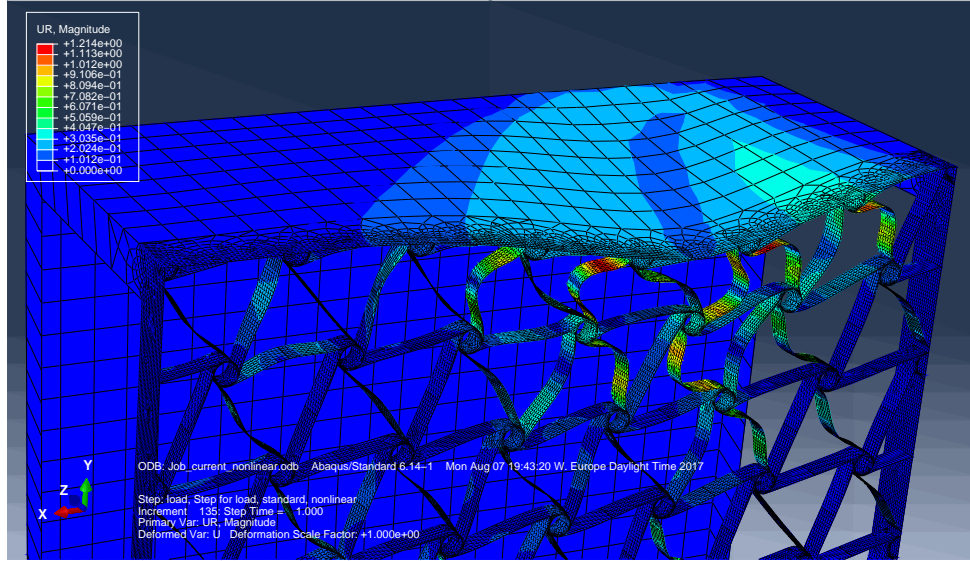


Figure 4.27: Model response without the use of inner ribs and with automatic stabilization. The simulation converged to the 100% of the prescribed load (800 N). The inclusion of artificial constant damping factor allows the simulation to achieve further load increments, overpassing the point at which the collapse of the structure occurs. For the considered configuration and under the prescribed load, severe local deformations occurs at the wing-box skin which is needed to be accounted for.

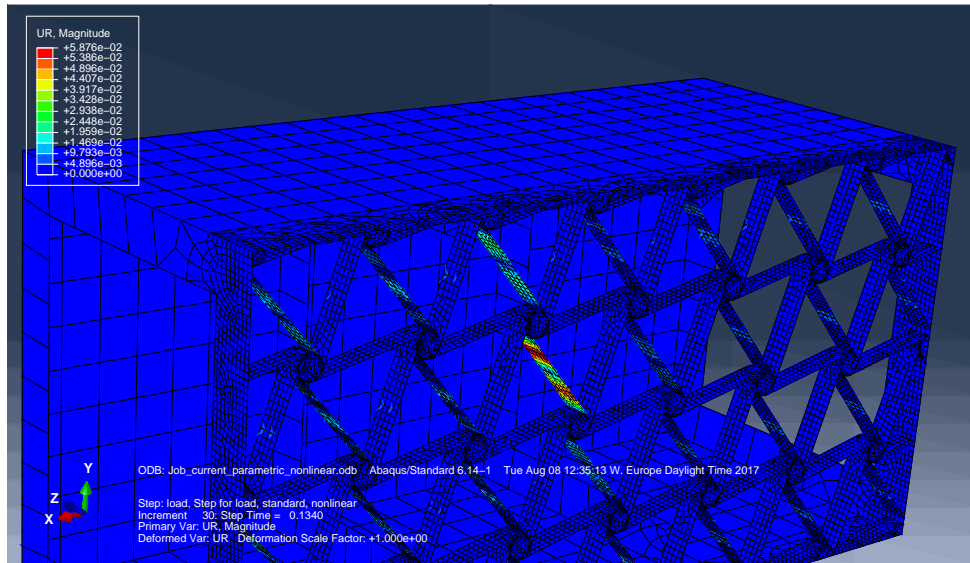


Figure 4.28: Model response incorporating inner ribs and without automatic stabilization. The simulation converged to the 13% of the prescribed load (800 N). The inner ribs have added stiffness to the structure in the bending.

Chapter 5

Simulations results

In the present chapter, results obtained from the simulations completed in Abaqus CAE are presented. Firstly, the general response of the structure is characterized for the baseline configuration. A description of the elastic instability that the chiral ligaments undergo is included. Also, the nonlinear global response of the wing-box in twist angle is shown.

Secondly, results obtained from the parametric study performed are presented. Here, the influence of each of the parameters on the nonlinear response in twist of the structure and the buckling phenomena are shown.

5.1 General response characterization

In this section, the general response of the model is characterized. For the wing-box, the nominal value of its characteristic parameters are those shown in Table 3.2, while Tables 3.1 and 3.3 contain the nominal values of the main parameters for the chiral lattice and for the ribs, respectively. Also, the baseline configuration incorporates a pair of inner ribs and the load is applied on a single mesh node on the upper flange of the tip rib, as described in Subsection 4.2.2.

In the simulations, automatic stabilization through constant damping factor is included. For this case, the response of the structure when 47% of the prescribed load has been applied is the one shown in Figure 5.1. It can be seen that buckling starts at the tip region of the lattice. Several lattice have started to buckle as an initial response to the load. However, in a further load increment, buckling phenomena moves backwards and those ligaments located close to the root and at a higher y coordinate, start to deform even more severely. At this point, when 47% of the prescribed load has been applied, the structure collapses and the twist increases for small increments in the applied load. This can be seen in Figure 5.4.

This is the point at which the local instabilities are such that there is need of adding artificial damping factor in order to capture the structure dynamics. After this point, artificial damping is essential for the

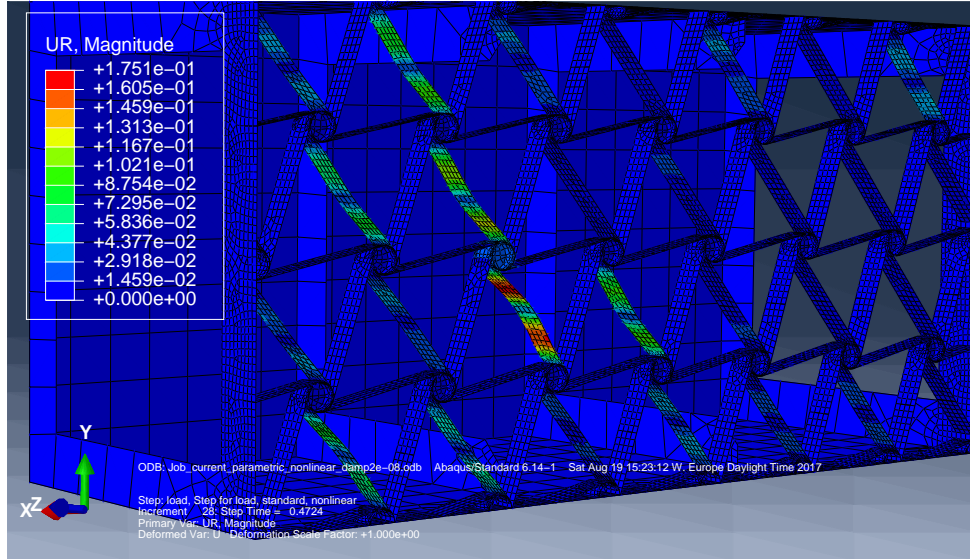


Figure 5.1: Baseline model response when the fraction of load applied equals to 47% of the prescribed load (700 N). Buckling has appeared at the tip of the wing-box due as an initial response to the load that it is being introduced.

simulation to continue. As it was explained in Subsection 4.2.5, special care needs to be taken to ensure that the inclusion of artificial damping factor is not leading to inaccurate results due to over-damping of the structure. This can be done by comparing the fraction of the static energy that it is dissipated with to the external work that is introduced into the system. The Figure 5.2 makes this comparison possible. It can be seen that effectively, the energy statically dissipated through automatic stabilization is negligible in comparison with the external work. This figure also shows the abrupt increment in external work at the point where the structure collapses due to sudden buckling of the chiral ligaments.

In order to see the overall system response as load increases, a displacement-force curve can be plotted. The Figure 5.3 shows the wing-box twist adaptation as load increases. In this plot, results from the nonlinear simulations are shown as the set of scatter points while the dotted line represents the forecast response by the linear simulation. In the case shown, the linear simulation arises a value for the twist at the wing-box tip ϕ_{tip} equal to -0.196 degrees while the nonlinear simulation predicts a final twist of -1.248 degrees. This shows that the problem under study is highly nonlinear.

The nonlinear response also shows the point where the structure collapses, when 73% of the prescribed load has been applied. The colour contour plot of the total rotational displacement over the solution model is shown in Figure 5.4. This figure shows severe buckling occurring at the root of the lattice chiral structure.

In a further stage of the simulation, the structure enters the post-buckling regime and the instabilities propagate to other parts of the lattice chiral structure, as it can be seen in Figure 5.5. Here it can be seen that the instabilities are more generalized and buckling appears in more ligaments apart from those at the

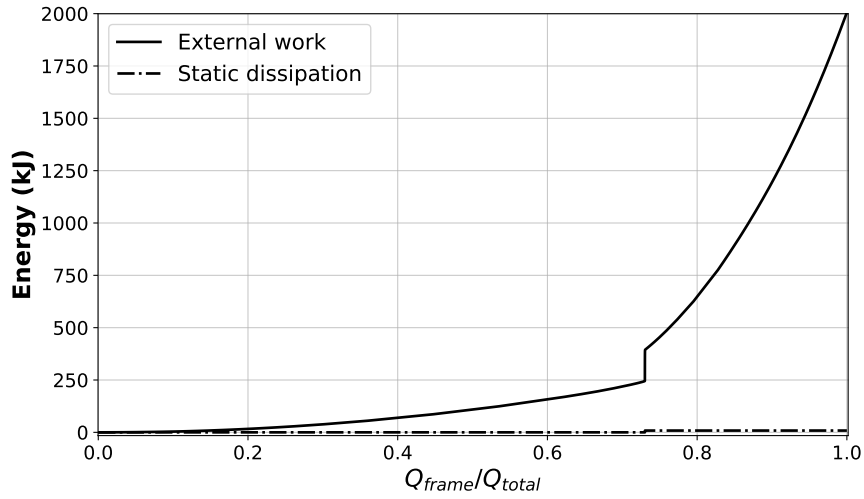


Figure 5.2: External work and static dissipation for a simulation of the baseline configuration. It can be seen that the static dissipation through automatic stabilization is negligible in comparison with the external work showing that the inclusion of artificial damping factor is unluckily to be leading to inaccurate results. The abrupt change in the external work shows the point where structure collapses due to sudden buckling of the chiral ligaments.

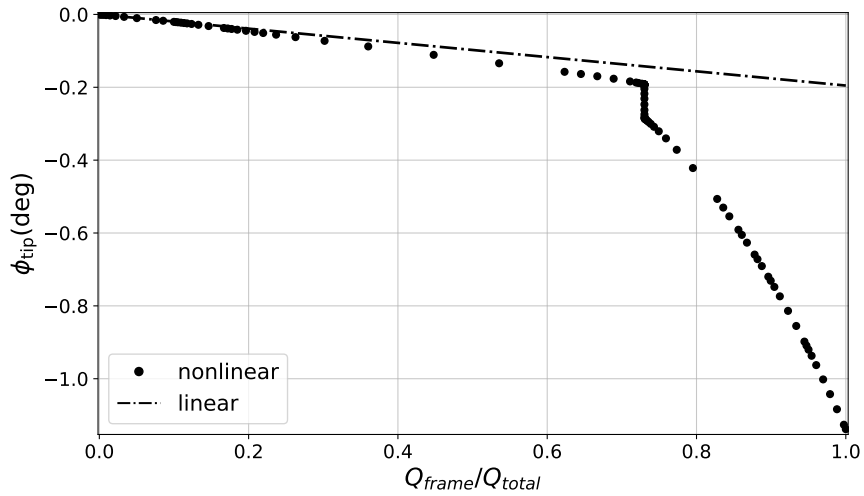


Figure 5.3: Displacement-force curve for the baseline configuration. Two breakdowns for the buckling deformation are shown in the plot. The first one is located at the point where the fraction of applied load equals to 73% and the second one at the point where the fraction is 96%.

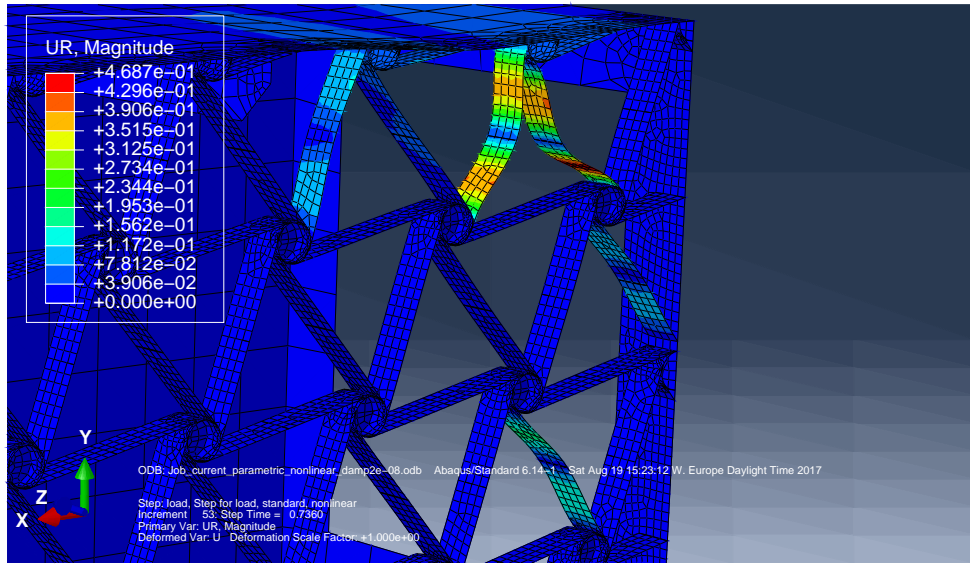


Figure 5.4: Baseline model response when the fraction of load applied equals to 73% of the prescribed load (700 N). Severe buckling deformation appears in those chiral ligaments located at the root and with a higher y coordinate. This is the point when the structure collapses and the twist increases for small increments in load.

root. Under certain conditions, this generalized state can produce a second sudden variation in the slope of the displacement-force curve, showing a third effective stiffness.

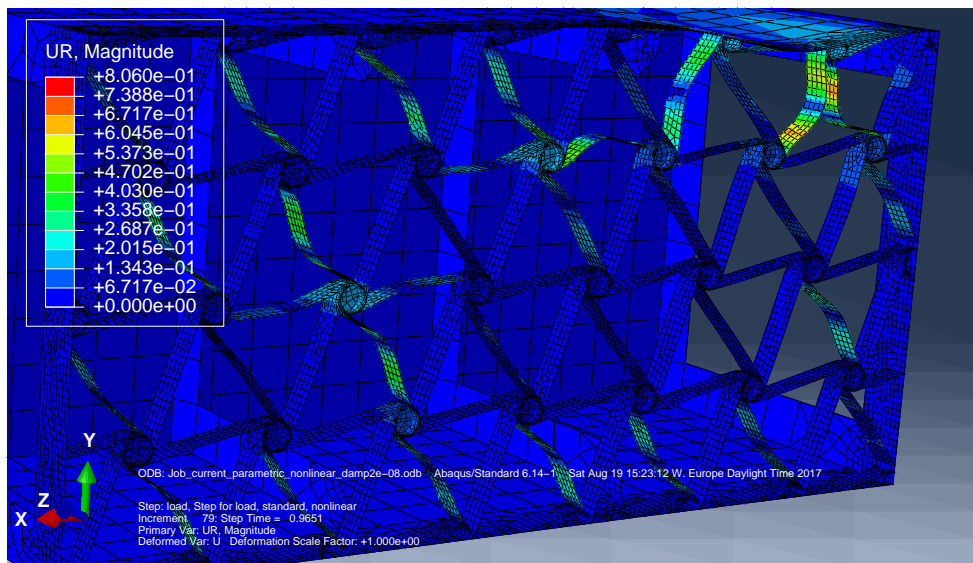


Figure 5.5: Baseline model response when the fraction of load applied equals to 96% of the prescribed load (700 N). In this case, not only the ligaments located at the root show severe buckling but also, other located at different points of the chiral lattice has started to buckle at the same time, inducing rapidly growing deformation for small increments in load.

5.2 Parametric study on the computational model

The aim of this section is to show the effect of each parameter on the nonlinear response of the structure. The parameters included in the analysis are the following:

- Wing-box thickness t_{box}
- Number of unit cells in the transversal direction M
- Number of unit cells in the spanwise direction N
- Chiral node depth B_{chi}
- Chiral node radius r_{chi}
- Chiral lattice thickness t_{chi}
- Chiral ligament half length L_{chi}
- Dimensionless ligament eccentricity ε_{chi}

5.2.1 Wing-box thickness

In the present subsection the effect of different values for the wing-box thickness t_{box} on the structure response is investigated. The geometric representation of the wing-box thickness t_{box} can be seen in Figure 3.10.

The results from the simulations carried out can be seen in Table 5.1. In the table, the twist at the tip of the wing-box for the Abaqus nonlinear simulation ϕ_{tip} and for the linear simulation $\tilde{\phi}_{\text{tip}}$ are shown. This result is obtained by evaluating the value of the angular deformation u at a number of mesh elements located in different parts of the wing-box tip rib, as explained in the Subsection 3.3.7. Therefore, the maximum deviation between the individual values and the calculated mean twist has also been included. Finally, the Table 5.1 shows the maximum vertical displacement found in the nodes located in the upper wing-box skin.

The displacement-force curve for each of the values of t_{box} studied can be seen in Figure 5.6. It can be seen that the structure collapses for the cases of $t_{\text{box}} = 0.6 \text{ mm}$, $t_{\text{box}} = 0.8 \text{ mm}$ and $t_{\text{box}} = 1.0 \text{ mm}$, when the load applied reaches 40%, 64% and 97% of the total prescribed load, respectively. This result already shows the relevance of the wing-box thickness t_{box} in the triggering of the collapsing buckling. A detailed view of the nonlinear response of the structure for the different analysed cases is shown in Figure 5.7. Here, the difference between the linear and the nonlinear is represented and it can be seen that the gap between the two responses increases as the value of t_{box} decreases. In the Table 5.1, comparing the values of ϕ_{tip} and $\tilde{\phi}_{\text{tip}}$ provides information of the huge difference in the final value of the twist between the nonlinear and the linear response when the buckling occurs and it is captured in the simulation. For

t_{box} (mm)	ϕ_{tip} (deg)	$e(\phi_{\text{tip}})$ (%)	$\tilde{\phi}_{\text{tip}}$ (deg)	$e(\tilde{\phi}_{\text{tip}})$ (%)	v_{\max}	$\hat{z}_{v_{\max}}$	$\hat{x}_{v_{\max}}$	
0.6	-14.331	11.13	-0.27	-14.259	0.121	-85.506	1	0.971
0.8	-1.934	11.43	-0.223	-15.178	0.546	-15.915	1	0.334
1	-0.403	14.651	-0.2	-19.923	0.546	-4.741	1	0.334
1.2	-0.221	15.031	-0.178	-21.074	0.121	-1.246	1	0.971

Table 5.1: Results from the parametric study on the wing-box thickness t_{box} . The results show the mean twist at the tip of the wing-box for the Abaqus nonlinear simulation ϕ_{tip} and for the linear simulation $\tilde{\phi}_{\text{tip}}$. The maximum relative error of the mean calculation, expressed as percentage, for these two magnitudes is $e(\phi_{\text{tip}})$ and $e(\tilde{\phi}_{\text{tip}})$, respectively. The table also shows the maximum vertical displacement v_{\max} among all the mesh nodes located on the upper skin of the wing-box and the dimensionless position in the spanwise direction $\hat{x}_{v_{\max}}$ and in the chordwise direction $\hat{z}_{v_{\max}}$ of the node that shows $v = v_{\max}$.

example, for $t_{\text{box}} = 0.8$ mm, the value of the tip twist from the linear simulation $\tilde{\phi}_{\text{tip}}$ is 12% of the value estimated from the nonlinear simulation ϕ_{tip} .

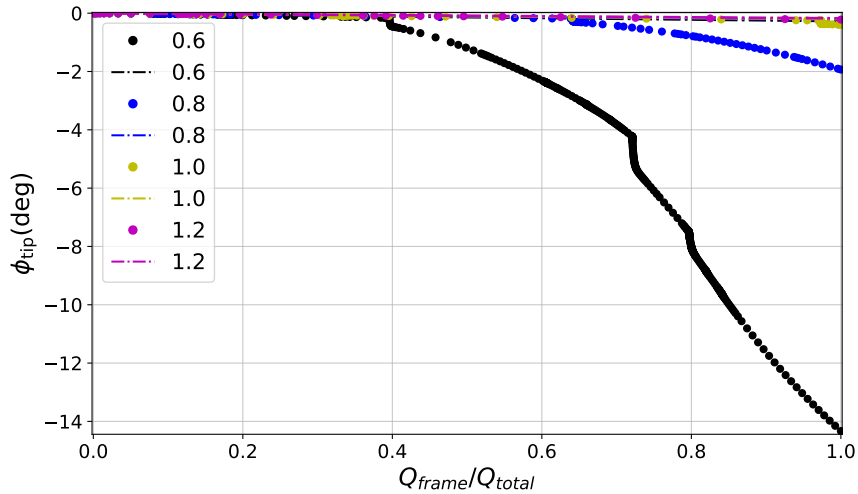


Figure 5.6: Displacement-force curve for various values of the wing-box thickness t_{box} . For all the cases shown, the force applied was located on the upper flange of the tip rib and its magnitude was equal to -800 N.

The differences in response for the different cases are also visually evaluated using colour contour plots of total rotational displacement. Such a visualization is shown in Figure 5.8 for the case of wing-box thickness $t_{\text{box}} = 1.2$. It can be seen that buckling does not propagate to other parts of the lattice and it stays where it had appeared on first place, at the first ligaments after the inner rib located further from the root. In this case, the value of wing-box thickness $t_{\text{box}} = 1.2$ mm makes the structure sufficiently stiff in bending and therefore, buckling does not appear at the root causing the structure collapse.

On the other hand, in Figure 5.9 the same plot is shown for a value of wing-box thickness $t_{\text{box}} = 0.8$

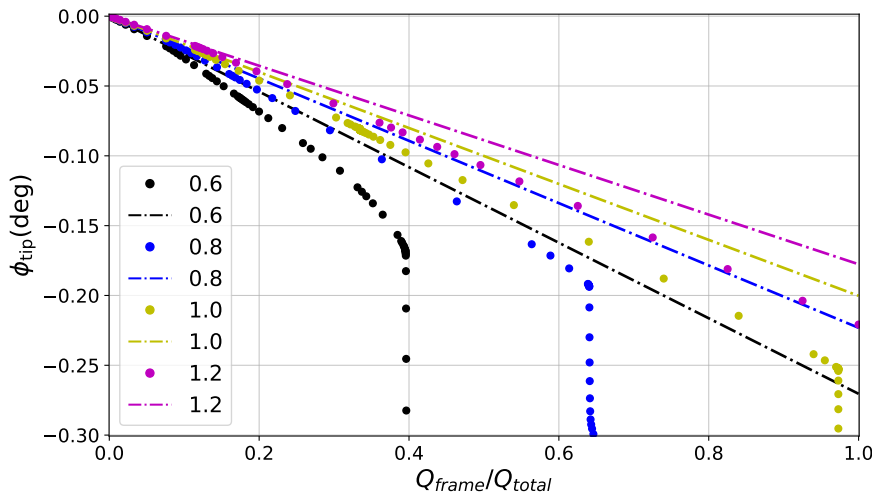


Figure 5.7: Detail of the displacement-force curve for various values of the wing-box thickness t_{box} . For all the cases shown, the force applied was located on the upper flange of the tip rib and its magnitude was equal to -800 N.

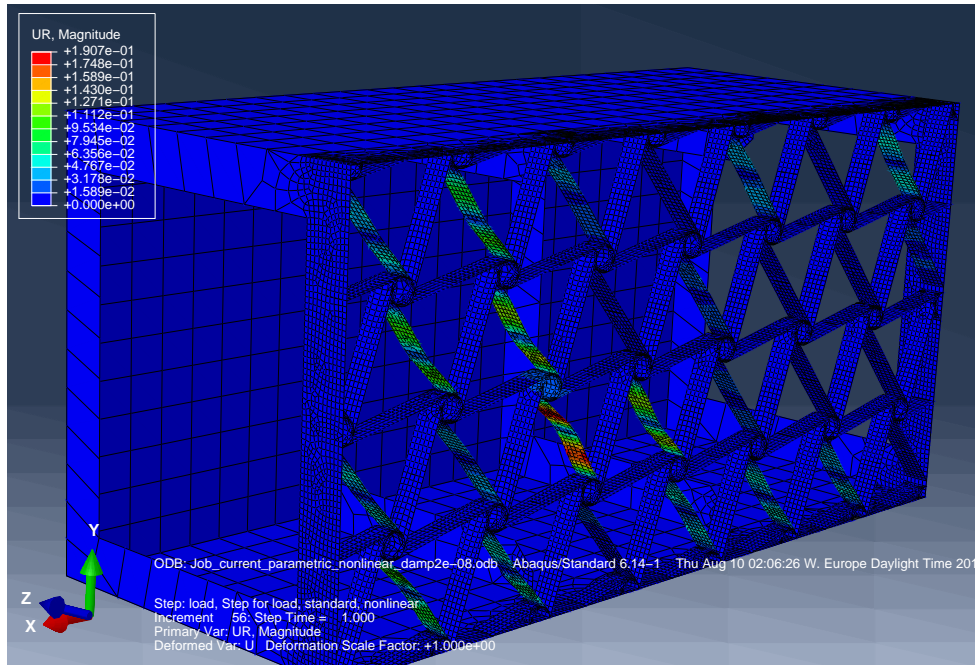


Figure 5.8: Color contour representation of the total angular displacement of the mesh elements on the deformed structure for $t_{\text{box}} = 1.2$ mm. This case is shown after all the prescribed load (800 N) has been applied. The elastic instabilities had appeared at the wing tip and they have not propagated to the root causing the structure collapse.

mm, after all the prescribed load (800 N) has been applied. This figure shows how severe deformation due to buckling is occurring in the ligaments at the root. It is possible to see that some local deformation has been induced into the upper skin of the wing-box in between the root and the first inner rib. As shown in Table 5.1, for the case $t_{\text{box}} = 0.8$ mm, the point with maximum displacement v in the y direction is shown to appear close to the root, where $\hat{x}_{v_{\max}} = 0.334$.

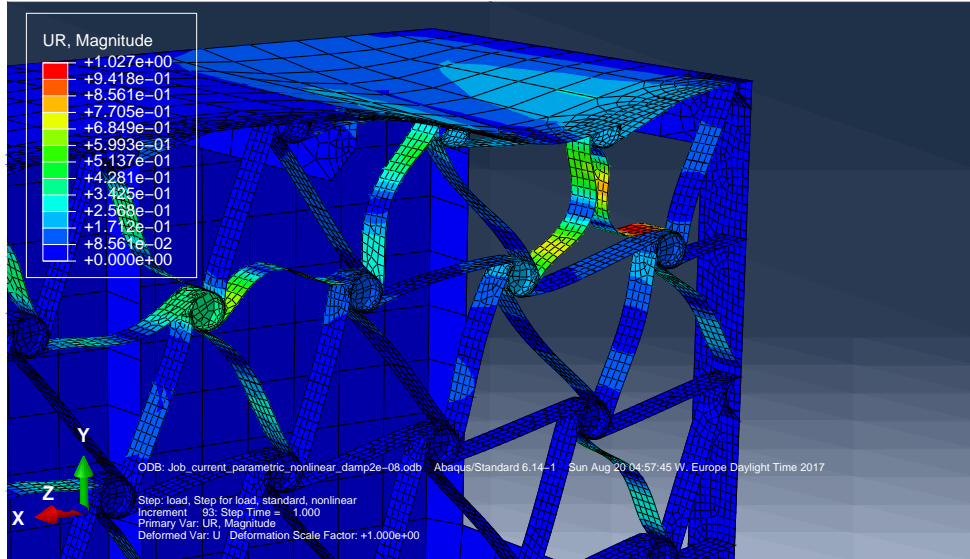


Figure 5.9: Color contour representation of the total angular displacement of the mesh elements on the deformed structure for $t_{\text{box}} = 0.8$ mm. This case is shown after all the prescribed load (800 N) has been applied. The appearance of elastic instabilities at the ligaments at the root has induced the structure collapse and local deformation on the wing-box skin.

Finally, for the case of $t_{\text{box}} = 0.6$ mm, it can be seen that the collapse of the structure occurs when just 40% of the prescribed load has been applied. For this case, Figure 5.6 shows a second change in the slope of the force-displacement curve when approximately 72% of the prescribed load has been applied. This second stage of the collapse of the structure appears when the elastic instabilities propagate from the ligaments at the root to other ligaments located closer to the tip of the structure. In Figure 5.10, this generalized buckling can be seen at the moment when the second change in the slope of the force-deformation curve occurs. All those ligaments that have just started to deform, causing the wing-box sudden adaptation in twist for the second time.

A further study is performed in order to see the relationship between the wing-box thickness and the value of the force applied that induces the structure collapse. As a result, the plot shown in Figure 5.11 is produced. It can be seen that relatively small variations in t_{box} produce considerable increments in the load required to trigger the buckling-induced twist adaptation of the wing-box, as it has been already mentioned. For example, for $t_{\text{box}} = 0.6$ mm, the magnitude of the force required to activate the mechanism is 300 N, while for $t_{\text{box}} = 0.8$ mm, the magnitude raises up to 525 N.

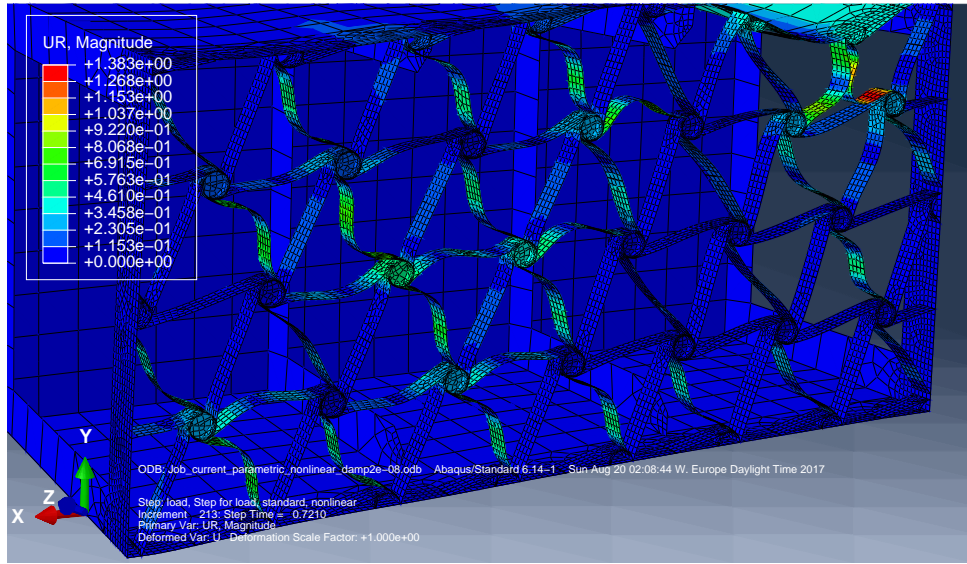


Figure 5.10: Color contour representation of the total angular displacement of the mesh elements on the deformed structure for $t_{\text{box}} = 0.6 \text{ mm}$. This case is shown when 72% of the prescribed load (800 N) has been applied. The figure shows how the elastic instabilities have extended to the majority of the ligaments in the chiral lattice.



Figure 5.11: Force that induces the structure to collapse as a function of the wing-box thickness t_{box} .

5.2.2 Number of unit cells in the chiral lattice

Now the effect of the number of units cells in the transversal direction M and in the spanwise direction N on the structural response is investigated. These two parameters are responsible of the height and the length of the wing-box, respectively. The division of the chiral lattice in M units cells in the transversal direction and in N units cells in the spanwise direction can be seen in Figure 3.7.

Firstly, the number of unit cells in the transversal direction M is varied. This parameter modifies the height of the model. Similarly as it was done for the study of the wing-box thickness t_{box} influence in the structure response, the results from the different simulations are shown in Table 5.2. Also, the displacement-force curve is shown in Figure 5.12. It can be seen from the results that increasing M results in a decrement of the structure sensitivity to buckling. In order to be able to onset the elastic instabilities for $M > 3$, the simulations are executed for a prescribed load of 1200 N.

M	ϕ_{tip} (deg)	$e(\phi_{\text{tip}})$ (%)	$\tilde{\phi}_{\text{tip}}$ (deg)	$e(\tilde{\phi}_{\text{tip}})$ (%)	v_{\max}	$\hat{z}_{v_{\max}}$	$\hat{x}_{v_{\max}}$
3	-9.672	11.43	-0.335	-15.177	-55.962	1	0.971
4	-1.221	18.13	-0.289	-24.409	-11.467	1	0.546
5	-0.385	15.3	-0.267	-21.211	-1.747	0.9	0.971

Table 5.2: Results from the parametric study on the number of unit cells in the transversal direction M . The results show the mean twist at the tip of the wing-box for the Abaqus nonlinear simulation ϕ_{tip} and for the linear simulation $\tilde{\phi}_{\text{tip}}$. The maximum relative error of the mean calculation, expressed as percentage, for these two magnitudes is $e(\phi_{\text{tip}})$ and $e(\tilde{\phi}_{\text{tip}})$, respectively. The table also shows the maximum vertical displacement v_{\max} among all the mesh nodes located on the upper skin of the wing-box and the dimensionless position in the spanwise direction $\hat{x}_{v_{\max}}$ and in the chordwise direction $\hat{z}_{v_{\max}}$ of the node that shows $v = v_{\max}$.

From the results shown in Table 5.5 it can be seen how for the case of $M = 3$, the point that shows $v = v_{\max}$ is located at the wing-box tip where $\hat{x}_{v_{\max}} = 0.971$, due to the high twist of the structure. However, for $M = 4$, the location of the point with $v = v_{\max}$ is at $\hat{x}_{v_{\max}} = 0.546$ showing the point at which local deformation occurs. The value of the twist at the tip ϕ_{tip} has been reduced in 12% of what it was for $M = 3$. This shows that the structure increases its shear stiffness as the height of the wing-box increases. For $M = 5$, the structure is sufficiently stiff that v_{\max} appears approximately at the point where the load is applied and the collapse of the structure does not occur. This shows that deformation is only achieved in the vicinity of the load introduction point due to the high stiffness in shear of the structure.

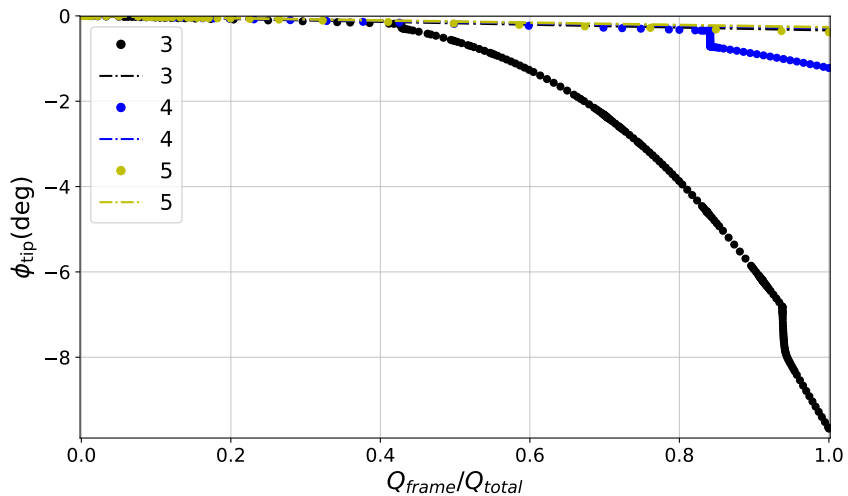


Figure 5.12: Displacement-force curve for various values of the number of unit cells in the transversal direction M . For all the cases shown, the load introduction point was located in the middle of the upper flange of the tip rib and its magnitude was equal to -1200 N.

The effects of the variation of the number of unit cells in the spanwise direction N , parameter responsible of the wing-box length, are investigated next. The results from the parametric study carried out are shown in Table 5.3. The displacement-force curve for the simulations carried out is shown in Figure 5.13. It can be seen that the bigger the wing-box length, the earlier that the buckling of the lattices cause the collapse of the structure.

N	ϕ_{tip} (deg)	$e(\phi_{\text{tip}})(\%)$	$\tilde{\phi}_{\text{tip}}$ (deg)	$e(\tilde{\phi}_{\text{tip}})(\%)$	v_{\max}	$\hat{z}_{v_{\max}}$	$\hat{x}_{v_{\max}}$
7	-0.215	13.74	-0.165	-18.212	-1.182	1	0.971
8	-1.596	14.222	-0.203	-18.444	-14.267	1	0.334
9	-3.419	9.419	-0.231	-12.654	-20.361	1	0.324
10	-10.516	7.756	-0.27	-10.353	-61.202	1	0.971
11	-22.16	6.466	-0.321	-8.819	-138.196	1	0.971
12	-31.558	5.316	-0.374	-7.222	-207.335	1	0.971

Table 5.3: Results from the parametric study on the number of unit cells in the spanwise direction M . The results show the mean twist at the tip of the wing-box for the Abaqus nonlinear simulation ϕ_{tip} and for the linear simulation $\tilde{\phi}_{\text{tip}}$. The maximum relative error of the mean calculation, expressed as percentage, for these two magnitudes is $e(\phi_{\text{tip}})$ and $e(\tilde{\phi}_{\text{tip}})$, respectively. The table also shows the maximum vertical displacement v_{\max} among all the mesh nodes located on the upper skin of the wing-box and the dimensionless position in the spanwise direction $\hat{x}_{v_{\max}}$ and in the chordwise direction $\hat{z}_{v_{\max}}$ of the node that shows $v = v_{\max}$.

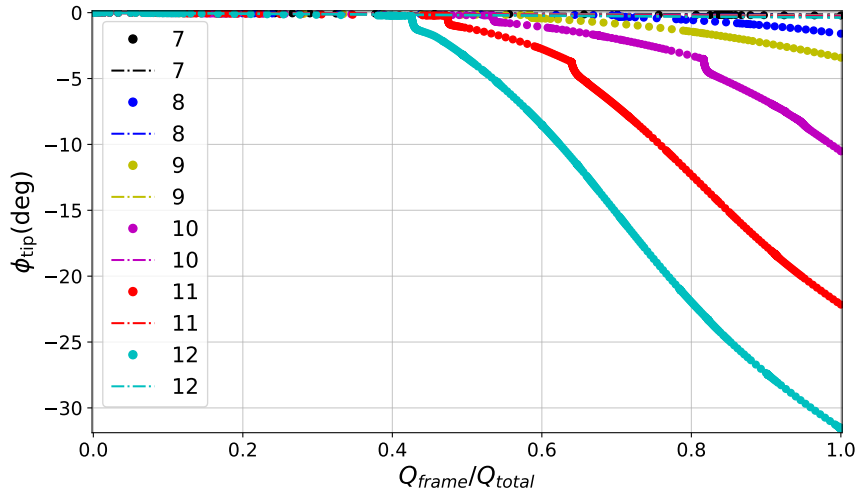


Figure 5.13: Displacement-force curve for various values of the number of unit cells in the spanwise direction N . For all the cases shown, the load introduction point was located in the middle of the upper flange of the tip rib and its magnitude was equal to -700 N.

In Figure 5.13, a second change in the slope of the curve for the cases of $N = 10$ and $N = 11$ can be seen. This happens when, as explained in Section 5.1, the buckling phenomena progresses from the

ligaments at the root to be more generalized in other parts of the structure. This characteristic can be seen in Figure 5.14, where the response of the structure for the case of $N = 10$ and load fraction of 81% is shown.

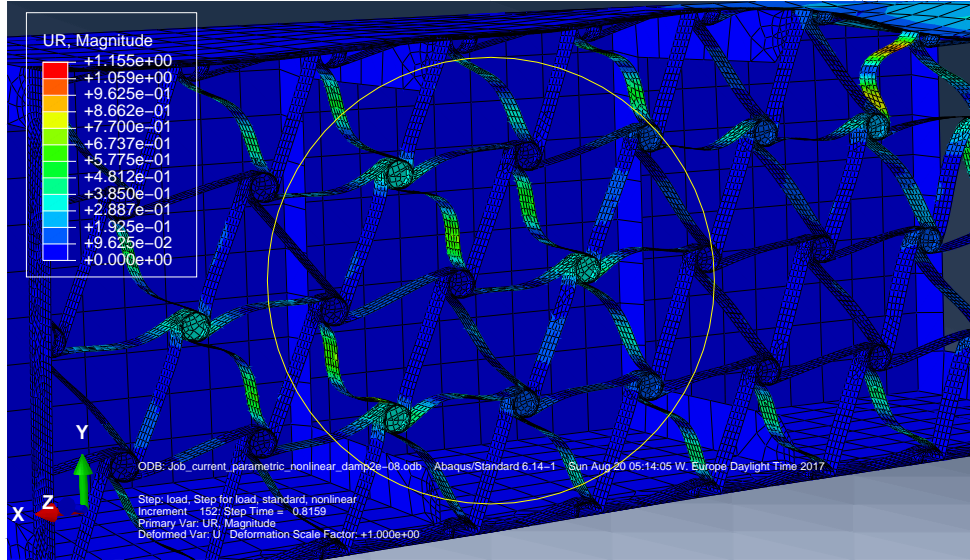


Figure 5.14: Colour contour showing the total rotational displacement when the fraction of load applied equals to 81% of the prescribed load (700 N) and $N = 10$. The plot shows how the buckling phenomena is generalized for the whole chiral structure.

When plotting the force that makes the structure to collapse against the corresponding wing-box length, the Figure 5.15 is produced. This graphic shows that, for example, a force of 300 N is required to induce the collapse of a wing-box with length equal to 1000 mm.

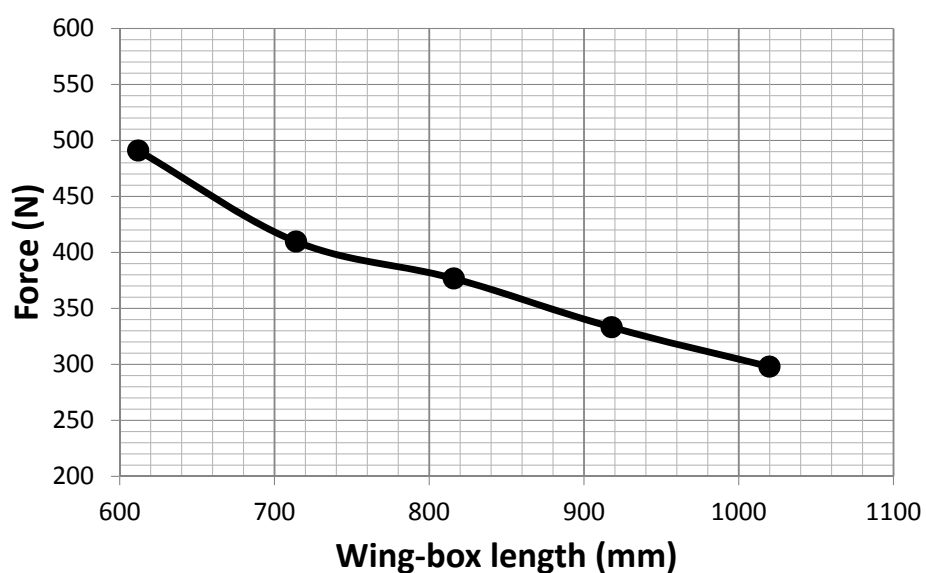


Figure 5.15: Force that induces the structure to collapse as a function of the wing-box length.

5.2.3 Chiral lattice parameters

In the present subsection, the following parameters of the chiral lattice structure are varied and its effect of the system response is shown:

- Chiral node depth B_{chi}
- Chiral node radius r_{chi}
- Chiral lattice thickness t_{chi}
- Chiral ligament half length L_{chi}
- Dimensionless ligament eccentricity ε_{chi}

Dimensionless chiral ligament eccentricity ε_{chi}

The first of the chiral structure parameters that is studied is the ligament eccentricity e_{chi} , in its dimensionless form ε_{chi} . The geometrical meaning of this parameter can be seen in the sketch shown in Figure 3.8. The numeric results from the simulations carried out can be seen in Table 5.4.

ε_{chi}	ϕ_{tip} (deg)	$e(\phi_{\text{tip}})$ (%)	$\tilde{\phi}_{\text{tip}}$ (deg)	$e(\tilde{\phi}_{\text{tip}})$ (%)	v_{\max}	$\hat{z}_{v_{\max}}$	$\hat{x}_{v_{\max}}$
0	-0.372	12.092	-0.182	-13.82	-4.147	1	0.546
0.001	-1.194	11.467	-0.191	-15.24	-11.731	1	0.334
0.0015	-0.703	15.571	-0.16	-10.22	-7.122	1	0.546
0.01	-1.596	14.222	-0.203	-18.44	-14.267	1	0.334
0.05	-1.275	14.18	-0.223	-18.27	-12.298	1	0.334
0.1	-0.282	14.065	-0.229	-18.3	-2.044	1	0.334

Table 5.4: Results from the parametric study on the dimensionless chiral ligament eccentricity ε_{chi} . The results show the mean twist at the tip of the wing-box for the Abaqus nonlinear simulation ϕ_{tip} and for the linear simulation $\tilde{\phi}_{\text{tip}}$. The maximum relative error of the mean calculation, expressed as percentage, for these two magnitudes is $e(\phi_{\text{tip}})$ and $e(\tilde{\phi}_{\text{tip}})$, respectively. The table also shows the maximum vertical displacement v_{\max} among all the mesh nodes located on the upper skin of the wing-box and the dimensionless position in the spanwise direction $\hat{x}_{v_{\max}}$ and in the chordwise direction $\hat{z}_{v_{\max}}$ of the node that shows $v = v_{\max}$.

The force-deformation curve for the range of simulations carried out can be seen in Figure 5.16. Here it can be seen that the collapse of the structure occurs for all the cases except for $\varepsilon_{\text{chi}} = 0.1$. The deformation state of the structure for this case can be seen in Figure 5.17 that shows how the excessive eccentricity of the ligaments keep them from buckling and causing the structure collapse.

The Figure 5.16 also shows that the case of $\varepsilon_{\text{chi}} = 0.0$, that is when the ligaments are flat, is not the case that shows an earlier onset of the instabilities, as it would be expected. Instead, for $\varepsilon_{\text{chi}} = 0.0$,

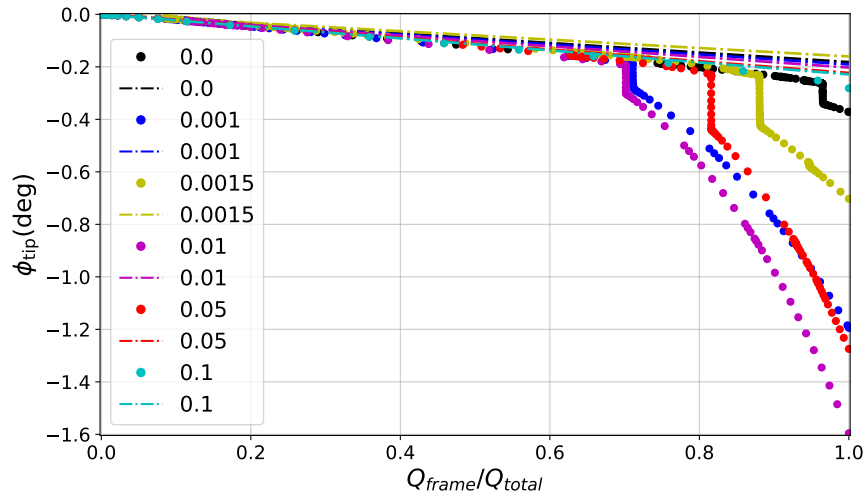


Figure 5.16: Displacement-force curve for various values of the dimensionless chiral ligament eccentricity ϵ_{chi} . The plot shows how the collapse of the structure occurs for all the cases except for $\epsilon_{\text{chi}} = 0.1$.

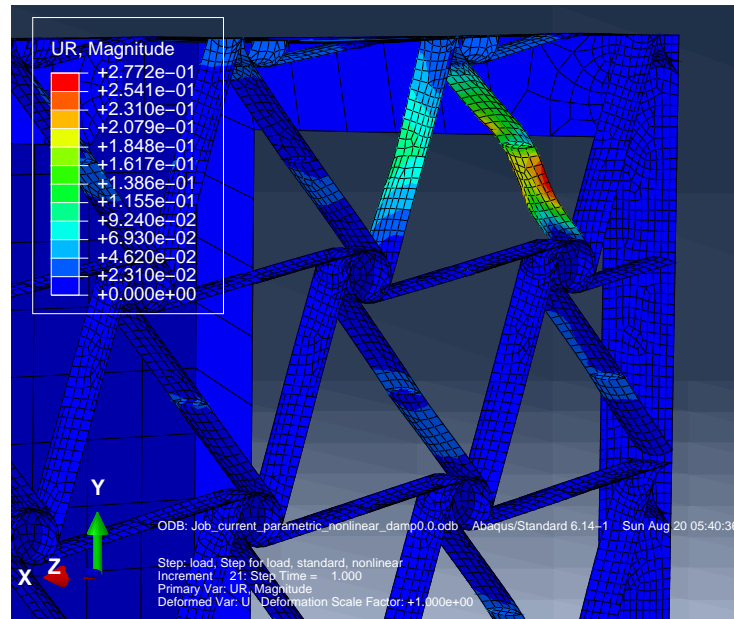


Figure 5.17: Colour contour showing the total rotational displacement when the fraction of load applied equals to 100% of the prescribed load (700 N) and $\epsilon_{\text{chi}} = 0.1$. For this case, the excessive ligament eccentricity at the end of the simulation keeps it from buckling and causing the structure collapse.

the structure shows the later onset of the instabilities, when the applied load is 96% of the prescribed load. On the other hand, the collapse of the structure is triggered when the applied load is 68% of the prescribed load for the case of $\varepsilon_{\text{chi}} = 0.001$. This particular behavior is investigated by looking at the deformed plots on the Abaqus visualization module. In Figures 5.18 and 5.19 the deformed state of the ligaments at the point when collapse of the structure occurs is shown for the cases of $\varepsilon_{\text{chi}} = 0.0$ and $\varepsilon_{\text{chi}} = 0.001$, respectively. It can be seen that the buckling mechanism in the ligaments changes between the two cases. In particular, it can be seen that for $\varepsilon_{\text{chi}} = 0.0$ the onset of the instabilities induces some rotation to the lattice nodes located on the upper part. The particular geometry of the model is believed to be the reason behind this differences in the appearance of buckling at the ligaments at the root.

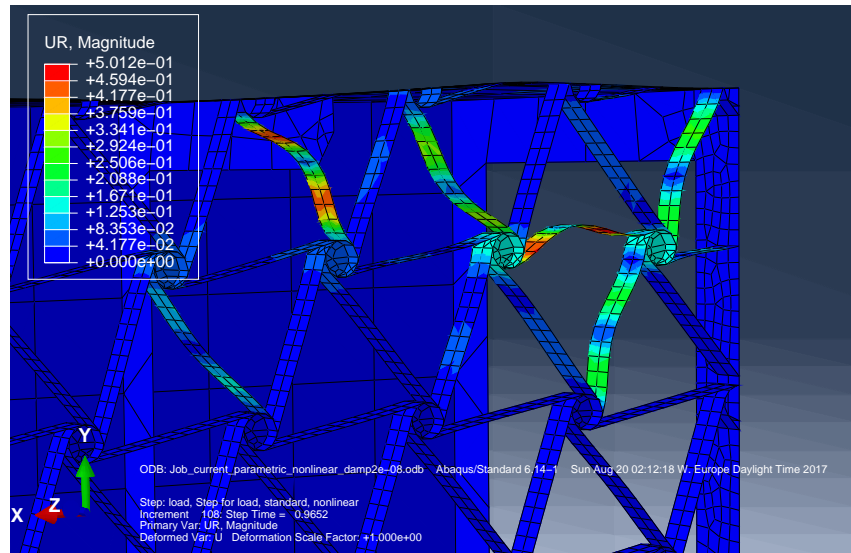


Figure 5.18: Colour contour showing the total rotational displacement when the fraction of load applied equals to 96% of the prescribed load (700 N) and $\varepsilon_{\text{chi}} = 0.0$. In this case, the onset of the instabilities affect the rotation of the lattice nodes, in particular. There are two ligaments on the upper part that remain undeformed.

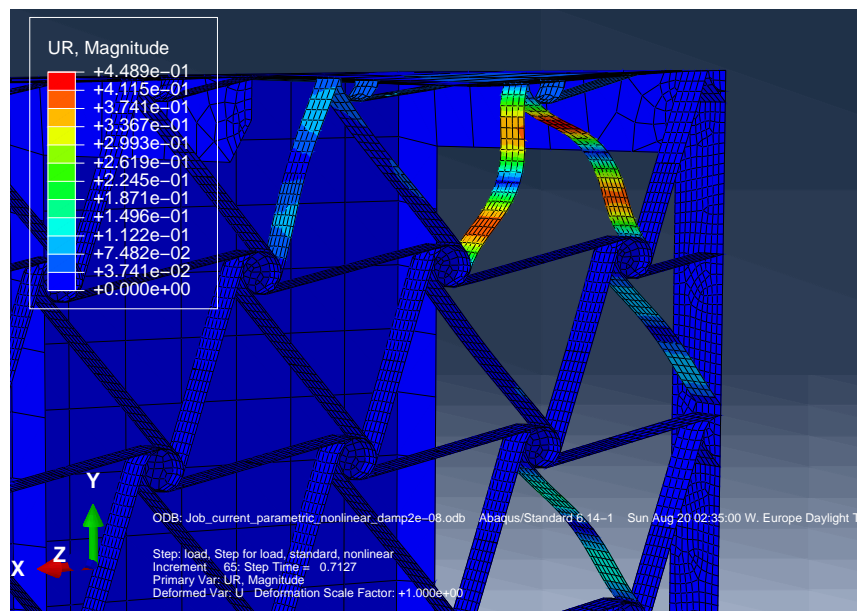


Figure 5.19: Colour contour showing the total rotational displacement when the fraction of load applied equals to 71% of the prescribed load (700 N) and $\varepsilon_{\text{chi}} = 0.001$.

Chiral node depth B_{chi}

The numeric results from the parametric analysis on the chiral node depth B_{chi} can be seen in Table 5.5. The geometrical meaning of this parameter can be seen in the sketch shown in Figure 3.8. The displacement-force curve can be seen in Figure 5.20 for various values of B .

The Figure 5.21 shows a colour contour plot representing the rotation u around the x direction of the mesh elements located on the upper skin of the wing-box and close to the root. This is represented for the case of $B_{\text{chi}} = 30$ mm, at the moment when collapse of the structure occurs which is at 86% of the prescribed load and in the area where local deformation of the skin appear. Examination of the plot arises that the value of u in this area is approximately double to the case of $B_{\text{chi}} = 10$ mm, which can be seen in Figure 5.22. This shows that the bigger B_{chi} is, the more area is affected by the ligaments deformation when buckling occurs and the greater the local deformation is.

When plotting the force that makes the structure to collapse against the corresponding value of chiral node depth depth B_{chi} , the Figure 5.23 is produced.

B_{chi}	ϕ_{tip} (deg)	$e(\phi_{\text{tip}})(\%)$	$\tilde{\phi}_{\text{tip}}$ (deg)	$e(\tilde{\phi}_{\text{tip}})(\%)$	v_{\max}	$\hat{z}_{v_{\max}}$	$\hat{x}_{v_{\max}}$
10	-1.399	11.421	-0.217	-15.359	-12.735	1	0.334
20	-1.596	14.222	-0.203	-18.444	-14.267	1	0.334
30	-0.707	16.454	-0.216	-24.477	-7.975	1	0.334

Table 5.5: Results from the parametric study on chiral node depth B_{chi} . The results show the mean twist at the tip of the wing-box for the Abaqus nonlinear simulation ϕ_{tip} and for the linear simulation $\tilde{\phi}_{\text{tip}}$. The maximum relative error of the mean calculation, expressed as percentage, for these two magnitudes is $e(\phi_{\text{tip}})$ and $e(\tilde{\phi}_{\text{tip}})$, respectively. The table also shows the maximum vertical displacement v_{\max} among all the mesh nodes located on the upper skin of the wing-box and the dimensionless position in the spanwise direction $\hat{x}_{v_{\max}}$ and in the chordwise direction $\hat{z}_{v_{\max}}$ of the node that shows $v = v_{\max}$.

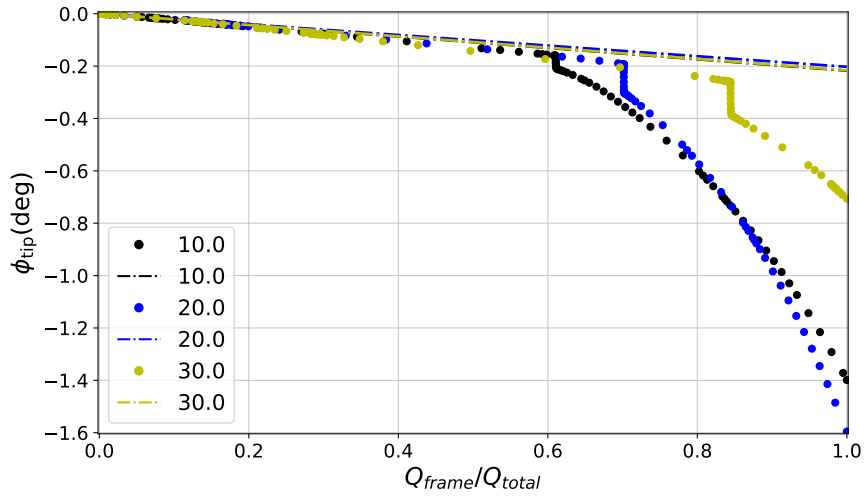


Figure 5.20: Displacement-force curve for various values of the dimensionless chiral node depth B_{chi} . Results show how the bigger the node depth B_{chi} is, the later the collapse of the structure occurs but the more abrupt is its.

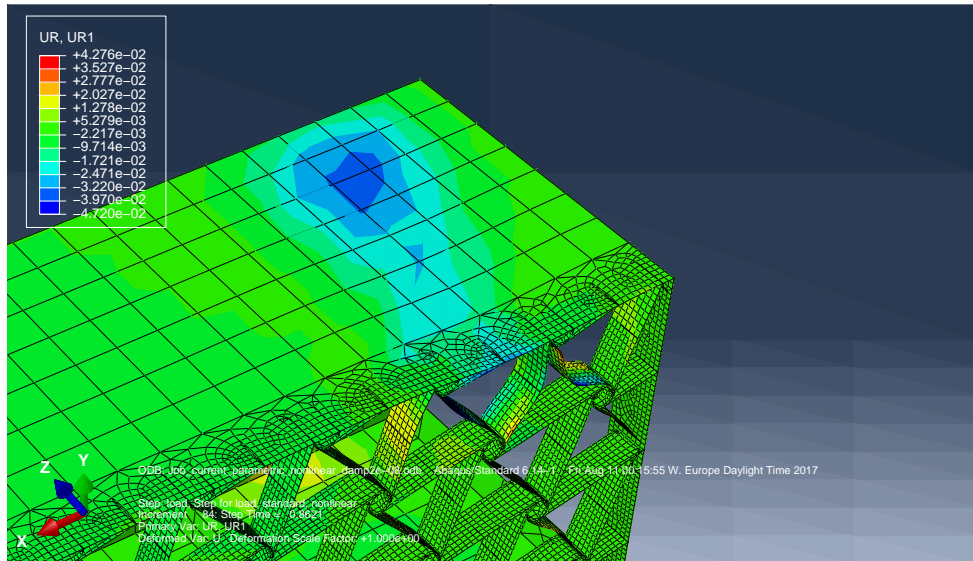


Figure 5.21: Colour contour showing the total rotational displacement when the fraction of load applied equals to 86% of the prescribed load (700 N) and $B_{\text{chi}} = 30$ mm. The plot shows a colour contour with the value of the rotational displacement u around the x direction at the moment in which the structure collapses. In the area where the local deformation occurs, the value of u is approximately equal to -0.033 rad.

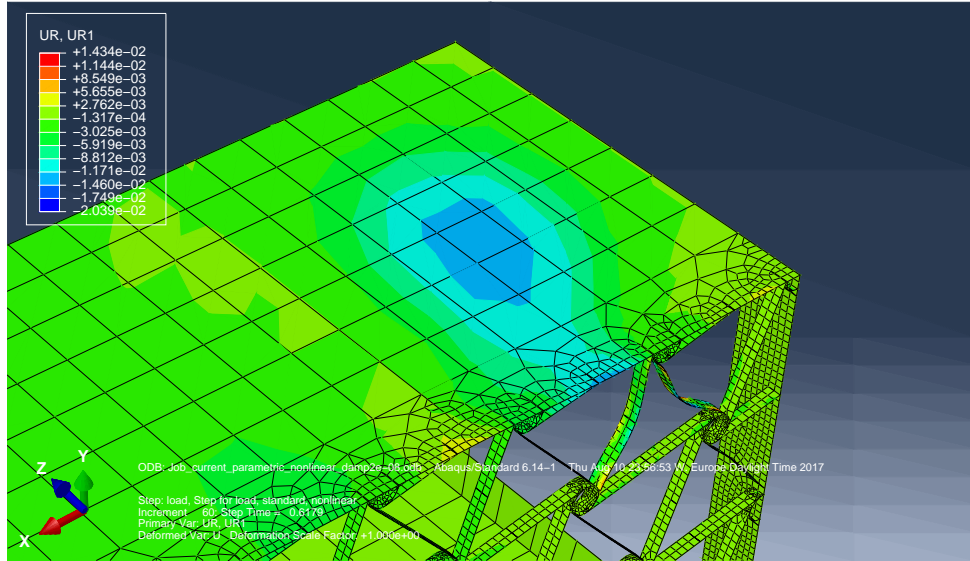


Figure 5.22: Colour contour showing the total rotational displacement when the fraction of load applied equals to 62% of the prescribed load (700 N) and $B_{\text{chi}} = 10 \text{ mm}$. The plot shows a colour contour with the value of the rotational displacement u around the x direction at the moment in which the structure collapses. In the area where the local deformation occurs, the value of u is approximately equal to -0.015 rad .

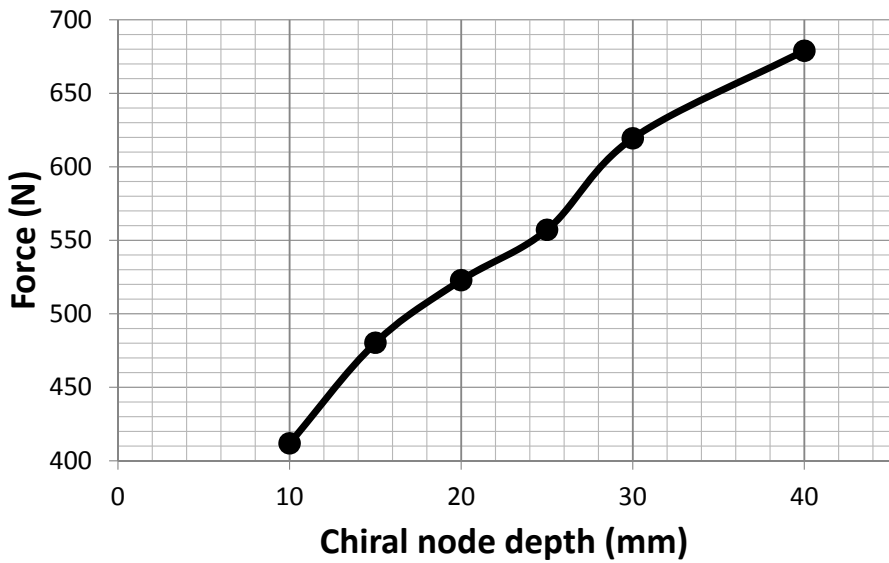


Figure 5.23: Force that induces the structure to collapse as a function of the chiral node depth B_{chi} .

Chiral node radius r_{chi}

A parametric study on different values of the chiral node radius r_{chi} is presented next. The geometrical meaning of this parameter can be seen in the sketch shown in Figure 3.8. The possible values of r_{chi} are limited by the geometry of the chiral lattice. For values $r_{\text{chi}} \leq 5$ mm, it is not possible to build the model due to interferences between the different ligaments that joined at each of the nodes. The numeric results from the simulations are presented in Table 5.6.

The displacement-force curve obtained from the simulations is shown in Figure 5.24. This curve shows how the structure collapses for all the analysed cases except for $r_{\text{chi}} = 17.5$ mm and $r_{\text{chi}} = 20$ mm. However, for the case of $r_{\text{chi}} = 17.5$ mm, buckling do not occur on the ligaments located at the root but in those located just after the inner rib located closer to the root, with smaller x . This can be seen in Figure 5.25. Then, the chiral node radius r_{chi} value shifts the position of the buckling ligaments that origin the collapse of the structure.

The variation of the force that makes the structure to collapse as a function of the chiral node radius r_{chi} can be seen in Figure 5.26. It can be seen that, the smaller the chiral node radius r_{chi} is, the earlier the structure collapse occurs.

r_{chi}	ϕ_{tip} (deg)	$e(\phi_{\text{tip}})$ (%)	$\tilde{\phi}_{\text{tip}}$ (deg)	$e(\tilde{\phi}_{\text{tip}})$ (%)	v_{\max}	$\hat{z}_{v_{\max}}$	$\hat{x}_{v_{\max}}$
7.5	-1.184	13.64	-0.171	-10.046	-11.586	1	0.331
10	-0.877	9.525	-0.17	-10.196	-9.831	1	0.334
12.5	-0.886	9.596	-0.17	-10.247	-10.051	1	0.337
15	-1.121	13.638	-0.173	-10.134	-11.677	1	0.342
17.5	-0.273	9.481	-0.171	-10.215	-4.169	1	0.568
20	-0.229	12.686	-0.171	-8.848	-1.433	1	1.026

Table 5.6: Results from the parametric study on chiral node radius r_{chi} . The results show the mean twist at the tip of the wing-box for the Abaqus nonlinear simulation ϕ_{tip} and for the linear simulation $\tilde{\phi}_{\text{tip}}$. The maximum relative error of the mean calculation, expressed as percentage, for these two magnitudes is $e(\phi_{\text{tip}})$ and $e(\tilde{\phi}_{\text{tip}})$, respectively. The table also shows the maximum vertical displacement v_{\max} among all the mesh nodes located on the upper skin of the wing-box and the dimensionless position in the spanwise direction $\hat{x}_{v_{\max}}$ and in the chordwise direction $\hat{z}_{v_{\max}}$ of the node that shows $v = v_{\max}$.

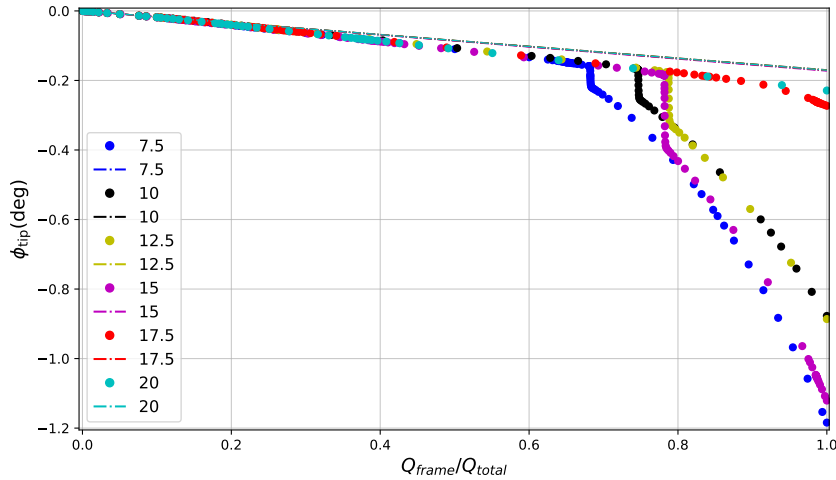


Figure 5.24: Displacement-force curve for various values of the chiral node radius r_{chi} .

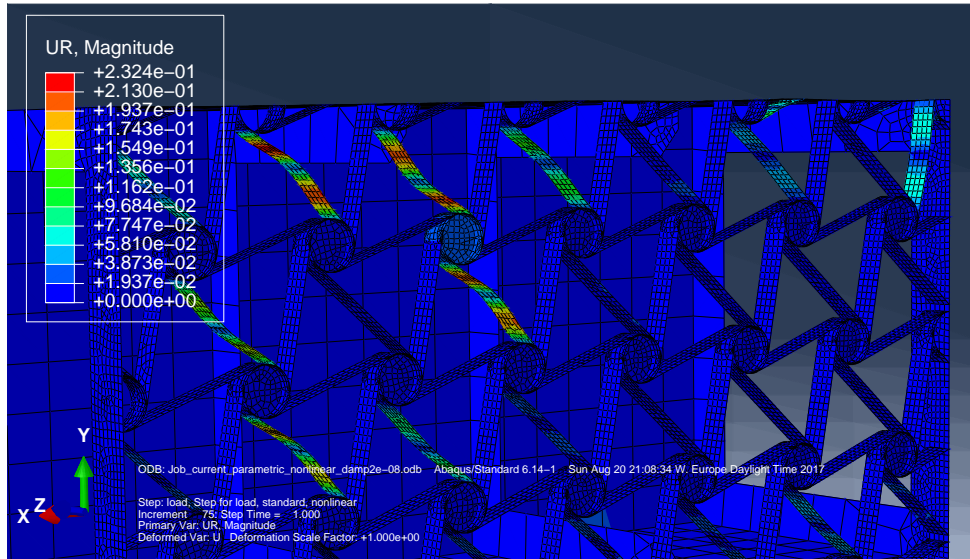


Figure 5.25: Colour contour showing the total rotational displacement when the fraction of load applied equals to 100% of the prescribed load (700 N) and $r_{\text{chi}} = 17.5$ mm. Here, the excessive value of the chiral node radius r_{chi} makes that the buckled region is moved towards increasing values of x .

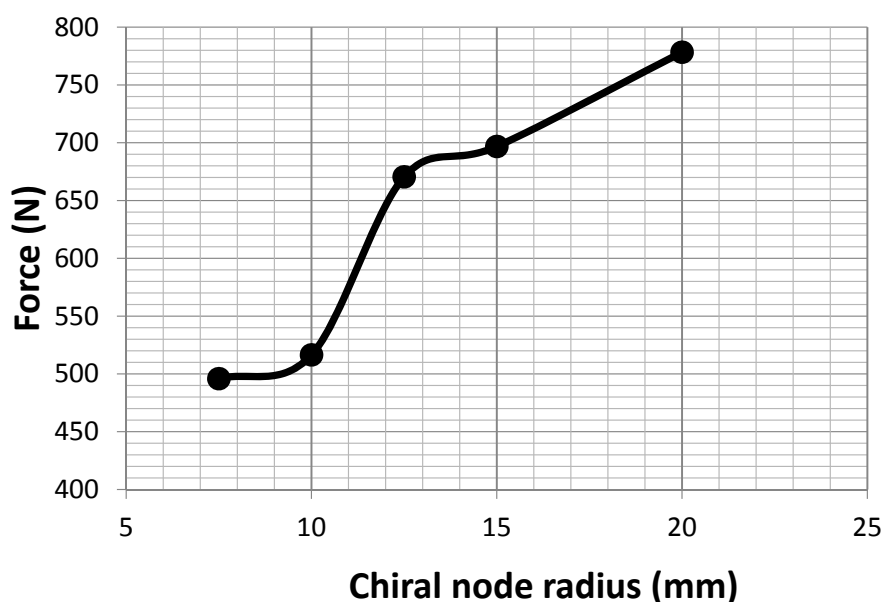


Figure 5.26: Force that induces the structure to collapse as a function of the chiral node radius r_{chi} .

Chiral ligament half length L_{chi}

The numeric results obtained for the parametric study on the chiral ligament half length L_{chi} are shown in Table 5.7. The geometrical meaning of this parameter can be seen in the sketch shown in Figure 3.8. The displacement-force curve for the set of values analysed is shown in Figure 5.27. This plot shows that the bigger the ligament half length is, the earlier the structure collapses after severe buckling of the ligaments at the root. For the case of $L_{\text{chi}} = 30$, the structure does not collapse because the higher ligaments length has incremented the buckling load.

Again, in a further step, the force that causes the structure to collapse for a given value of the half length L_{chi} parameter is investigated. The resulting plot is shown in Figure 5.28.

L_{chi}	ϕ_{tip} (deg)	$e(\phi_{\text{tip}})$ (%)	$\tilde{\phi}_{\text{tip}}$ (deg)	$e(\tilde{\phi}_{\text{tip}})$ (%)	v_{\max}	$\hat{z}_{v_{\max}}$	$\hat{x}_{v_{\max}}$
30	-0.181	13.106	-0.131	-8.951	-1.101	1	0.602
50	-1.596	14.222	-0.203	-18.444	-14.267	1	0.334
70	-3.252	13.574	-0.204	-8.297	-24.022	1	0.463

Table 5.7: Results from the parametric study on chiral ligament half length r_{chi} . The results show the mean twist at the tip of the wing-box for the Abaqus nonlinear simulation ϕ_{tip} and for the linear simulation $\tilde{\phi}_{\text{tip}}$. The maximum relative error of the mean calculation, expressed as percentage, for these two magnitudes is $e(\phi_{\text{tip}})$ and $e(\tilde{\phi}_{\text{tip}})$, respectively. The table also shows the maximum vertical displacement v_{\max} among all the mesh nodes located on the upper skin of the wing-box and the dimensionless position in the spanwise direction $\hat{x}_{v_{\max}}$ and in the chordwise direction $\hat{z}_{v_{\max}}$ of the node that shows $v = v_{\max}$.

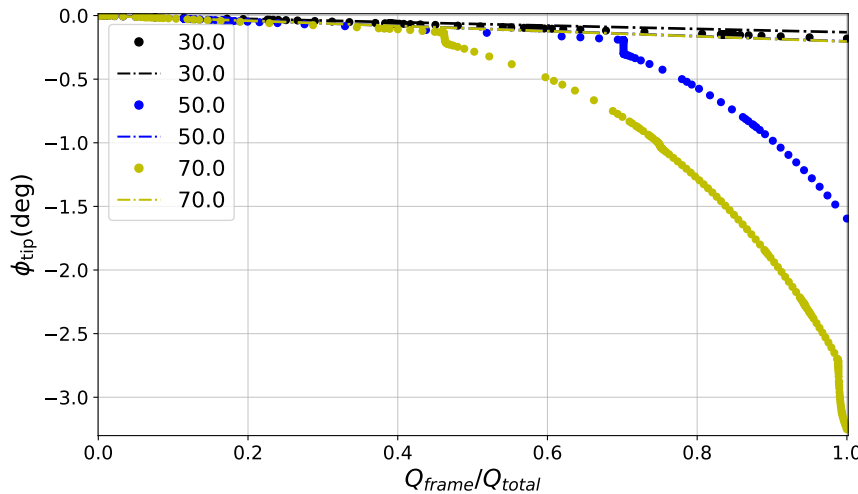


Figure 5.27: Displacement-force curve for various values of the chiral ligament half length L_{chi} . The bigger the ligament half length is, the earlier that the structure will collapse after severe buckling of the ligaments at the root.

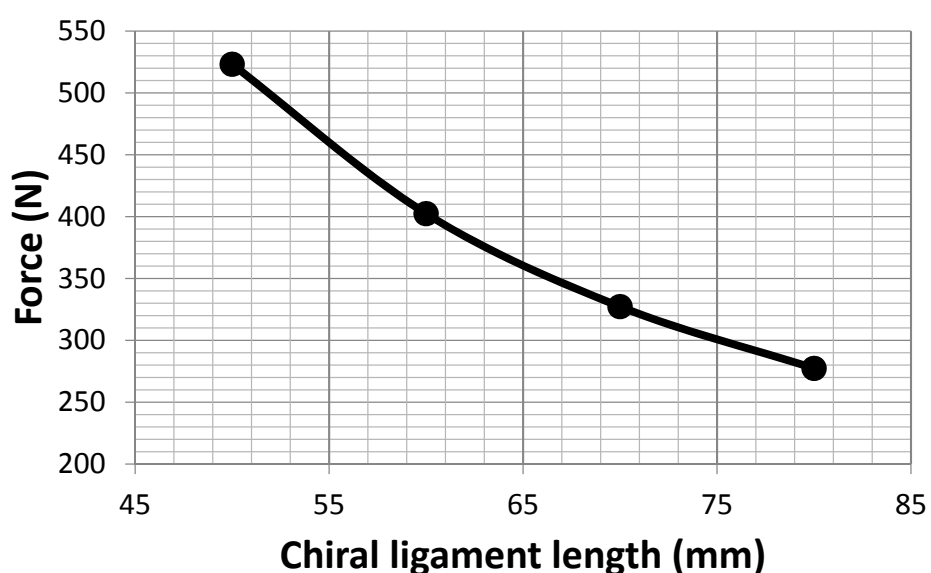


Figure 5.28: Force that induces the structure to collapse as a function of the chiral ligament half length L_{chi} .

Chiral structure thickness t_{chi}

The results for the parametric study performed on the chiral structure thickness t_{chi} are shown in Table 5.8. This parameter represents the wall thickness assigned to all the shell elements that form the lattice structure part, shown in Figure 3.8. The displacement-force curve is shown in Figure 5.29. Here it can be seen that a thicker chiral structure delays the structure collapse. An interesting aspect to be considered is that the more bigger the thickness t_{chi} is, the bigger the magnitude of the sudden wing-box twist adaptation is.

Finally, the required force to induce the structure collapse is plot against the corresponding value of the chiral structure thickness t_{chi} , resulting on the curve shown in Figure 5.30.

t_{chi}	ϕ_{tip} (deg)	$e(\phi_{\text{tip}})(\%)$	$\tilde{\phi}_{\text{tip}}$ (deg)	$e(\tilde{\phi}_{\text{tip}})(\%)$	v_{\max}	$\hat{z}_{v_{\max}}$	$\hat{x}_{v_{\max}}$
0.2	-1.413	11.363	-0.233	-15.24	-10.646	1	0.546
0.4	-1.331	11.406	-0.206	-15.187	-12.654	1	0.334
0.6	-0.699	14.276	-0.193	-18.502	-7.311	1	0.546
0.8	-0.186	6.856	-0.125	-12.046	-2.039	1	0.546

Table 5.8: Results from the parametric study on chiral structure thickness t_{chi} . The results show the mean twist at the tip of the wing-box for the Abaqus nonlinear simulation ϕ_{tip} and for the linear simulation $\tilde{\phi}_{\text{tip}}$. The maximum relative error of the mean calculation, expressed as percentage, for these two magnitudes is $e(\phi_{\text{tip}})$ and $e(\tilde{\phi}_{\text{tip}})$, respectively. The table also shows the maximum vertical displacement v_{\max} among all the mesh nodes located on the upper skin of the wing-box and the dimensionless position in the spanwise direction $\hat{x}_{v_{\max}}$ and in the chordwise direction $\hat{z}_{v_{\max}}$ of the node that shows $v = v_{\max}$.

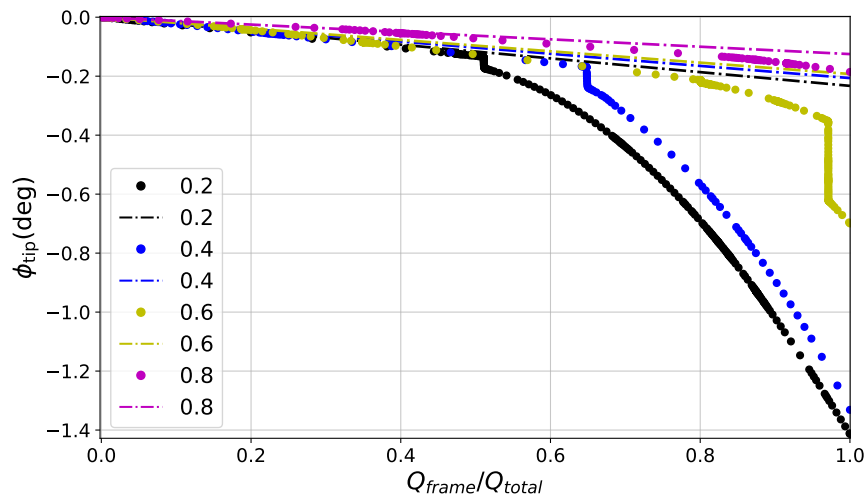


Figure 5.29: Displacement-force curve for various values of the chiral structure thickness t_{chi} . The bigger the ligament half length is, the earlier that the structure will collapse after severe buckling of the ligaments at the root.

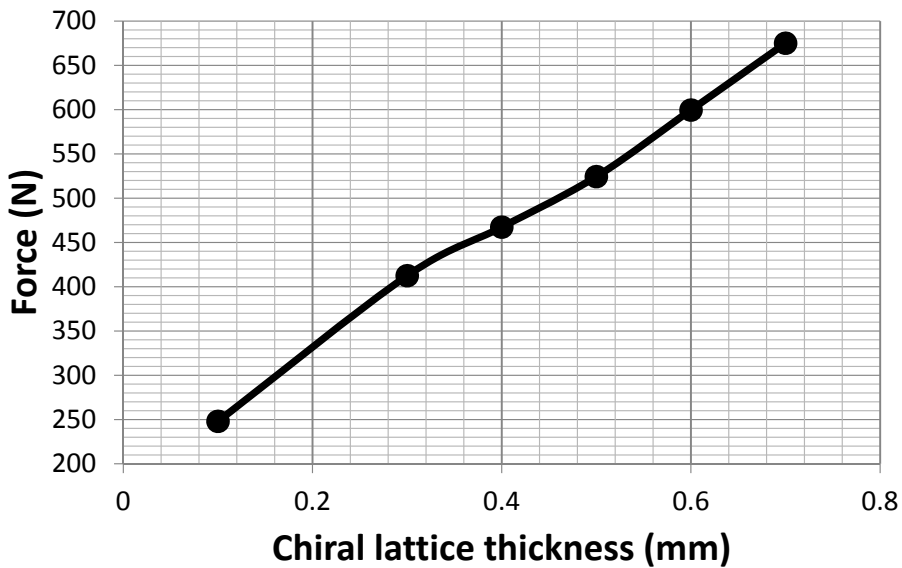


Figure 5.30: Force that induces the structure to collapse as a function of the chiral structure thickness t_{chi} .

Chapter 6

Aeroelastic study

In the present chapter, the compliant design for the wing-box is embedded into a full wing model. A pressure field is then introduced to simulated the pressure distribution obtained from the evaluation of the aerodynamic forces around the airfoil.

6.1 Wing model

The wing is modeled in its half span dimension and the airfoil is one symmetric NACA 0012. An overview of the wing model can be seen in Figure 6.1.

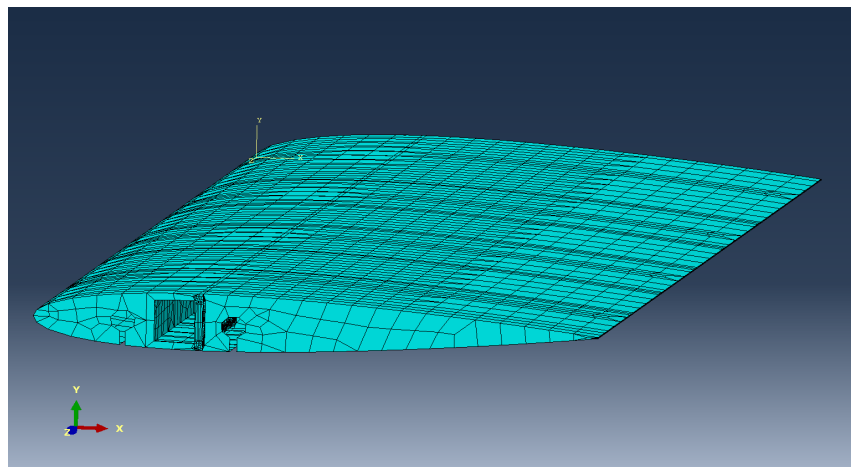


Figure 6.1: Overview of the wing FEM model embedded with the compliant wing-box design.

The boundary condition for the wing-box includes establish a free condition at the tip of the wing and a clamping condition at the root.

6.2 Aerodynamic model

The pressure distribution originated from the fluid-airfoil interaction is responsible of the forces applied into the wing model. This is the only source of forces introduced into the model. The pressure distribution is obtained using ©XFOIL software which considers the airfoil geometry and the flight condition.

The flight condition is determined by introducing the air velocity V , the air density ρ , the air dynamic viscosity μ

Chapter 7

Conclusion and Outlook

This thesis presents a novel passive mechanism  wing twist morphing  achieved through the control of the wing-box bending-twist coupling. The system incorporates a variable-stiffness spar in the wing-box that comprises a lattice of chiral elements. In the ligaments of these elements, elastic instabilities are intentionally induced and thus the effective shear modulus of the adaptive spar is modified. This phenomena provokes the wing-box section shear centre shifting and the consequent modification in wing-box torsional stiffness. This, ultimately induces a wing-box twist adaptation that has been passively activated exploiting local elastic instabilities.

An analytical model of the wing-box is developed using an ideal beam configuration with variable shear modulus in one of the webs. The effect of variations of this magnitude on the torsional stiffness, the flexural stiffness, the shear centre position and the bending and twisting deformations of the wing-box are studied. Also, the effect of variations of the geometry in these magnitudes is analysed. Results anticipate that, once the buckling-induced reduction in shear modulus in the spar is activated, the reduction in flexural stiffness for the wing-box is negligible compared with the reduction in torsional stiffness.

A computational model of the whole wing-box assembly is built next. It is designed in a fully parameterized format using Python scripting. This model is constituted of a wing-box in C-profile, a lattice of chiral elements and a tunable number of ribs that provide additional transversal stiffness and avoid local deformations in the wing-box skin. Different design options are considered, such as variations in the geometry, the load, the mesh and the number of ribs. An analysis of this model is performed in order to obtain a baseline configuration to posteriorly execute parametric studies. One of the aspects considered is this analysis is the modeling of the lattice nodes rigid body behavior. Results shows that the best modeling approach is to add an additional rigid part to provide supplementary stiffness. The addition of ribs in the middle of wing-box length is necessary to provide additional stiffness in the transversal direction and prevent undesired local deformations in the wing-box skin. Another consideration is the appearance of sources of instabilities such as buckling that require the inclusion of artificial damping factor into the simulation.

Nonlinear simulations are carried out using this model and incorporating artificial dissipation through 

constant damping factor. Special attention needs to be taken so that the inclusion of artificial damping factor is not leading to inaccurate results due to over-damping of the structure. The onset of the buckling phenomena and its evolution in the chiral lattice is characterized next. Results show that the collapse of the structure occurs when severe buckling appears on the ligaments of the chiral elements located at the root of the wing-box. This event produces a sudden reduction on the torsional stiffness of the structure and an increase in the wing-box twist adaptation observed at the tip. A second and more generalized buckling in the chiral lattice is observed to origin a second modification of the torsional stiffness for certain cases. For the baseline configuration of the model, the twist morphing of the wing-box is obtained to be equal to -1.25 degrees for the nonlinear simulation while the predicted twist for the linear simulation is -0.19 degrees.

Furthermore, a parametric study is performed on the computational model. Results show that considerable tailorability can be achieved through modifications of selected parameters. The parameter that shows to have a bigger influence in the onset and evolution of the elastic instabilities is the wing-box thickness. Increasing the wing-box thickness by 0.1 mm, provokes that the required force to induce the appearance of buckling at the root increases by 100 N.

CONCLUSIONS FROM THE WING SIMULATIONS

In further studies of this technology, it would be necessary to numerically analyse the system response for more realistic aerodynamic loads and also manufacture a demonstrator that could be used to experimentally test the feasibility of the proposed concept. The analysis of the time-bounded response of this mechanism is beyond the scope of this preliminary work, but such a investigation would be a crucial prior implementation of the system on a real lift generating structure.

The proposed morphing has been shown to be capable of inducing global twist morphing of a wing-box exploiting local elastic instabilities. It has shown to be promising to be applied on realistic wing structures for which the torsional response is dominated by the wing-box. Possible applications may include load alleviation purposes on lift-generating structures with high aspect ratio.

Bibliography

- [1] J.E Cooper, “Introduction to Aircraft Aeroelasticity and Loads,” in *Gust and Turbulence Encounters*, no. 1996, ch. 14, John Wiley & Sons, Ltd., 2007.
- [2] “Part of ”the dream of flight” online exhibit in the American Treasures section at the U.S. Library of Congress.” <http://www.loc.gov/exhibits/treasures/images/>. Accessed: 29 July 2017.
- [3] P. a. Lloyd, “Requirements for smart materials,” *Proceedings of the Institution of Mechanical Engineers, Part G: Journal of Aerospace Engineering*, vol. 221, no. 4, pp. 417–478, 2007.
- [4] S. Boye, “A passenger aircraft with a downwardly foldable wing tip device.” UK Patent: GB2524827. Available at: <https://www.gov.uk/browse/business/intellectual-property/>, 2015. Accessed: 27 July 2017.
- [5] S. Barbarino, O. Bilgen, R. M. Ajaj, M. I. Friswell, and D. J. Inman, “A Review of Morphing Aircraft,” *Journal of Intelligent Material Systems and Structures*, vol. 22, no. 9, pp. 823–877, 2011.
- [6] G. D. Miller, “Active Flexible Wing (AFW) Technology,” tech. rep., 1988.
- [7] E. Pendleton, P. Flick, D. Paul, D. Voracek, E. Reichenbach, and K. Griffin, “The X-53 A Summary of the Active Aeroelastic Wing Flight Research Program,” *48th AIAA/ASME/ASCE/AHS/ASC Structures, Structural Dynamics, and Materials Conference*, no. April, 2007.
- [8] P. C. Chen, D. Sarhaddi, R. Jha, D. D. Liu, K. Griffin, R. Yurkovich, S. Antonio, R. Yurkovich, and T. B. Company, “Variable Stiffness Spar Approach for Aircraft Maneuver Enhancement Using ASTROS,” *Journal of Aircraft*, vol. 37, no. 5, pp. 865–871, 2000.
- [9] M. Amprikidis and J. E. Cooper, “Development of an Adaptive Stiffness Attachment for an All-Moving Vertical Tail,” *46th AIAA/ASME/ASCE/AHS/ASC Structures, Structural Dynamics and Materials Conference*, no. April, pp. 1–11, 2005.
- [10] B. Stanford, M. Abdulrahim, R. Lind, and P. Ifju, “Investigation of Membrane Actuation for Roll Control of a Micro Air Vehicle,” *Journal of Aircraft*, vol. 44, no. 3, pp. 741–749, 2007.
- [11] B. P. Sanders, C. Martin, and D. Cowan, “Aerodynamic and aeroelastic characteristics of the DARPA Smart Wing phase II wind tunnel model,” *Smart Structures and Materials 2001*, vol. 4332, pp. 390–398, 2001.

- [12] D. M. Elzey, A. Y. N. Sofla, H. N. G. Wadley, A. Y. N. Sofia, and H. N. G. Wadley, “A bio-inspired high-authority actuator for shape morphing structures,” *Proceedings of SPIE*, vol. 5053, no. 7, pp. 1943–1955, 2003.
- [13] A. F. Arrieta, I. K. Kuder, M. Rist, T. Waeber, and P. Ermanni, “Passive load alleviation aerofoil concept with variable stiffness multi-stable composites,” *Composite Structures*, vol. 116, no. 1, pp. 235–242, 2014.
- [14] D. Bornengo, F. Scarpa, and C. Remillat, “Evaluation of hexagonal chiral structure for morphing airfoil concept,” *Proceedings of the Institution of Mechanical Engineers, Part G: Journal of Aerospace Engineering*, vol. 219, no. 3, pp. 185–192, 2005.
- [15] A. Spadoni and M. Ruzzene, “Static Aeroelastic Response of Chiral-core Airfoils,” *Journal of Intelligent Material Systems and Structures*, vol. 18, no. October, pp. 1067–1075, 2007.
- [16] A. Spadoni and M. Ruzzene, “Numerical and experimental analysis of the static compliance of chiral truss-core airfoils,” *Journal of Mechanics of Materials and Structures*, vol. 2, no. 5, pp. 965–981, 2007.
- [17] W. Raither, A. Bergamini, and P. Ermanni, “Profile beams with adaptive bending-twist coupling by adjustable shear centre location,” *Journal of Intelligent Material Systems and Structures*, vol. 24, no. 3, pp. 334–346, 2013.
- [18] A. Bergamini, R. Christen, B. Maag, and M. Motavalli, “A sandwich beam with electrostatically tunable bending stiffness,” *Smart Materials and Structures*, vol. 15, no. 3, pp. 678–686, 2006.
- [19] W. Raither, A. Bergamini, F. Gandhi, and P. Ermanni, “Adaptive bending-twist coupling in laminated composite plates by controllable shear stress transfer,” in *Composites Part A: Applied Science and Manufacturing*, vol. 43, pp. 1709–1716, 2012.
- [20] W. Raither, M. Heymanns, A. Bergamini, and P. Ermanni, “Morphing wing structure with controllable twist based on adaptive bending-twist coupling,” *Smart Materials and Structures*, vol. 22, no. JUNE 2013, p. 065017, 2013.
- [21] F. Runkel, A. Reber, G. Molinari, A. F. Arrieta, and P. Ermanni, “Passive twisting of composite beam structures by elastic instabilities,” *Composite Structures*, vol. 147, pp. 274–285, 2016.
- [22] R. Andreas, *Experimental investigation of the structural response of a wing model with structurally tailored buckling elements for morphing*. Master thesis no. 15-007, ETH Zürich, 2015.
- [23] R. S. Lakes, “Deformation mechanisms in negative Poisson’s ratio materials: structural aspects,” *Journal of Materials Science*, vol. 26, no. 9, pp. 2287–2292, 1991.
- [24] D. Prall and R. Lakes, “Properties of a chiral honeycomb with a poisson’s ratio of 1,” *International Journal of Mechanical Sciences*, vol. 39, no. 3, pp. 305–314, 1997.
- [25] P. Bettini, A. Aioldi, G. Sala, L. D. Landro, M. Ruzzene, and A. Spadoni, “Composite chiral structures for morphing airfoils: Numerical analyses and development of a manufacturing process,” *Composites Part B: Engineering*, vol. 41, no. 2, pp. 133–147, 2010.

- [26] A. Spadoni, M. Ruzzene, and F. L. Scarpa, “Global and local linear buckling behavior of a chiral cellular structure,” *Physica Status Solidi (B)*, vol. 242, no. 3, pp. 695–709, 2005.
- [27] J. Zhang and M. F. Ashby, “Buckling of honeycombs under in-plane biaxial stresses,” *International Journal of Mechanical Sciences*, vol. 34, no. 6, pp. 491–509, 1992.
- [28] L. J. Gibson and M. F. Ashby, *Cellular Solids: Structure and Properties*, vol. 7. 1999.
- [29] F. Scarpa, S. Blain, T. Lew, D. Perrott, M. Ruzzene, and J. R. Yates, “Elastic buckling of hexagonal chiral cell honeycombs,” *Composites Part A: Applied Science and Manufacturing*, vol. 38, no. 2, pp. 280–289, 2007.
- [30] W. Miller, C. W. Smith, F. Scarpa, and K. E. Evans, “Flatwise buckling optimization of hexachiral and tetrachiral honeycombs,” *Composites Science and Technology*, vol. 70, no. 7, pp. 1049–1056, 2010.
- [31] B. Haghpanah, J. Papadopoulos, D. Mousanezhad, H. Nayeb-Hashemi, and A. Vaziri, “Buckling of Regular, Chiral and Hierarchical Honeycombs under a General Macroscopic Stress State,” *Proceedings of the Royal Society A: Mathematical, Physical and Engineering Sciences*, vol. 470, no. 2167, p. 20130856, 2014.
- [32] G. Ramstein, *Experimental Validation of Chiral Structures with Local Controlled Instabilities*. Semester project no. 16-015, ETH Zürich, 2016.
- [33] A. Spadoni, M. Ruzzene, and F. Scarpa, “Dynamic Response of Chiral Truss-core Assemblies,” *Journal of Intelligent Material Systems and Structures*, vol. 17, no. November, pp. 941–952, 2006.
- [34] A. Airolidi, M. Crespi, G. Quaranti, and G. Sala, “Design of a Morphing Airfoil with Composite Chiral Structure,” *Journal of Aircraft*, vol. 49, no. 4, pp. 1008–1019, 2012.
- [35] A. Airolidi, P. Bettini, P. Panichelli, M. F. Oktem, and G. Sala, “Chiral topologies for composite morphing structures - Part I: Development of a chiral rib for deformable airfoils,” *Physica Status Solidi (B) Basic Research*, vol. 252, no. 7, pp. 1435–1445, 2015.
- [36] N. Hu and R. Burgueño, “Buckling-induced smart applications: recent advances and trends,” *Smart Materials and Structures*, vol. 24, no. 6, p. 063001, 2015.
- [37] P. M. Reis, “A perspective on the revival of structural (in) stability with novel opportunities for function: From buckliphobia to buckliphilia,” *Journal of Applied Mechanics*, vol. 82, no. 11, p. 111001, 2015.
- [38] R. Vincenz, *Airfoil camber morphing exploiting chiral structures: Manufacturing and testing*. Semester project no. 17-041, ETH Zürich, 2017.
- [39] Dassault Systèmes, *Abaqus 6.14 Online Documentation*, 2014.

Appendix A

Python code generated

All the code generated for this project can be downloaded from the following Github repository:
<https://github.com/AlejandroValverde/abaqus.git>.